

197 Candidates and 102 New Validated Planets in C0-C10 of K2

Andrew W. Mayo

Submitted in partial fulfillment of the requirements
for the degree of Bachelor of Arts in Physics and Astrophysics
in the Undergraduate College of Harvard University, 2017

ABSTRACT

Since 2014, the K2 mission has observed large portions of the ecliptic plane in search of transiting planets, and thus far discovered over 500 planet candidates in the first 10 campaigns. With observations planned up to at least campaign 16, many more planet candidates will continue to be discovered. We present here our identification of 197 planet candidates suitable for validation from campaigns 0-10 of the K2 mission. We subject these planets to a validation process in order to calculate the false positive probability (FPP), and find that 102 are validated ($FPP < 0.001$), 61 remain candidates ($0.001 < FPP$), and 34 are of an unknown disposition (we were unable to or chose not to report the false positive probability). Of the 102 newly validated planets, 32 have already been validated elsewhere, 37 have merely been identified as candidates elsewhere, and 33 have never been identified before. We describe the process of data reduction, candidate identification, and validation. We also explore the demographics of the newly validated planets. This research, in addition to dramatically increasing the population of validated K2 planets, will also provide new targets for follow-up observations, as well as serve as a framework for validating candidates from upcoming K2 campaigns and candidates identified through the Transiting Exoplanet Survey Satellite (TESS), expected to launch in early to mid 2018.

1. Introduction

The field of exoplanets is relatively young compared to most other disciplines of astronomy: the first discovery of an exoplanet system was only in 1992, when two small planets were found orbiting a pulsar through the method of pulsar timing variations

(Wolszczan & Frail 1992). The first confirmation of an exoplanet orbiting a main sequence star was only in 1995 (Mayor & Queloz 1995), although a reported brown dwarf discovered in 1989 may in fact be an exoplanet, depending on its inclination (Latham et al. 1989). Since then, the field has expanded rapidly, with many thousands of exoplanets having now been discovered. And with new, upcoming telescopes and space missions like the James Webb Space Telescope, the Transiting Exoplanet Survey Satellite (TESS; Ricker et al. 2015), the Thirty Meter Telescope (TMT; Sanders 2013), and the Giant Magellan Telescope (GMT; Johns et al. 2012), the number of known exoplanets and our understanding of them will only increase.

The work in this thesis expands our list of validated exoplanets, which will improve our understanding of exoplanet populations and provide new, interesting targets for follow-up observations. Further, this thesis develops methods of efficient exoplanet validation which will aid in the identification and follow-up of high-interest targets. It will also help us prepare for the validation work that will be required with the arrival of the Transiting Exoplanet Survey Satellite (TESS), in order to meet TESS’s level 1 science requirement of determining the masses of at least 50 exoplanets smaller than $< 4R_{\odot}$.

In order to understand how the research in this thesis fits into the current body of exoplanet work, it is important to discuss the key methods of exoplanet detection and the roles they have played in the field thus far. To date, there have been five primary methods of exoplanet detection: radial velocity, transit, direct imaging, microlensing, and transit timing variation. Below, we will discuss each of these methods and their impact briefly. Additionally, we will discuss the method of astrometry, which has detected and confirmed previously discovered exoplanets but has not yet made any exoplanet discoveries of its own. Lastly, we will briefly touch on a few other lesser known or lesser used methods of exoplanet detection, including the BEaming, Ellipsoidal, and Reflection phase modulation (BEER)

method, eclipse timing variations, pulsation timing variations, and pulsar timing variations.

1.1. Methods of Exoplanet Detection

1.1.1. The Radial Velocity Method

The radial velocity (RV) method is responsible for more exoplanet discoveries than any other method, except for the transit method. This method is employed by taking many spectra of a star and looking for small shifts in the wavelength of the spectra’s absorption features. Such shifts are due to the Doppler effect: as an orbiting planet tugs on its star, it causes the star to wobble back and forth due to the planet’s gravitational pull, causing the spectrum to be redshifted and blueshifted. This wobble effect can be seen in Fig. 1, where an RV curve is shown for the exoplanet 51 Peg b (Mayor & Queloz 1995). By measuring the amplitude of the stellar wobble and estimating the star’s mass, constraints can be put on the exoplanet’s mass. The semi-amplitude of this effect is related to the planet’s mass according to the following equation:

$$K = \frac{m_2}{(m_1 + m_2)} \frac{na \sin i}{\sqrt{1 - e^2}}$$

where K = semi-amplitude, m_1 = stellar mass, m_2 = planetary mass, $n = 2\pi/P$ = mean motion, a = semi-major axis, i = inclination, and e = eccentricity. Using Kepler’s Third Law to remove a and using more intuitive units, this equation can be rewritten as:

$$\frac{K}{m s^{-1}} = 203 \left(\frac{P}{days} \right)^{-1/3} \frac{(M_p/M_{Jup}) \sin i}{\left((M_*/M_\odot) + 9.548 \times 10^{-4} (M_p/M_{Jup}) \right)^{2/3} \sqrt{1 - e^2}}$$

where M_* is stellar mass, M_\odot is solar mass, M_p is planetary mass, and M_{Jup}

is Jupiter mass. According to the NASA Exoplanet Archive (Akeson et al. 2013; exoplanetarchive.ipac.caltech.edu, 10 Feb. 2017), the radial velocity method has thus far been used to measure the mass of 592 stellar companions with minimum or absolute masses below 13 Jupiter masses. 13 Jupiter masses is a commonly used (though somewhat arbitrary) threshold between brown dwarfs and exoplanets, corresponding to the limit below which deuterium burning in the core of an object is not ignited. Many of those discoveries were made using other methods, as the RV method is often employed as follow-up for exoplanets that have already been discovered (usually by the transit method).

One drawback of the RV method is that the RV amplitudes falls off as the size of the orbit increases (to be precise, RV amplitude scales with the inverse cube root of the period). This decreases the exoplanet detection sensitivity of the RV method at larger semi-major axes. Further, there is a strong degeneracy between planetary mass and inclination. In fact, RV mass is often something of a misnomer, as most of the time the RV method is only able to yield $m \sin i$ (i.e. mass \times sin(orbital inclination)), rather than actual planetary mass. Fortunately, the semi-amplitude of the RV signal is still quite large even for highly inclined systems: at $i = 60^\circ$, the RV amplitude only drops by 50% relative to $i = 0^\circ$. Through statistical considerations, the mass of a planet detected with the RV method is $M_p \approx 1.4M_p \sin i$ on average (i.e. 40% higher than the measured value of $m \sin i$).

1.1.2. *The Transit Method*

The transit method is responsible for more exoplanet detections than any other method. The transit method relies on the small dip in light that occurs when an exoplanet passes in front of its star. Fig. 2 shows two transit light curves from the first exoplanet ever discovered by the transit method (Charbonneau et al. 2000). By measuring the depth of a transit and estimating the stellar radius, the radius of the exoplanet can also be determined

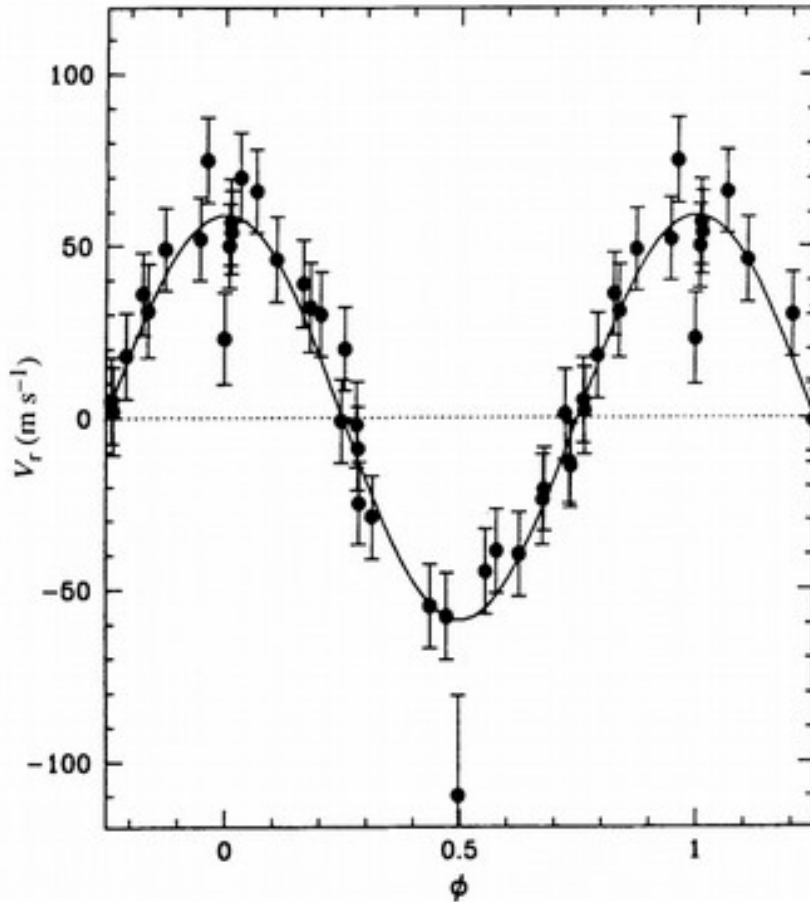


Fig. 1.—: Phase-folded radial velocity curve of 51 Peg b. This figure is reproduced from Mayor & Queloz (1995).

using

$$\left(\frac{R_p}{R_*}\right)^2 = \text{depth}$$

(note that this is only an approximation, as it doesn't consider the effects of limb-darkening).

The transit method is extremely useful when applied in tandem with the RV method. Transits provide a measurement of the planetary inclination, which allows the $m \sin i$ value measured by the RV method to be converted into a true mass. Knowing both the mass

and radius of an exoplanet allows its bulk density to be calculated. In general, larger exoplanets are gaseous, akin to Neptune or Jupiter, and typically low-density (unless they are very large). On the other hand, smaller planets tend to be rocky, like Earth or Venus, and higher-density. Rogers (2015) found that at short periods, most planets above 1.6 Earth radii appear to be gaseous rather than rocky. (Near this cutoff point, planets are usually called mini-Neptunes or super-Earths, depending on if they are gaseous or rocky in composition respectively.)

The transit method has yielded thousands of exoplanet discoveries so far, primarily through the *Kepler* mission. Because so many of the major accomplishments of the transit method have been made thanks to *Kepler*, we will delve into breakthroughs and discoveries made with the transit method in section 1.3.1

Unfortunately, the transit method has a few drawbacks. The transit method can only be applied when a planetary system is fortuitously aligned with observers to cause a transit. This automatically eliminates all but a few percent of exoplanets, even those that can be detected by the RV method. This effect worsens at larger semi-major axes (since the alignment required for a transit is even tighter and therefore fortuitous transits are even less likely). As such, long period planets like solar system analogs are only rarely detected because of their very low transit likelihood. Further, even when longer period planets are detected, observers must wait much longer to observe each transit, making detection and characterization even more difficult.

1.1.3. *The Direct Imaging Method*

Another common method of exoplanet detection is direct imaging, which is essentially just taking a picture of the planet. This is done by overcoming the high contrast between a

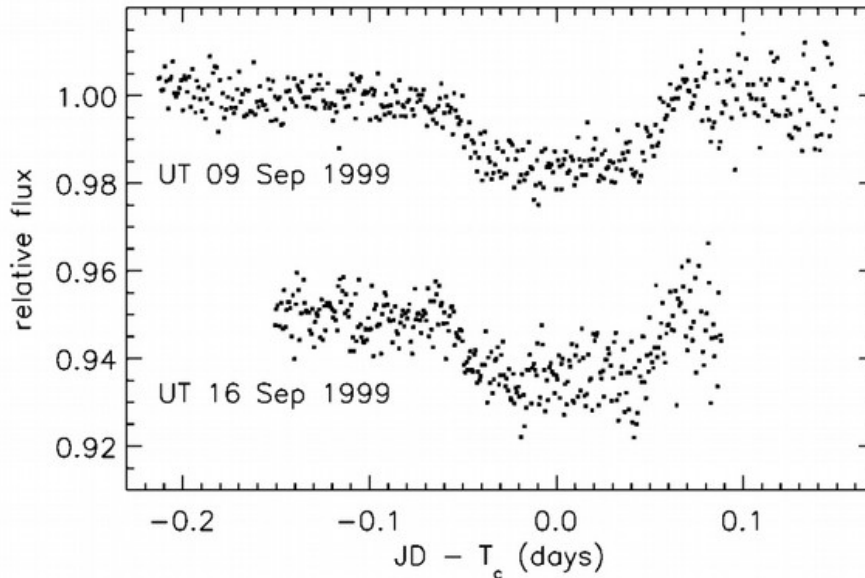


Fig. 2.—: Two transits of HD 209458b, the first exoplanet detected with the transit method. This figure is reproduced from Charbonneau et al. (2000).

star’s brightness and a planet’s brightness in order to resolve the two components separately. This method typically employs some sort of masking system on a telescope which blocks as much of a star’s light as possible while blocking as little of a nearby planet’s light as possible. Additionally, ground-based direct imaging surveys must often rely on adaptive optics (AO), a technology through which one of the telescope’s mirrors is warped hundreds of times per second in order to counteract atmospheric turbulence. Many telescopes with AO systems are able to reach the diffraction limit in their observations.

With sufficient contrast, light from the planet can be seen separate from the star’s light. The poster child for direct imaging is the HR 8799 system, seen in Fig. 3; no other system detected with direct imaging has found more than two planets in a system. HR 8799, however, was originally observed to host three planets, and a fourth was later discovered (Marois et al. 2010). According to the NASA Exoplanet Archive

(exoplanetarchive.ipac.caltech.edu, 11 Feb. 2017), the direct imaging method has resulted in the detection of 20 planetary companions (with masses estimated at or below the 13 Jupiter mass threshold). Note that direct imaging does not allow for dynamical mass measurements (except perhaps in conjunction with astrometry), but rather estimated via models based on system age, planet luminosity, or a planetary spectrum.

Direct imaging is extremely useful since it allows a spectrum of the planet to be taken directly, from which atmospheric characterization can be performed. Additionally, direct imaging allows for intensive study of planets near and beyond the snow line (where volatiles in the system condensate from gas to solid), which is very difficult or impossible with other methods. In fact, microlensing is most sensitive to planets near the snow line. On the other hand, this method preferentially detects young systems with self-luminous planets, since self-luminous planets are brighter and therefore easier to detect.

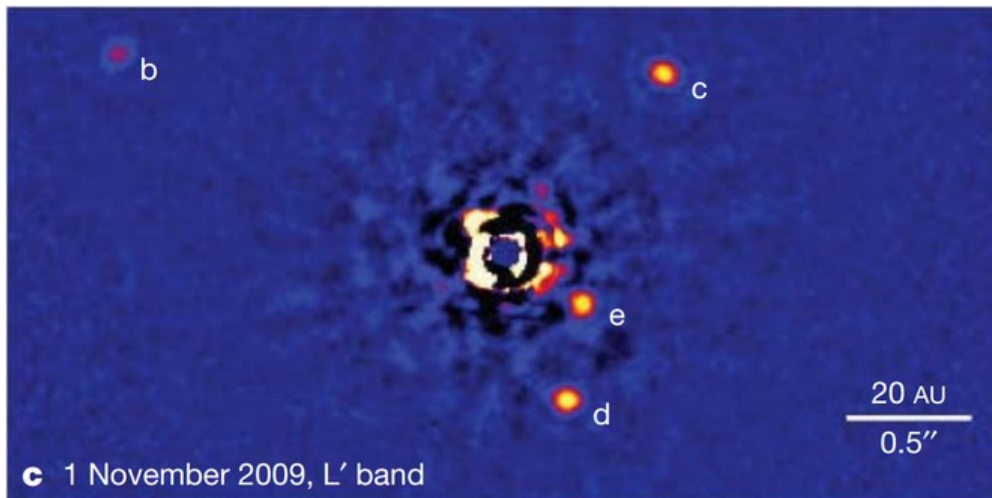


Fig. 3.—: Direct image of the HR 8799 system, a system with 4 known giant planets, all beyond 10 AU. This figure is reproduced from Marois et al. (2010).

1.1.4. *The Microlensing Method*

The microlensing method relies on the bending of light according to Einstein’s general theory of relativity. Given a distant lensing object (typically ~ 4 kPc) and an even more distant source object (typically ~ 8 kPc, near the Galactic Bulge), light from the source will be lensed and magnified as the source passes in front of the lens (along the observer’s line of sight). Although the magnification is never high enough to allow the source to be resolved (at least for exoplanets), the brightness of the source is still dramatically increased, sometimes by many orders of magnitude.

If there happens to be a planet in the source star system, observers may detect a secondary magnification effect. See in Fig. 4 the first microlensing event leading to the discovery of an exoplanet; the long-term peak in brightness is due to the source star, while the two sharp peaks are caused by an orbiting planet, roughly 1.5 Jupiter masses (Bond et al. 2004). By modeling the entirety of a microlensing event for a system with an exoplanet, the planet’s mass can usually be determined (by assuming a reasonable stellar mass or estimating the stellar mass through follow-up). Sometimes, depending on the quality of the initial data, the follow-up, and the nature of the system, additional parameters can also be determined, such as semi-major axis, inclination, and true mass (without stellar mass assumptions)

According to the NASA Exoplanet Archive (exoplanetarchive.ipac.caltech.edu, 11 Feb. 2017), the microlensing method has resulted in the detection of 44 planetary companions (with measured masses at or below the 13 Jupiter mass threshold). The microlensing method is excellent for analyzing planets at distances of many AU, which makes it a very useful method for researching planets at or beyond the snow line. The downside to microlensing is that follow-up is generally impossible, as the source system is typically too faint after the microlensing event has ended to be detected again (Yee et al. 2016).

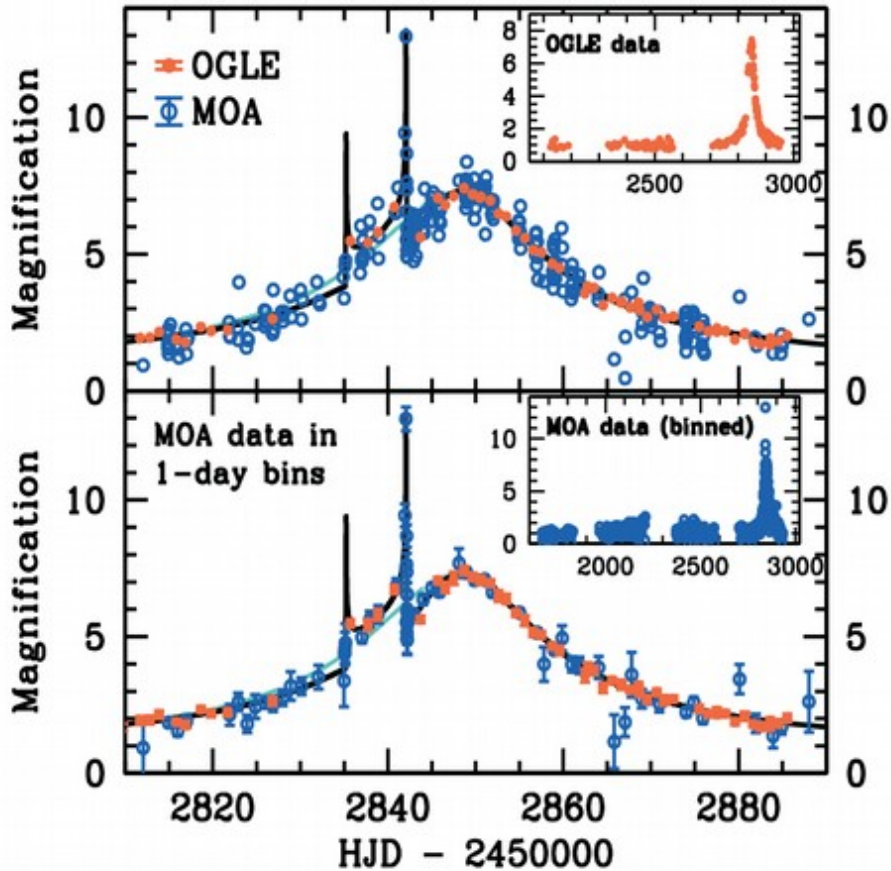


Fig. 4.—: The microlensing event for the first exoplanet discovered through the microlensing method, OGLE 2003-BLG-235Lb. This figure has been reproduced from Bond et al. (2004).

1.1.5. The Transit Timing Variation Method

The transit timing variation (TTV) method relies on minor variations in the time of planetary transits due to planet-planet gravitational interactions. This method can only be applied if: 1) at least one planet transits, and 2) there are at least two planets in the system. It also helps if the two planets are near resonance with one another, i.e. the ratio of orbital periods is near n/m , where n and m are both integers. Near resonance, the TTV effect is greatly amplified (Agol et al. 2005). As an extreme example, the Kepler-88 system has two

planets near a 2:1 resonance, which causes TTVs on the order of 12 hours for the smaller planet, Kepler-88b (see Fig. 5). As planets orbit their star and pass by one another, the gravitational kick that each planet delivers to the other during conjunction causes planets to arrive at transit early or later than expected. By either employing simplified analytical expressions or an N-body numerical integration, the TTVs can be precisely modeled in order to ascertain the mass of the perturbing planet, and possibly other parameters such as eccentricity and argument of the periastron (i.e. the orientation of the planet’s elliptical path with respect to observers). The TTV method can reveal planets that would be either difficult or impossible to detect with other methods, especially low-mass planets (Ballard et al. 2011). However, the strict requirements on this method make it only occasionally applicable. According to the NASA Exoplanet Archive (exoplanetarchive.ipac.caltech.edu, 11 Feb. 2017), the TTV method has resulted in the detection of 11 planetary companions (with measured masses at or below the 13 Jupiter mass threshold). It should be noted that while only 11 planets have been *discovered* via the TTV method, many more planets discovered via other methods have had subsequent mass measurements or mass constraints made using TTVs.

Another measurement similar to TTVs that bears brief mentioning is transit duration variations (TDVs). If a planet transits near periastron (the point of closest approach to the star), the transit duration will be much shorter than if it transits during apastron. TDVs are not very effective for discovering exoplanets in their own right (since TTVs would likely be sufficient to detect any planet that TDVs could detect) but they are useful for placing stronger constraints on parameters such as planetary inclination, as well as gaining information on the system architecture. For instance, in the case of a large, non-transiting planet, TTVs can suggest the presence of the planet but still yield highly multimodal solutions, particularly for the non-transiting planet’s period (since many near-resonance orbital periods can induce similar TTV signals). Modeling TDVs alongside TTVs can

provide additional information with which to assess the likelihood of each mode.

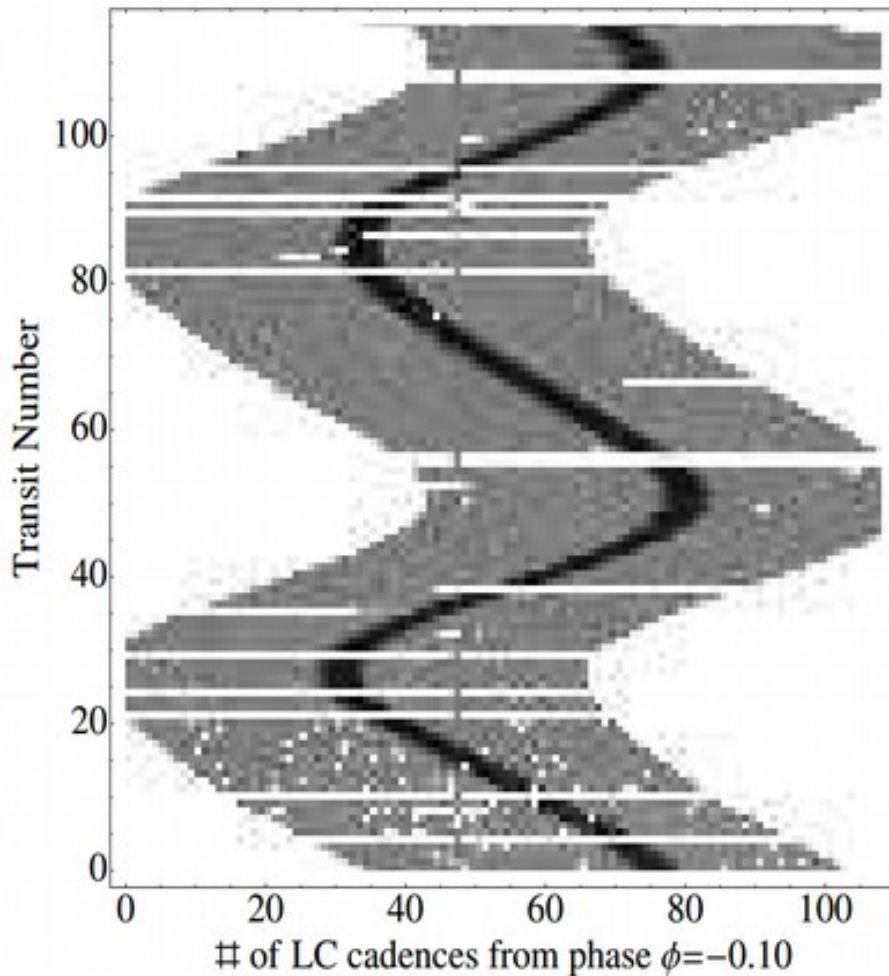


Fig. 5.—: A river plot for Kepler-88b, a planet with enormous, ~ 12 hour transit timing variations. This plot has been reproduced from Nesvorný et al. (2013): gray is the normalized flux, black is the flux level during transit, and white represents an absence of data.

1.1.6. Astrometry

Astrometry bears mentioning as a method of exoplanet detection even though it has yet to discover any exoplanets. The method is essentially to look for periodic wobbling of a star’s centroid of light, indicative of the gravitational tug of an orbiting planet. This is

somewhat similar to the RV method, which also looks for stellar wobble in order to infer the presence of a planet. However, this method is best applied when the system is face-on whereas the RV method is most effective when the system is edge-on.

Although astrometry has thus far been a disappointing method of exoplanet discovery, it has however been useful in occasionally detecting previously discovered exoplanets and thereby placing stronger constraints on systems; for example, certain high mass exoplanets discovered by the transit or RV methods, such as McArthur et al. (2010), have been confirmed and had stronger constraints placed on their mass or inclination through astrometry (see Fig. 6). With the launch of the Gaia spacecraft in 2013 and the first Gaia data release in 2016, astrometry is finally expected to yield its first exoplanet discoveries (Gaia Collaboration et al. 2016). In fact, the yield thanks to Gaia is expected to be enormous. Perryman et al. (2014) predicts $21,000 \pm 6,000$ exoplanet discoveries through astrometry during Gaia’s nominal 5 year mission; with an extended 10 year mission, that number rises to $70,000 \pm 20,000$ exoplanet discoveries. If these predictions prove accurate, Gaia’s astrometry work could increase the number of known exoplanets by over an order of magnitude thanks and significantly fill the high mass, long period regions of exoplanet parameter space.

1.1.7. Additional Methods of Exoplanet Detection

Besides the methods thus far discussed, there are a few additional methods of exoplanet detection which have only been applied to a handful systems. The BEaming, Ellipsoidal, and Reflection phase modulation (BEER) method consists of simultaneously looking for photometric modulations due to beaming (sometimes called Doppler boosting), ellipsoidal variations (distortions of the stellar shape) caused by tidal interactions, and reflection of light from the star or planet onto each other (see the discovery of Kepler-76b for more

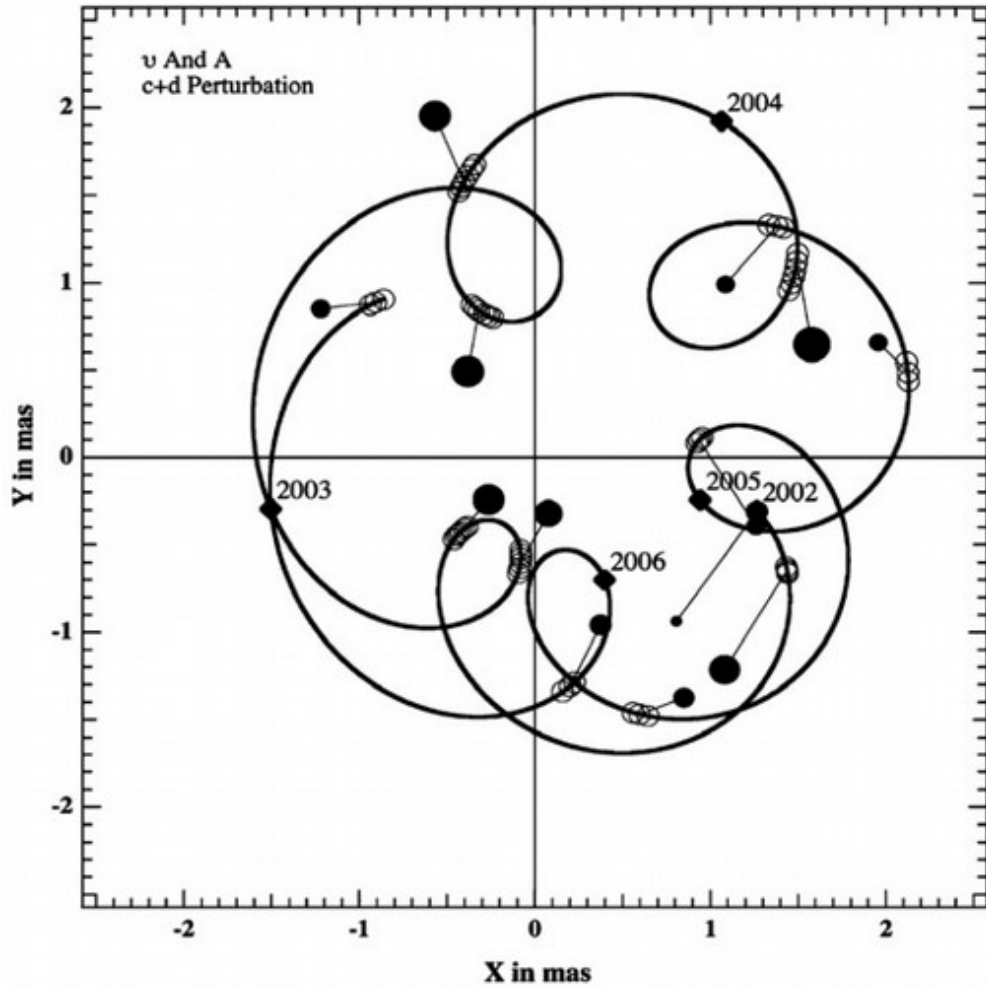


Fig. 6.—: Astrometric measurements of ν Andromedae Reflex motion of the star is due to ν Andromedae c and d, which places constraints on the stellar mass, planetary masses and periods, and system inclination. Figure reproduced from McArthur et al. (2010).

details; Faigler et al. 2013). Another method is eclipse timing variations, in which an eclipsing binary system exhibits small timing variations in star/star eclipses due to the gravitational pull of planetary mass objects, similar to the TTV method (see the discovery of 2 planets in the NN Ser system for more details; Qian et al. 2009, Beuermann et al. 2010). Exoplanets have also been detected via pulsation timing variations, which involves observing large, pulsating stars for small changes in pulsation times, suggesting a light

arrival time delay indicative of stellar motion due to an orbiting planet (see the discovery of KIC 7917485b for more details; Murphy et al. 2016). This method may prove useful for detecting exoplanets around massive stars, which has thus far proven a significant challenge due to the large stellar to planetary radius ratio and lack of narrow spectral absorption features (which cause difficulties for the transit and RV methods respectively). The last method to mention is that of pulsar timing variations, which was briefly mentioned earlier. Looking for anomalies in measurements of the pulsation period can reveal gravitational interactions with planetary-mass objects. This method was first used to discover two super-Earth exoplanets in the PSR1257+12 system (Wolszczan & Frail 1992), followed by an object less than twice the mass of the moon in the same system two years later (Wolszczan 1994). According to the NASA Exoplanet Archive (exoplanetarchive.ipac.caltech.edu, 11 Feb. 2017), this method has since been used for only two other other exoplanets.

1.2. A Detailed Description of Transits

1.2.1. *A First-Approximation Model*

This thesis relies on the transit method more than any other method described above. Thus, we will turn to focus on the transit method in more detail. It is important to keep in mind that transits provide observers with far more than simply the radius of an exoplanet. To a first order approximation, a transit is simply a trapezoid-shaped depression in a light curve, where the base of the trapezoid corresponds to the passage of the exoplanet across the star’s face and the sloped sides match the exoplanet’s ingress onto and egress off the star’s face. The depth of the transit conveys information about the planet’s radius while the slope of the ingress and egress lines places constraints upon the impact parameter of the planet (how close the transit chord passes by the center of the stellar disc), consequently constraining the planet’s inclination.

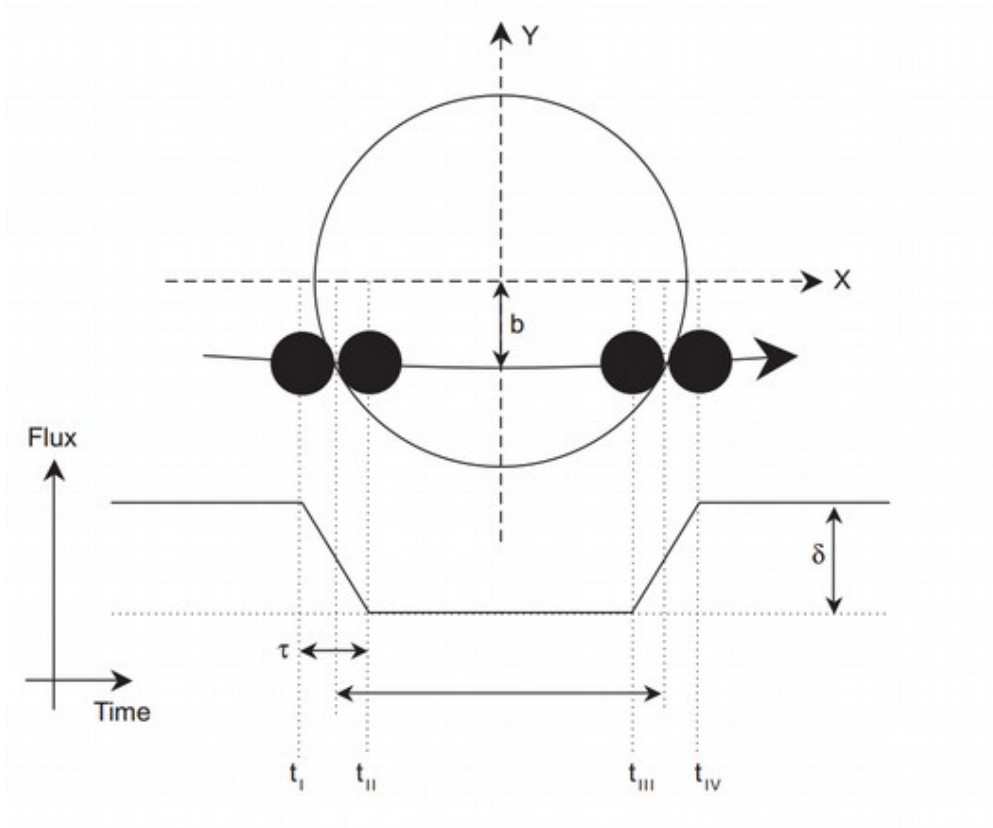


Fig. 7.—: A diagram of a simplified transit. The trapezoidal shape of the transit is apparent. Reproduced from Winn (2010).

1.2.2. Limb-Darkening

In actuality, the flat bottom of the trapezoid is not actually flat. As the planet blocks portions of the star at different radial distances from the star's center, the depth of the baseline varies; near the limbs of the star the baseline is shallower, near the center of the star the baseline is deeper. This is the result of an effect called limb-darkening, which is a lessening in brightness near the edges of a star's projected disc. This effect is due to the optical depth of the star reaching unity at shallower (and cooler) depths near the stellar limb, since the angle between the star's surface and the observer's line of sight is highly oblique near the limbs. Because observed light is emitted from shallower regions of

a star near its limbs, and because stars tend to be cooler (and therefore darker) at greater radial distances from their center, the limbs of a star’s disc appear to be darker than the star’s center. There are many models that can be used to fit limb-darkening, such as linear (Schwarzschild & Villiger 1906), quadratic (Kopal 1950), exponential (Claret & Hauschildt 2003), logarithmic (Klinglesmith & Sobieski 1970), square-root (Diaz-Cordoves & Gimenez 1992), three-parameter nonlinear (Sing et al. 2009), or four-parameter nonlinear (Claret 2000).

1.2.3. Learning about the Stellar Surface

Transits can also reveal details about the surface of the host star. The passage of a planet across the stellar disc provides a one-dimensional scan of the stellar surface, which can reveal the sizes and locations of starspots and plage. If the planet’s orbital plane is highly misaligned to the stellar rotation, then a large fraction of the stellar surface may be scanned by the planet’s shadow at some time or another. Over long timescales, after many transits, all regions of the star between a certain northern and southern stellar latitude will be blocked by the transiting planet. If observations can be carried out over this timescale, a map of starspots, plage, and other active stellar regions can be recreated, and the evolutionary timescale of such features can be analyzed. Such observations will also allow for strong constraints on the spin-orbit misalignment (Sanchis-Ojeda et al. 2012).

1.2.4. Rossiter-McLaughlin Effect

If the planet-to-star radius ratio is high enough and the star is rotating quickly enough, a transit may induce a measurable Rossiter-McLaughlin (RM) effect. The RM effect is a small variation in the RV induced as the planet crosses different parts of the star during

transit. When the planet blocks the receding side of its star, the light it blocks is redshifted light, which induces a slight, net blueshift in apparent velocity of the star. The opposite occurs for the approaching side of the star. By collecting multiple RV measurements during transit, observers can place constraints on the rotational velocity of the star as well as obliquity (the sky-projected angle between the axis of planetary orbital motion and the stellar rotation axis). Measurements of the latter have yielded very interesting findings on planetary system evolution; for example, Albrecht et al. (2012) found with obliquity measurements that hot Jupiters likely form misaligned to their host stars, but eventually become well-aligned through tidal interactions (more quickly for cooler stars). Additionally, in the same way that transits act as a one-dimensional scan of the stellar surface with *photometry* (see section 1.2.3), measurements of the RM effect provide a one-dimensional scan of the stellar surface with *spectroscopy*.

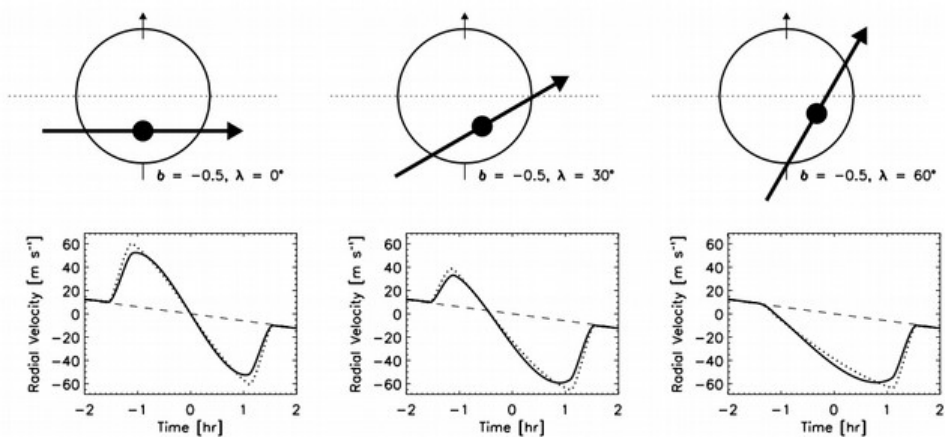


Fig. 8.—: A demonstration of the Rossiter-McLaughlin effect at three different obliquities. Reproduced from Gaudi & Winn (2007).

1.2.5. *Secondary Eclipses*

In addition to the transit, there may also be a secondary eclipse, in which the planet passes behind the face of the star (see Fig. 9). Because the planet is much dimmer than the star, the secondary eclipse is often too faint to detect. However, with sufficiently high precision (and depending on the observation wavelength), sometimes a secondary eclipse can be detected. This gives the observer a few useful pieces of information. For one, it can completely constrain the eccentricity and argument of the periastron of the exoplanet. If the planet has zero eccentricity, the time of the secondary eclipse will be at exactly halfway between the prior and subsequent transits. However, if the planet has sufficiently nonzero eccentricity, and the periastron is not aligned with the star and the observer, then the time of the secondary eclipse will be either earlier or later than the halfway mark between transits. Further, the length of the duration of the secondary eclipse provides further information. Using both the time of the eclipse and the duration of the eclipse allows the eccentricity and argument of the periastron to be fully constrained.

1.2.6. *Atmospheric Characterization*

Further, secondary eclipses reveal information about the exoplanet’s atmosphere. The depth of the secondary eclipse will vary at different wavelength ranges due to wavelength dependent changes in emission from the planet. This is due to various molecules acting to increase or decrease reflectivity and transmission at certain wavelengths. Thus, measuring a secondary eclipse at multiple wavelength ranges can provide insights into absorption features of dominant molecules.

The other way to learn about a planet’s atmosphere is through the primary transit, as some starlight passes through an annulus of atmosphere around the exoplanet (see Fig. 9).

Because only certain wavelengths of light can pass through the atmosphere (based on its composition), taking the difference between stellar spectra inside and outside of transit can show how planetary opacity varies with wavelength, providing insights on atmospheric composition. Thus far, this method has yielded the detection of many molecules including Na, K, CO, CO₂, CH₄, H₂O for multiple hot Jupiters (Sing et al. 2016, Charbonneau et al. 2002, Swain et al. 2009a, Swain et al. 2009b, Swain et al. 2008). The method is also expected to yield spectroscopic details of numerous terrestrial planets with JWST (Greene et al. 2016, Belu et al. 2011).

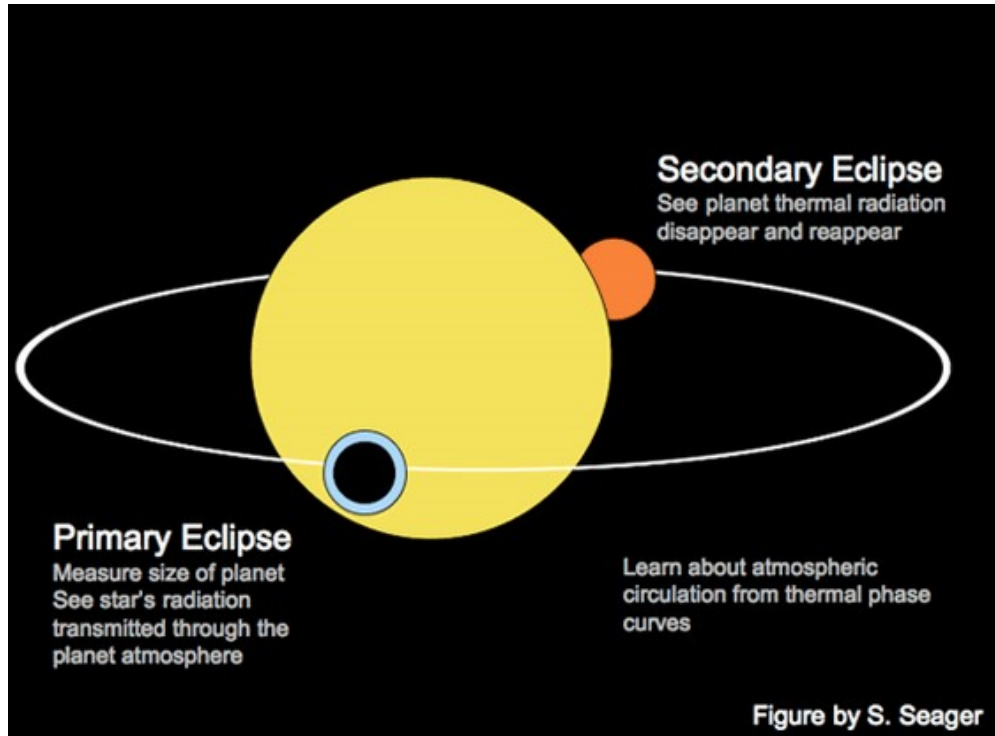


Fig. 9.—: Atmospheric characterization of exoplanets can be performed two ways: 1) analyzing the opacity of the atmosphere as a function of wavelength via planetary radius (including atmosphere, represented by the blue ring in the figure), or 2) observing the wavelength dependent depth of the secondary eclipse, when the planet passes behind its star.¹

¹ The current version of this figure was produced by Sara Seager. The original version was produced by Tim Brown. As Tim Brown explains in a private communication: “I sketched out the first version of this figure

1.3. The *Kepler* Mission

Arguably, the most important moment in the history of exoplanet science, other than the discovery of the first exoplanet, was the beginning of the *Kepler* mission (Borucki et al. 2008). Launched in 2009, the *Kepler* space telescope was designed to stare at over 100,000 stars in a single patch of sky for 3.5 years in order to look for transits.

1.3.1. *Kepler's Accomplishments*

The *Kepler* mission has been an overwhelming success. According to the NASA Exoplanet Archive (exoplanetarchive.ipac.caltech.edu, 20 Feb. 2017), it is currently responsible for 2331 verified exoplanets, more than every other exoplanet survey combined. *Kepler* has greatly expanded our understanding of the exoplanet population. It has led to the discovery, characterization, and understanding of new exoplanet populations such as mini-Neptunes and super-Earths. It has also populated the parameter space of transiting exoplanets at longer periods than ever before and across a wide range of masses, from Earth-mass planets to brown dwarfs and even larger, with more than two thousand detected eclipsing binaries. *Kepler* has also discovered numerous compact, multiplanet, highly coplanar systems, as well as a handful of circumbinary planets (planets orbiting two stars), such as Kepler-16b (*Kepler's* first circumbinary planet; Doyle et al. 2011), and Kepler-1647b (its most recent; Kostov et al. 2016). Further, *Kepler* is responsible for the discovery of the first Earth-sized exoplanet orbiting in its star's habitable zone (Kepler-186f; Quintana et al. 2014).

in PowerPoint sometime in the early '00s, and used it in a few talks, but never that I recall published it anywhere. I think Dave Charbonneau had a very slightly modified version that he used here and there, and may have published in some proceedings or other. Being Dave, he was punctilious about including a notation giving the provenance. But other people picked it up, and pretty soon there were slightly modified versions all over, and I gave up on the idea of getting the attribution right.”

Additionally, *Kepler*'s vast quantities of high cadence photometry was an enormous boon to the astroseismic community (Gilliland et al. 2010). Asteroseismology involves the study of stellar interiors through the analysis of stellar oscillation modes. These modes have periods on minute to hour timescales, and high cadence *Kepler* photometry collects data approximately once per minute at the level of tens of parts per million. As a result of such high precision, long timescale data, stellar interiors can now be studied with unprecedented precision and constraints on stellar density can be greatly improved.

Kepler also provided sufficient data to allow astronomers to calculate eta-Earth for M-Dwarfs, that is, the fraction of M-Dwarf stars that host Earth-sized, habitable planets (Dressing & Charbonneau 2013). The most recent estimate of eta-Earth for M-Dwarfs is roughly 0.16 for a strict habitable zone, 0.24 for a generous habitable zone (which allows for recent Venus to early Mars insolation boundaries; Dressing & Charbonneau 2015).

It should be mentioned that one of the primary goals of the *Kepler* mission was to assess eta-Earth for G-stars, i.e. the frequency of Earth-sized planets orbiting Sun-like stars. It was initially estimated that a good characterization of this value could be made within the mission lifetime. Unfortunately, noise from both stars and the telescope proved greater than initially expected. As it stands, very rough estimates of eta-Earth for G-stars do exist (Petigura et al. 2013). However, the error bars for these estimates are very large and need significant improvement.

1.4. The K2 Mission

1.4.1. From *Kepler* to *K2*

In 2013, the second of the *Kepler* spacecraft's four reaction wheels failed, preventing the spacecraft was looking at its designated field and bringing an end to the original

mission. Fortunately, a follow up survey, called K2, was developed that used the spacecraft’s thrusters as a makeshift third reaction wheel (Howell et al. 2014). The *Kepler* spacecraft fires its thrusters approximately once every six hours to maintain an unstable equilibrium and keep the telescope pointing toward a field in the ecliptic plane. (For this reason, the spacecraft cannot look at the original *Kepler* field, since it is too far from the ecliptic plane.) The field must lie in the ecliptic plane in order to balance solar pressure along the spacecraft’s roll axis. However, in order to keep the spacecraft’s solar panels pointed toward the Sun and to prevent sunlight from entering the telescope, the spacecraft must shift to a new ecliptic field every ~ 83 days (roughly 75 of those days are devoted to science). A comparison of the photometric sensitivities achieved by the *Kepler* and K2 missions can be seen in Fig. 10. For bright stars (brighter than 12.5 in *Kepler* magnitude), proper reduction of K2 data gives the same photometric precision as for *Kepler* (assuming the application of effective systematics correction techniques).

The K2 mission has thus far been very fruitful; according to the NASA Exoplanet Archive (exoplanetarchive.ipac.caltech.edu, 14 Mar. 2017), K2 has a current yield of 520 planet candidates, 34 of which have mass or $m \sin i$ estimates. A major benefit to K2 that *Kepler* lacked is that K2 looks at multiple patches of the sky, so with each new campaign there are new bright targets available for follow-up (such as RV measurements or transmission spectroscopy) and there are also more opportunities to detect rare objects or events due the greater overall sky coverage.

1.4.2. Bridging Kepler and TESS

Because of its campaign format, K2 will help to bridge the gap between the *Kepler* mission and the upcoming TESS mission, slated for launch March-June 2018. Whereas the *Kepler* mission involved 3+ years of data collection on a single field (covering approximately

1/400 of the sky), TESS will scan almost the entire celestial sphere over the course of ~ 2 years, split into 26 campaigns each lasting 27.4 days (Ricker et al. 2015). K2 is nestled nicely between these two extremes, with $\lesssim 20$ campaigns lasting ~ 75 days each. As a result, observers have had an excellent chance to prepare for the type of modeling and follow-up that will be required for an all-sky exoplanet survey. Lastly, the original *Kepler* mission had a proprietary period during which the *Kepler* team had exclusive access to the data. Unlike *Kepler*, neither TESS nor K2 have a propriety period (although TESS will produce its own candidate lists like *Kepler*). Therefore, K2 is providing astronomers with a chance to prepare for the TESS mission by learning now how to handle frequent deliveries of new batches of transiting planet candidates.

1.5. Planet Validation

The main goal of this thesis is the validation of exoplanet candidates from campaigns 0 through 10 of the K2 mission. The difference between an exoplanet candidate and a validated exoplanet is very important. With the original *Kepler* mission, an exoplanet candidate was a transit signal that had passed a battery of astrophysical and instrumental false positive tests. Now, however, the usage is looser; the term is commonly used to refer to any exoplanet signal that a particular team has identified as a possible planet. So long as the reasoning is sound and the results are published, the signal is effectively a candidate. A validated planet is a candidate that has been vetted with follow-up observations and determined quantitatively to be far more likely an exoplanet than a false positive (according to some likelihood threshold). Note that validation is not the same thing as confirmation, which is ideally attained through a reliable mass determination. Confirmation is more rigorous than validation, in the same way that validation is more rigorous than candidacy. Confirmation is usually accomplished via the RV method, the TTV method, or, less

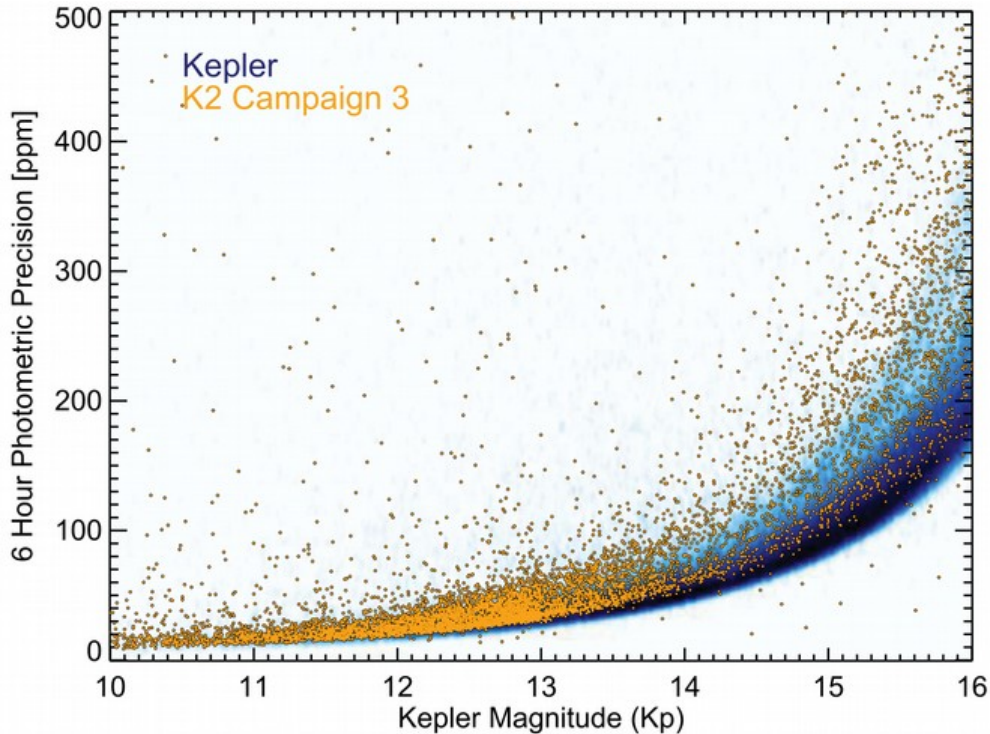


Fig. 10.—: A comparison of *Kepler* and K2 precision. Blue dots represents *Kepler* targets, while orange dots represent K2 Campaign 3 targets. With the proper reduction techniques to account for thruster firing and other noise sources, K2 precision approaches that of *Kepler*, and is essentially equal at magnitudes brighter than $K_p = 12.5$. Reproduced from Vanderburg et al. (2016a).

commonly, methods such as a full photo-dynamical modeling solution (e.g. Carter et al. 2011) or Doppler tomography (e.g. Zhou et al. 2016).

Validated planets, because confidence in their planethood is higher than for a regular candidate, are far more promising targets than planet candidates for follow-up observations, characterization, and eventual confirmation.

1.5.1. VESPA

When the transit method began to yield its first exoplanet detections, validation referred to an extensive process which could involve spectroscopy and photometry from multiple observatories, RV measurements, and AO observations. In other words, “validation” used to refer to what is now considered confirmation. An excellent example of this is TrES-1b (Alonso et al. 2004), for which the initial transit signal was followed up with AO imaging in two bands, seven epochs of medium resolution spectroscopy, additional transit photometry at three facilities in seven filters, and high-precision RV measurements. All of this follow-up was required to rule out certain false positives scenarios, primarily background or hierarchical eclipsing binary star systems.

Today, however, validation is an intermediate step to confirmation; a complete orbital solution or supplementary method of detection is not required (as it would be for confirmation). Instead, validating a planet means quantitatively comparing the true positive scenario and various false positive scenarios (and finding the true positive scenario to be very likely).

With the rush of new exoplanet data delivered by *Kepler*, a number of standardized validation methods have been developed to handle the influx of candidates, such as BLENDER (Torres et al. 2011) and PASTIS (Planet Analysis and Small Transit Investigation Software; (Díaz et al. 2014)). BLENDER was the first validation method for *Kepler* and served as the workhorse for *Kepler* data before other validation techniques were developed. The method that will be discussed and applied in this thesis is called VESPA, or Validation of Exoplanet Signals using a Probabilistic Algorithm. VESPA is a public package (Morton 2015) based on the work of Morton (2012). It operates within a Bayesian framework and calculates the False Positive Probability (FPP), the likelihood that a candidate is a false positive rather than a true positive.

The method described by Morton (2012) can quantify the FPP of a planet candidate by incorporating any amount of follow-up for the candidate. In other words, it can determine whether transit data alone are sufficient to validate the candidate or whether additional spectroscopy and/or high-contrast imaging is required as supplement. A spectrum will allow VESPA to rule out particularly unlikely portions of parameter space, which may either increase or decrease the FPP depending on whether the ruled out regions are predominantly populated with true positives or false positives. Similarly, high-contrast imaging helps VESPA determine the likelihood of a hidden companion to the target star by supplying limits on the maximum brightness of an unseen companion at a given projected separation from the target. (As the contrast of an image increases without detecting a companion, the parameter space within which a companion can hide decreases and thus the FPP also decreases.) With this Bayesian approach, Morton (2012) found that rigorous follow-up with multiple observatories and methods of observations is often overkill, and that transit data supplemented with a single spectrum and a single high-contrast image are often more than enough to validate a candidate (and sometimes even less than that is sufficient).

There are a few key components of VESPA that make its validation procedure effective. For one, VESPA takes into account both the depth and the shape of the transit (via the transit duration and the ingress/egress slopes). This helps distinguish star-sized objects from planet-sized objects, as the former tend to have a pronounced V-shaped transit while the latter typically have a characteristic trapezoidal transit shape (more so for smaller planets). However, it should be noted that transit shape is not always enough, as Jupiter-sized planets can have very similar transit shapes to small stars (which can be somewhat similar in size).

Additionally, VESPA is very fast compared to other validation methods such as BLENDER. VESPA can complete its validation analysis in only approximately 10 minutes

with modest computational facilities such as a modern laptop computer (Morton 2012), while BLENDER could require many thousands of CPU hours to operate on a candidate. VESPA accomplishes this gain in speed by applying a simpler, less comprehensive algorithm than BLENDER. Rather than rigorously address every imaginable false positive scenario, VESPA considers only the most common scenarios, including:

1. A background (or foreground) eclipsing binary (BEB) blended with the target star
2. A hierarchical eclipsing binary (HEB) system
3. A single eclipsing binary (EB) system
4. A non-associated, blended background/foreground star with a transiting planet (Bpl)

Although the parameter space considered by VESPA may not be as complete as that of BLENDER, VESPA is still very comprehensive, considering most plausible scenarios leading to a false positive.

1.5.2. Data Used for this Validation

In this thesis, information such as planetary radius, planetary period, and stellar density are determined from transits; stellar rotational velocity, temperature, and surface gravity are determined from a stellar spectrum; and the likelihood of stellar companions of various brightnesses as a function of projected separation is determined through high-contrast imaging. All of this information is then used by VESPA in order to calculate the FPP.

All of the transit data used are from the K2 mission. A transit fitting routine was developed specifically for the validation work done in this thesis, which models key transit parameters for single- or multiplanet systems using a Monte Carlo Markov Chain (MCMC)

process using an affine invariant ensemble sampler (Goodman & Weare 2010) with the emcee Python package (Foreman-Mackey et al. 2013). (The transit model is described in greater detail in section 4.1.2.) After instrumental systematics are removed from the K2 data, this model is applied to the K2 photometry in order to extract the relevant transit parameters. Additionally, all planet candidates that undergo the validation process in this thesis have a stellar spectrum supplied by the Tillinghast Reflector Echelle Spectrograph. This is one of two spectrographs for the 1.5 meter Tillinghast telescope at the Whipple Observatory on Mt. Hopkins in Arizona. For each spectrum, the Stellar Parameter Classification technique (Buchhave et al. 2012) is applied in order to extract spectroscopic parameters. Further, the majority of high contrast imaging is collected with the Differential Speckle Survey Instrument (Horch et al. 2009) on the 3.5-m Wisconsin-Indiana-Yale-NOAO (WIYN) telescope or the Gemini-South 8.1-m telescope.

For our research, 197 exoplanet candidates suitable for validation were identified from K2 campaigns 0-10 (henceforth C0-C10) using the candidate pipeline applied to campaigns 0-3 in Vanderburg et al. (2016a) (henceforth V16). As will be discussed in the body of this thesis, planets fainter than 13th magnitude are less appealing or outright impossible targets for precise radial velocity follow-up (i.e. mass determination) with many of the best modern facilities (such as HARPS-N at TNG and HIRES at Keck I; Marcy et al. 2014). Therefore, candidates with host stars fainter than approximately 13th magnitude were not observed with the TRES spectrograph (on the 1.5-meter Tillinghast telescope). Approximately half of the candidate sample is fainter than 13th magnitude, and therefore do not have spectra and do not undergo validation.

1.5.3. *Format of this Thesis*

The body of this thesis will have the following format. Section 2 will be a discussion of the work to develop the exoplanet candidate list. Section 3 will detail the supporting observations used in the validation process. Section 4 will describe the analysis of the K2 light curves and the follow-up spectroscopy and high-contrast imaging. Section 5 will discuss how VESPA is applied to a planet candidate. Section 6 will present the results of the validation process for in detail for a single planet, then in general for all candidates, followed by an investigation of population statistics for the newly validated exoplanets. Section 7 will be a discussion of the broader impacts of this research. Lastly, Section 8 will be a summary and conclusion.

2. Pixels to planets

In this section, we first explain how K2 observations are collected, then we describe the process by which systematic errors are removed from K2 data, and finally we discuss analysis of the corrected K2 data in order to identify planet candidates.

2.1. K2 Observations

Since 2014, the K2 mission has served as the successor to the original *Kepler* mission. Working with only two of the *Kepler* spacecraft’s original reaction wheels, K2 is constrained to observations along the ecliptic plane. Additionally, the spacecraft can only point toward a given field for approximately 83 days before moving (in order to keep sunlight on the spacecraft’s panels and out of its telescope), which divides K2 observations into “campaigns” corresponding to each field.

Due to on-board data storage constraints, not all data collected by the CCD cameras can be retained and transmitted to the ground. As a result, targets must be identified within each campaign field prior to observation so that non-target data can be discarded and a postage stamp (a small group of pixels) around each target can be saved and transmitted to the ground.

In the original *Kepler* mission, planet search targets were mostly selected pre-launch with the primary objective of determining the frequency of Earth-like planets orbiting Sun-like stars (Batalha et al. 2010) (although some planet search targets were selected during mission adjustments, and there was a Guest Observer program for secondary science objectives). However, K2 operates in a very different manner. For each K2 campaign, targets are exclusively selected through the Guest Observer (GO) program, which evaluates observing proposals submitted by the astronomical community for any scientific objective, not just exoplanet related objectives. Ideally, GO proposals have scientifically compelling goals that can be achieved through K2 observations and cannot easily be achieved with other instruments or facilities.

In each K2 campaign, the number of targets ranges between 10,000 and 30,000 with long cadence observations, and about 50 to 200 with short cadence observations. Exceptions include C0, which served primarily as proof-of-concept campaign to show that the K2 mission was viable, and C9, which focused on microlensing targets in the Galactic Bulge. Both C0 and C9 had fewer targets than normal in both long cadence and short cadence. It should also be noted that there are occasional minor overlaps between campaign fields (as well as a significant overlap between C5 and the planned C16). Despite fewer, new observation targets, overlaps provide a longer baseline of observations for targets of interest in the overlapping region.

K2 observations are strongly appealing to observers due to their long baseline, extreme

high-precision photometry: the *Kepler* spacecraft collects long cadence (≈ 30 minute integration) and short cadence (≈ 1 minute integration) observations. In a single campaign alone (C12, to be precise), K2 has conducted observations in support of research on exoplanets, binary stars, flare stars, white dwarfs, quasars, variable stars, hypervelocity stars, asteroseismology, giant stars, blazars, and extragalactic transients.

This paper focuses on Campaigns 0 through 10. However, the process implemented in this research can easily be extended and applied to additional K2 campaigns.

2.2. K2 Data Reduction

Because of the loss of two reaction wheels, the *Kepler* telescope is perpetually drifting off target and must be regularly corrected by thruster fires, causing shifts in the orientation of the photometric aperture. These shifts, coupled with variable sensitivity between pixels on the telescope’s CCD camera, lead to systematic variations in apparent stellar brightness, introducing noise into the photometric measurements. Howell et al. (2014) estimated that raw K2 precision is roughly a factor of 3-4 times worse than *Kepler*’s original precision (depending on stellar magnitude). Fortunately, an understanding of the motion of the *Kepler* spacecraft allows for modeling and correction of the induced systematic noise.

This thesis relies on the method of systematic correction described in Vanderburg & Johnson (2014) (hereafter referred to VJ14). Andrew Vanderburg performed the photometric reductions using this method, which we describe here. The first part of the method in VJ14 was selecting an appropriate aperture with which to analyze the pixel-level K2 data. Ten circular aperture masks of varying sizes were tested, as well as ten aperture masks shaped like the *Kepler* pixel response function and defined by varying cutoffs for each pixel’s flux. Whichever of these 20 aperture masks provided the best photometric precision

upon completing the data reduction was the mask selected. Photometric precision was only estimated after the thruster systematics were removed as well as low-frequency variations were removed (using a basis spline, or B-spline with breakpoints at 0.75 days). Within a running bin, the standard deviation of 13 adjacent long-cadence measurements was made, then the median value was divided by $\sqrt{13}$ and reported as the photometric precision. It's important to note that because photometric precision was not estimated until after data reduction, the data reduction steps below were performed 20 times, each with a different mask, and then a single "best" mask was selected based on its photometric precision.

So, with any given mask, the next step was to calculate the flux for each frame. VJ14 accomplished this by first subtracting the median background flux from the image (if not already done by the *Kepler* pipeline; this varied from campaign to campaign). Then, the remaining flux within the aperture mask was summed together.

Additionally, the motion of each star across the CCD was estimated by determining the centroid position of a single bright star in the campaign field. This was done (instead of individually measuring each star's apparent motion) because it improved the robustness of the reduction process, particularly for faint stars, stars with high background flux levels, and stars with nearby companions. The centroid position was calculated in two ways: 1) finding the weighted mean position (by photon count) along the x and y axes, and 2) fitting a multivariate Gaussian to the image of the star. The two methods were then compared by calculating their root-mean-squared residuals along both axes after fitting a fifth order polynomial; the method with the smaller residuals was selected.

The next step was to exclude certain data points. Data with undesirable values of the QUALITY tag in the *Kepler* FITS file data structure (produced by the *Kepler* pipeline) were excluded. Additionally, any data collected while the *Kepler* on-board thrusters were firing were excluded. In order to determine which points were collected at such times, a

method similar to principle component analysis was applied to the centroid positions in order to find the curve along which the centroid moved. Once this curve was identified, the position of the centroid along this curve, or the centroid’s “arclength”, was calculated. Then, the time derivative of arclength was calculated for each data point, a distribution for this value was created, and those data points with variations greater than 5σ discrepant from the mean of the distribution were excluded. (After Campaign 3, thruster firing events were identified by the *Kepler* team, so this step was unnecessary for subsequent campaigns.)

The remaining data points exhibited regular drifting in flux and centroid position over the course of ≈ 6 hour timescales, separated by discontinuities (thruster fires) that corrected the drift. To remove the drift, an iterative method of low-frequency fitting and high-frequency removal was employed. First, low frequencies were removed by fitting the data with a basis spline (B-spline) with breakpoints every 1.5 days. The second step was to plot the arclength along the centroid position curve against brightness and fit the relationship using a piecewise function (with either 15 or 25 segments). Outliers were ignored in this fitting process to preserve any transits in the data. Third, for each data point, its arclength position was used to find the corresponding model flux according to this piecewise function; the measured flux of the data point could be corrected by dividing by the model flux. Fourth, this correction was applied to the all of the original raw flux data (without low-frequency variations removed). Subsequently estimating the low-frequency variations typically resulted in a much better fit, since most of the roll systematics were now removed. So the fifth step was to repeat the process beginning at step one, only this time using the improved estimate of low-frequency variations. This process typically only required one or two iterations, but five iterations were performed for the sake of rigor. An example of a light curve before and after the data reduction process described here can be seen in Fig. 11.

It should be noted that this method relied on the regular back-and-forth motion of the spacecraft to trace out the same curve every time, so that arclength could be accurately determined. However, on timescales longer than 5-10 days, the spacecraft began exhibiting noticeable motion transverse to the centroid position curve. Therefore, the high-frequency correction steps of the above data reduction process were applied to light curve segments of 5-10 days (the low frequency steps were applied to the full light curve).

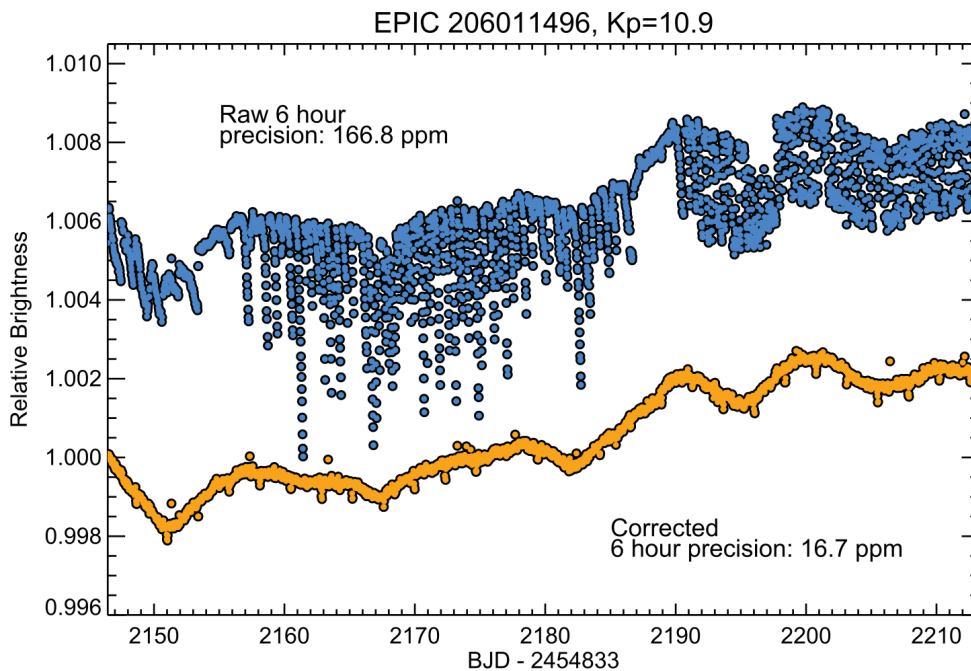


Fig. 11.—: Example of the K2 systematics reduction process on a single light curve. The blue points show the light curve before correcting for the systematics induced by the roll motion of the *Kepler* spacecraft, while the yellow points show the same light curve after those systematics have been removed via the data reduction process described in this work. Reproduced from Vanderburg et al. (2016a).

2.3. Identifying K2 Candidates

Once the roll systematics were removed from the photometry according to the method described by VJ14, a transit search was conducted for each K2 target by Andrew

Vanderburg using the method of V16. The first step was to remove low-frequency variations through a B-spline with breakpoints every 0.75 days. Once those variations were removed, we next removed any 4σ upwards outliers as well as the two worst downward outliers (we didn’t remove more downward outliers so as to preserve transit events). Next, we calculated a box-least-squares (BLS) periodogram (Kovács et al. 2002) on periodic signals ranging from 2.4 hours to half the length of the campaign. The spacing between investigated periods was determined by

$$\Delta P = P \frac{D}{N \times T_{\text{tot}}}$$

where ΔP is the spacing between periods evaluated in the periodogram, P is the period tested, D is the transit duration expected at that period, N is an oversampling factor to insure the frequency space is robustly explored, and T_{tot} is the total duration of K2 observations (for a given campaign).

After cleaning the resulting BLS periodogram of excess noise at low frequencies, the S/N ratio was calculated and all signals with $\text{SNR} > 9$ and a positive depth (i.e. a periodic *decrease* in brightness) were investigated. Detections lasting longer than 20% of the period or detections of a only single data point were removed and the BLS periodogram was then recalculated. After that, the depth of the putative transit was calculated without its lowest point to see if the depth changed by over 50%; if it did, that point was removed, the BLS periodogram was recalculated and the process repeated.

Any detection passing these tests was deemed a “Threshold Crossing Event” (TCE). Each TCE was fit with the Mandel & Agol (2002) transit model to estimate transit parameters, then the TCE was removed from the light curve, and then the BLS periodogram was recalculated. Once all TCEs had been identified, they subsequently underwent “triage”, in which each candidate was inspected by eye in order to remove obvious astrophysical and instrumental false positives from subsequent analysis. Candidates identified as neither type

of false positive passed the triage phase and moved on to a “vetting” phase in the form of more rigorous tests, which are described below:

1. The times of a TCE’s “in transit” points were compared against the position of the *Kepler* spacecraft at those times, as many false positives were composed of data points near the edges of *Kepler*’s rolls where the data reduction method was less well constrained.
2. Multiple apertures were tested to see if each TCE persisted, as certain systematics were particular to specific aperture sizes or types. Additionally, multiple apertures helped show whether a TCE was from another nearby star partially inside or just outside the photometric aperture.
3. Individual transits of a TCE were visually inspected, since instrumental false positives were less likely to have consistent, planet-like transit depths or shapes.
4. Flux centroid motion, relativistic beaming, ellipsoidal variations, and secondary eclipses were all searched for as evidence of astrophysical false positives.

This battery of vetting tests was conducted through visual inspection of a collection of diagnostic plots. I conducted the vetting procedure for C4-C10 (candidates were already vetted in this manner in V16). an example of which can be seen in Fig. 12 and Fig. 13 (in fact, the candidate in these figures is the example candidate we validate in section 6.1).

Any TCE surviving all of these vetting stages was promoted to “planet candidate”. These candidates were then subjected to our validation process, assuming a converged solution for transit parameters could be found and assuming there were sufficient follow-up observations of the candidate (spectroscopy and high-resolution imaging in particular; see section 3 for more details). Parameters for the 197 candidates that satisfied these requirements and were subjected to validation are listed in Table 2. Their associated stellar

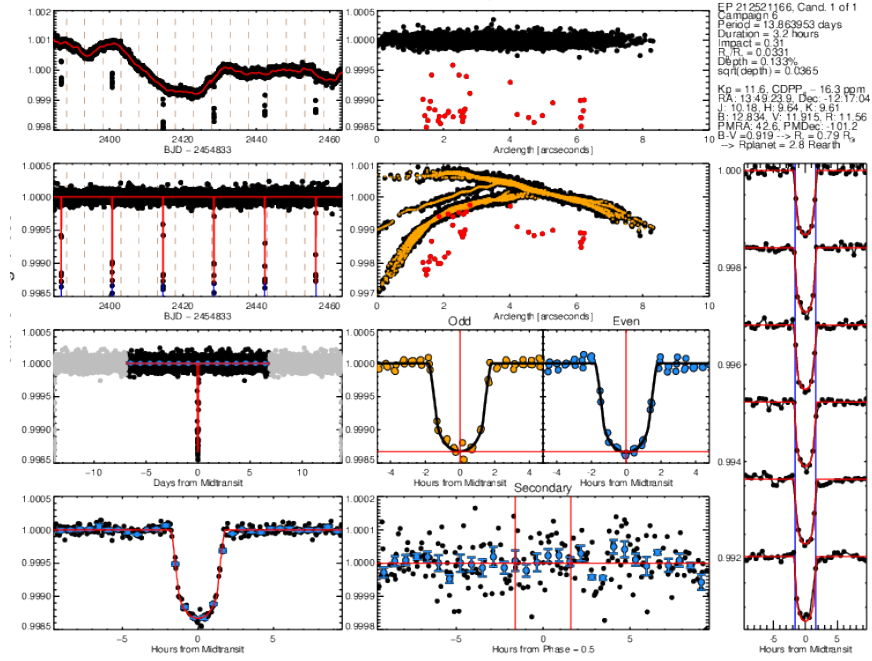


Fig. 12.— Diagnostic plots for EPIC 212521166.01. Left column, first (top) and second rows: K2 light curves without and with low frequency variations removed, respectively. The low frequency variations alone are modeled in red in the first row, whereas the best-fit transit model is in red in the second row. Vertical, brown, dotted lines denote the regions into which the light curve was separated to correct roll systematics. Left column, third and fourth rows: phase-folded, low frequency corrected K2 light curves. In the third row, the full light curve is shown (points more than one half period from the transit are gray), whereas in the fourth row, only the light curve near transit is shown. The red line is the best-fit model and the blue points are binned data points. Middle column, first and second rows: Arclength of centroid position of star versus brightness, after and before roll systematics correction respectively. Red points denote in transit data. In the second row, small orange points denote the roll systematics correction made to the data. Middle column, third row: separate plotting and modeling of odd (left panel) and even (right panel) transits, with orange and blue data points respectively. The black line is the best-fit model, the horizontal red line denotes the modeled transit depth, and the vertical red line denotes the mid-transit time (this is useful for detecting binary stars with primary and secondary eclipses). Middle column, fourth row: light curve data in and around the expected secondary eclipse time (for zero eccentricity). Blue data points are binned data, the horizontal red line denotes a relative flux = 1, and the two vertical red lines denote the expected beginning and end of the secondary eclipse. Right column: up to 30 individual transits (vertically shifted from one another) with the best fit model in red and the vertical blue lines denoting the beginning and end of transit.

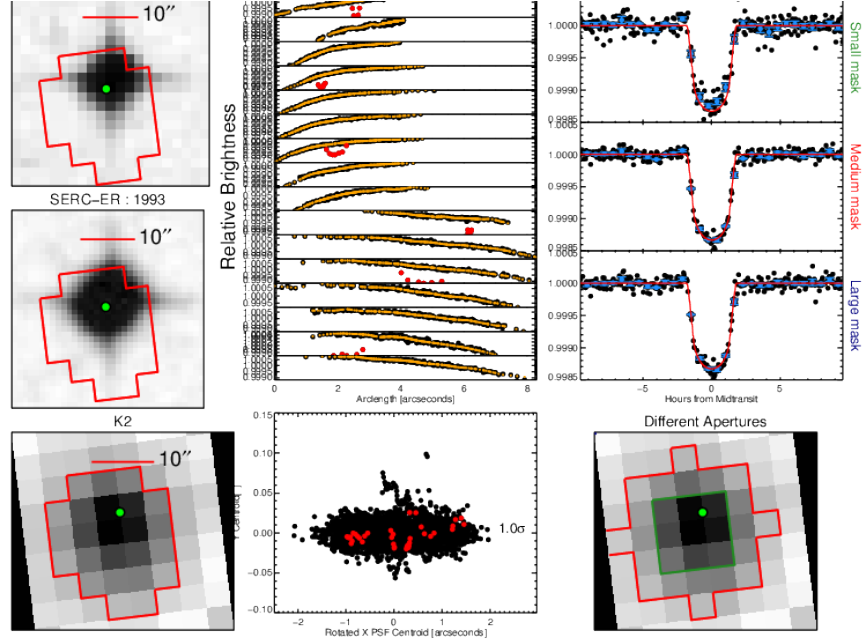


Fig. 13.—: Diagnostic plots for EPIC 212521166.01. Left column, first (top), second, and third rows: images from the first Digital Sky Survey, the second Digital Sky Survey, and K2 respectively, each with a scale bar near the top and an identical red polygon to show the shape of the photometric aperture chosen for reduction. The K2 image is rotated to match the orientation of the other two images. Middle column, top row: multiple panels of uncorrected brightness versus arclength, chronologically ordered and separated into the divisions in which the roll systematics correction was calculated. In-transit data points are red, orange points denote the brightness correction applied to remove systematics. Middle column, bottom row: variations in the centroid position of the K2 image. In-transit points are red. The discrepancy (in standard deviations) between the mean centroid position in-transit and out-of-transit is shown on the right side of the plot. Right column, first row: the K2 light curve near transit as calculated using three differently sized apertures: “Small mask” (top panel), “Medium mask” (middle panel), and “Large mask” (bottom panel), each with the identical best-fit model in red. Aperture-size dependent discrepancies in depth could suggest background contamination from another star. Right column, third row: the K2 image overlaid with the three masks from the previous plot shown (in this figure, the large mask is fully outside the postage stamp and is therefore not visible).

parameters are listed in Table 3.

3. Supporting Observations

In this section, we describe the types of follow-up observations that are typically used to improve our validation results. We first discuss stellar spectroscopy via the Tillinghast Reflector Echelle Spectrograph, followed by speckle imaging from the Differential Speckle Survey Instrument at the Wisconsin-Indiana-Yale-NOAO telescope.

3.1. The Tillinghast Reflector Echelle Spectrograph

As mentioned in section 1, the spectra used in this research were obtained by the Tillinghast Reflector Echelle Spectrograph (TRES). TRES has a resolving power of $R=44,000$ and is one of two spectrographs for the 1.5 meter Tillinghast telescope at the Whipple Observatory on Mt. Hopkins in Arizona. TRES was used to collect spectra for all planet candidates that underwent the validation process. Unfortunately, almost no candidates dimmer than 13th magnitude (in the *Kepler* band) were observed with TRES because of the lengthy integration time required to collect a spectrum and the difficulty of subsequent follow-up observations by other facilities. In fact, this was the primary limiting factor for the validation work in this paper: approximately half of the candidates were fainter than 13th magnitude in the *Kepler* band and therefore are not subjected to our validation process.

3.2. Speckle Observations

Most of our planet candidates had associated speckle imaging from either the 3.5-m Wisconsin-Indiana-Yale-NOAO (WIYN) telescope or the Gemini-South 8.1-m telescope. Although the speckle data came from two different telescopes, both made use of the same speckle imaging instrument, called the Differential Speckle Survey Instrument, or DSSI

(Horch et al. 2009), an instrument that travels between different telescopes.

An instrument like DSSI operates by taking numerous short exposure images (40 milliseconds for WIYN + DSSI) in order to largely freeze out atmospheric turbulence fluctuating on the many millisecond level (Roddier 1981). Each frame in the image stack is autocorrelated (correlated with itself) and triple correlated (correlated with itself *twice* simultaneously), and the resulting functions are averaged over the entire stack. The Fourier transforms of the averaged autocorrelation and triple correlation functions are the power spectrum and bispectrum. The difference between the power spectrum and a power spectrum of a calibration star is analyzed to constrain the angular separation, orientation, and brightness of any stellar companions to the target star. Then, using methods from Meng et al. (1990), the amplitude information from the power spectrum and the phase information from the bispectrum are used to reconstruct the image.

This data collection and reduction was performed for the majority of our selected K2 candidates. Further, many candidates were observed with WIYN in multiple bands, particularly 562 nm, 692 nm, and 880 nm, so in those cases we were able to make use of multiple high-contrast images in our validation work.

4. Data Analysis

Once all of the photometry had been reduced and all of the necessary follow-up observations had been collected, the next step was to analyze the data, calculate relevant parameters, and prepare the results for the validation process. In this section, we first explain the process of deriving parameters from our reduced light curves (to determine transit parameters and folded light curves), then our spectra (to calculate stellar parameters), and then our high-contrast images (to create contrast curves).

4.1. K2 light curves

4.1.1. *Simultaneous Fitting of Data Reduction and Transit Parameters*

In sections 2.2 and 2.3, we described the process of correcting K2 photometry for instrumental systematics and exploring the reduced light curves for candidates. Once those steps were complete, the planets candidate needed to be more thoroughly characterized. In order to assess transit and orbital parameters, the same process as that explained in V16 was followed. The first step was to re-derive the systematics correction while simultaneously modeling the transits in the light curve. This was done using code written by Andrew Vanderburg. As in the original systematics correction, the light curve was divided into multiple sections and applied the systematics correction to each section separately. A cubic spline was fit with breakpoints every ≈ 0.25 arcseconds to the arclength v. brightness relationship described in section 2.2 (arclength is a one-dimensional measure of position along the path an image centroid traces out on the *Kepler* CCD camera). The low-frequency variations in the light curve were modeled with a cubic spline (with breakpoints every 0.75 days), and the transits themselves were modeled with the Mandel & Agol (2002) transit model. The fit was performed using a Levenberg-Marquardt optimization (Markwardt 2009), and all of the parameters from the optimization (besides the transit parameters) were used in order to correct the systematics of the light curve (once again) and remove the low-frequency variations (once again). Since these parameters were determined in a *simultaneous* fit with the transits, the quality of the data reduction tended to be better.

4.1.2. *Final Estimation of Transit Parameters and Uncertainties*

The systematics-corrected, low-frequency extracted photometry now needed to be further analyzed in order to estimate final parameter values and their uncertainties. I

developed a transit model using the BATMAN Python package (Kreidberg 2015). My model assumed non-interacting planets with circular orbits. For each planet, I modeled five parameters: the epoch (i.e. time of first transit), the period, the inclination, the planetary to stellar radius ratio (R_p/R_*), and the semi-major axis normalized to the stellar radius (a/R_*). Additionally, I included a quadratic limb-darkening law (Kipping 2013), a parameter to allow the baseline to vary (in case there was an erroneous systematic offset from flux = 1 outside of transit), and a noise parameter that assigned the same uncertainties to each flux measurement (since flux error bars were not calculated in the K2 data reduction process). In systems with multiple planets, I fit all of the planets simultaneously, so that I could model overlapping transits.

For each candidate system, I measured the transit parameters in this model using emcee (Foreman-Mackey et al. 2013), a Python package which runs simulations using a Markov chain Monte Carlo (MCMC) algorithm with an affine invariant ensemble sampler (Goodman & Weare 2010). In each simulation, I sampled the parameter space with 30 walkers, either for 10,000 steps or until convergence, whichever came last. I defined convergence according to the scale-reduction factor (Gelman & Rubin 1992), a diagnostic that compares variance for individual walkers against variance of the whole ensemble. A simulation was considered converged when the scale reduction factor was less than 1.1 for each parameter in our parameter space.

Additionally, for each simulation I checked after the minimum number of steps (10,000) and at the end of the simulation whether there were any walkers in our ensemble which could be easily categorized as “bad”, i.e. trapped in a minimum of parameter space with a poorer best fit than the minimum of the ensemble majority. In detail, I classified a walker as “bad” if both of the following applied:

1. The Kolmogorov-Smirnov statistic between the best walker and the walker in question

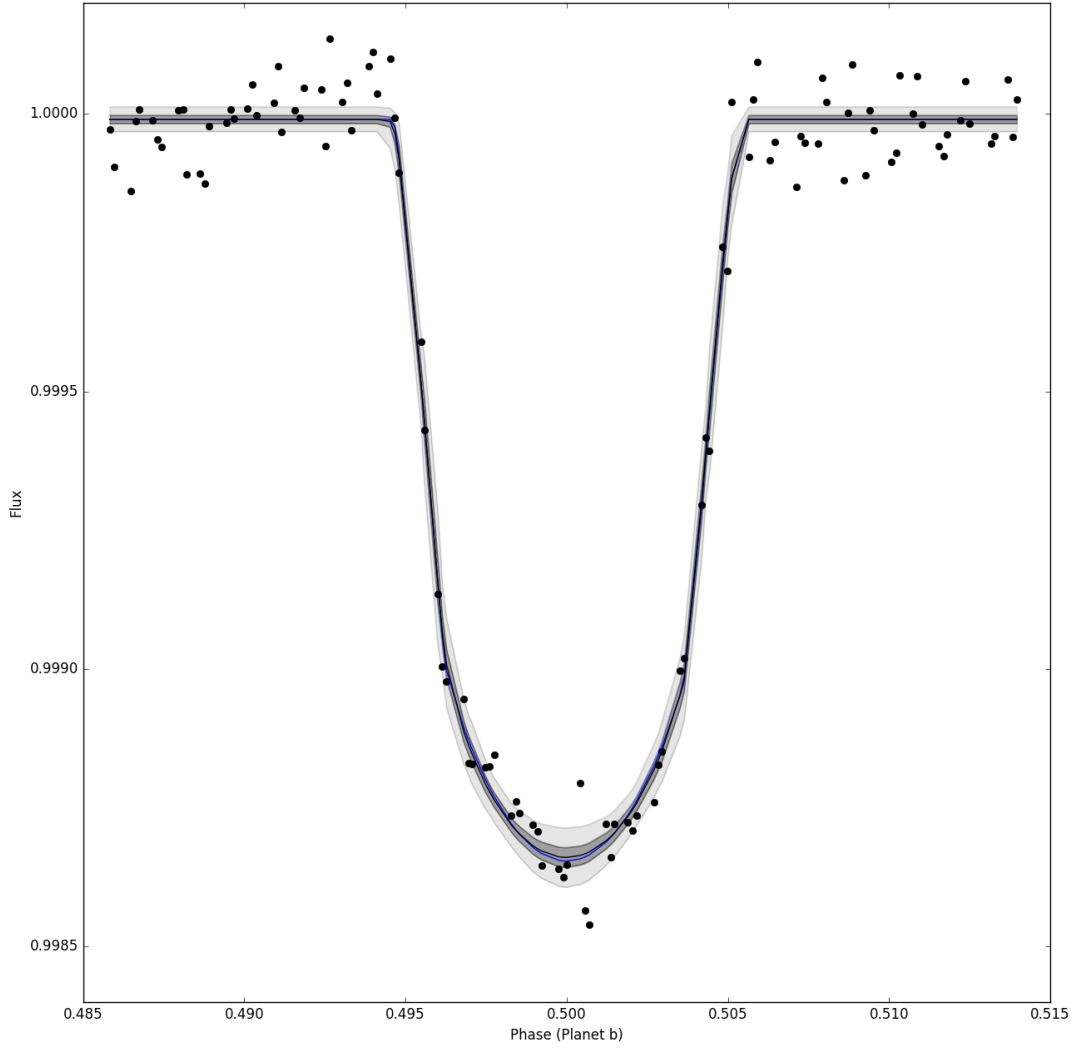


Fig. 14.—: A fit of our transit model to corrected and normalized light curve data for EPIC 212521166.01. The blue line is our transit model with the best-fit parameters, whereas the black line is the same transit model with median parameter values determined from an MCMC process. The dark grey and light grey regions are 1σ and 3σ confidence intervals, respectively.

was greater than 0.5.

2. $\exp(\theta_1 - \theta_g) < 1/(100n)$, where θ_1 is the local maximum likelihood (the maximum likelihood within the walker in question), θ_g is the global maximum likelihood throughout the ensemble, and n is the total number of steps. Failing this test meant the walker in question was very unlikely to rejoin the ensemble in the lifetime of the simulation.

If a walker was deemed bad after 10,000 steps, it was replaced with a good walker from the previous step of the simulation. If a walker was deemed bad at the end of the simulation, it was simply removed and not replaced.

For many systems, especially those with multiple candidate planets and/or long transits, the time frame within which a converged transit photometry solution could be found was longer than the time available for this research. As such, validation analysis of those candidates may be reported in future research but is not reported here.

4.2. Determining Stellar Parameters

4.2.1. Quick look classifications

As mentioned in section 3.1, each of the systems we selected for validation had a stellar spectrum that had been collected by TRES, one of the spectrographs on the 1.5-m Tillinghast telescope at the Whipple Observatory. Dave Latham and Allyson Bieryla visually inspected each spectrum collected by TRES and its cross correlation function in order to determine if there were any discrepant spectra (e.g. composite spectra or spectra of fast rotators).

I also removed cosmic rays from the spectra used for deriving stellar parameters. In

particular, I removed cosmic rays from aperture numbers 22, 23, and 24 of each spectrum. I focused on these three orders in particular because these are the only three TRES orders completely within 5050 to 5360 Angstroms. (As seen in the next section, this is the wavelength range on which the tool I used to derive stellar parameters operates.)

4.2.2. *Stellar Parameter Classification (SPC)*

After visual inspection and cosmic ray removal, each spectrum collected by TRES was analyzed using the Stellar Parameter Classification (SPC) tool, developed by Buchhave et al. (2012). SPC determines key stellar parameters through a comparison of the input spectrum to a library grid of synthetic model spectra, developed by Kurucz (1992). The library is 4-dimensional, varying in effective temperature T_{eff} , surface gravity $\log g$, metallicity $[m/H]$, and line broadening (a good proxy for projected rotational velocity, or $v \sin i$). $[m/H]$ is estimated rather than $[Fe/H]$ because all metallic absorption features are used to determine metallicity rather than just iron lines. (SPC assumes all relative metal abundances are the same as in the sun, and $[m/H]$ simply scales all solar abundances by the same factor.) This library grid spans T_{eff} from 3500 K to 9750 K in 250 K increments, $\log g$ from 0.0 to 5.0 (cgs) in 0.5 increments, $[m/H]$ from -2.5 to +0.5 in 0.5 dex increments, and line broadening from 1 km s⁻¹ to 20 km s⁻¹ in progressively spaced increments. In total, the library contains 51,359 synthetic spectra.

SPC takes an input spectrum and, for a particular value of $v \sin i$, cross-correlates it with each synthetic spectrum in the library grid from 5050 to 5360 Angstroms. The peak of the resulting, normalized cross-correlation function (CCF) for each grid point is calculated. Then, a 3-dimensional, third order polynomial in T_{eff} , $\log g$, and $[m/H]$ is fit and the peak value of the function is numerically determined. This process is then repeated for every other value of $v \sin i$ in the library grid. The locations and amplitudes of the resulting peak

CCF values (one for each $v \sin i$ value) are then modeled with a polynomial as a function of T_{eff} , $\log g$, $[m/H]$, and $v \sin i$, and the coordinates of the peak value of that polynomial are the estimated values of the parameters.

Because SPC operates on three, overlapping orders of a TRES spectrum, the above process is repeated for each order. The final parameters are determined through a weighted mean of the parameters estimated by each order. Weights are calculated according to the heights of the normalized CCF peaks for each order, so as to give preference to orders that provide a better fit to the synthetic spectra. Error bars for each of the parameters are estimated empirically as a function of normalized CCF peak heights from the analysis of a set of spectra, so that the S/N of the input spectrum can be accounted for. If the CCF peak height is above a certain threshold value, systematic errors are assumed to dominate over errors due to low S/N of the input spectrum (for more details, see Buchhave et al. 2012).

4.3. Contrast Curves

Our validation work made use of contrast curves when available (specifically, when contrast curves had been produced for a candidate system by the DSSI team). A contrast curve specifies at a given distance from the target star how bright a companion star would have to be in order to be detected. These contrast curves were primarily developed from speckle imaging (see section 3.2). Once speckle observations yielded a high-contrast image of a candidate, local minima and maxima were analyzed relative to the star’s peak brightness to determine Δm (average sensitivity) and its uncertainties within bins of radial distance from the target star. The contrast curves used in this research were the 5σ upper limit on Δm as a function of radial distance. An example of a contrast curve can be seen in Fig. 15.

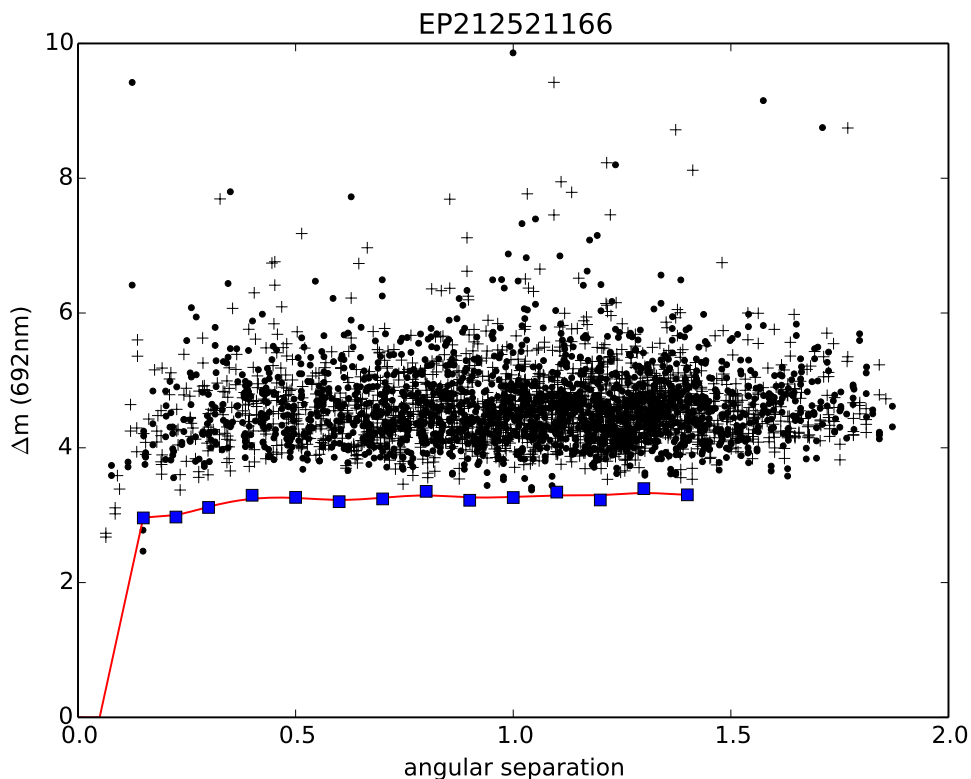


Fig. 15.—: A contrast curve developed from a speckle image at 692 nm for candidate system EPIC 212521166. The contrast curve is plotted as Δm versus angular separation (in arcseconds). Plus signs and circles are maxima and minima respectively of the background sensitivity in the image. The blue squares are the 5σ sensitivity limit within adjacent angular separation annuli. The red line is the contrast curve itself, a spline fit to the sensitivity limit (the blue squares).

Note that this process of creating a contrast curve was the same regardless of wavelength. So in the instances that multiple speckle images at different wavelengths were available, multiple contrast curves were created which were used in the validation process for a given candidate.

5. False Positive Probability Analysis

5.1. The Application of VESPA to Planet Candidates

Once photometry, spectroscopy, and any available high-contrast imaging had been collected and reduced for a candidate system, that system underwent the validation procedure using VESPA (Morton 2012). For each candidate, the following information was supplied:

1. A folded light curve containing the planetary transit and roughly one transit duration of baseline on either side. Identical error bars were assigned to all data points based on the noise parameter determined by my transit fitting procedure. This light curve had the presence of other planets in the system removed using the parameters determined by my fitting procedure.
2. A contrast curve, in order to reduce the parameter space in which a false positive scenario can exist by eliminating the possibility of stars above a certain brightness at a given distance.
3. RA and Dec. VESPA calculates the likelihood of a false positive scenario based on the target star’s location on the celestial sphere. E.g. near the Galactic plane, a target star’s FPP will increase significantly due to the crowded field.
4. T_{eff} , $\log g$, and $[m/H]$ (collected from SPC). These constraints help rule out false positive scenarios that would otherwise be allowed given only stellar magnitude information.
5. Stellar magnitudes. The K2 Ecliptic Plane Input Catalog (Huber et al. 2016) was queried to find magnitude information on each target star in the Kep, B, V, u, g, r, i, z, J, H, and K wavelength bands. For all of those bands besides Kep, magnitude uncertainties were also included if available

Given all this input, the first step VESPA makes is to create a representative population for each false positive scenario (and the transiting planet scenario). For each instance within each scenario’s population, the period is fixed at the value reported by the input. Each representative population for a given scenario has 20,000 instances. Creating this population requires a number of assumptions. First, TRILEGAL (Girardi et al. 2005), or the TRI-dimensional modeL of thE GALaxy, is used to simulate a stellar population representative of the true stellar population at the sky position given by the RA and Dec. This simulation includes stellar magnitudes and each star’s physical properties. Then stellar multiplicity is estimated by splitting each star system’s mass in two with 50% probability, and then splitting one of the components again with 25% probability (both cuts select a uniformly random mass ratio between 0.1 and 1). Additionally, stellar models are used to infer a companion’s radius and magnitude in different passbands from the primary’s T_{eff} , $\log g$, $[\text{Fe}/\text{H}]$, and magnitude in different passbands. Baraffe et al. (2002) is used for $M < 0.11M_{\odot}$, the Dartmouth models (Dotter et al. 2008) are used for $0.11M_{\odot} < M < 0.15M_{\odot}$, and the Padova models (Girardi et al. 2002) are used for $M > 0.15M_{\odot}$. Lastly, some very careful a priori assumptions are made about the planetary radius distribution and occurrence rate in order to appropriately calculate the prior and likelihood for the transiting planet scenario.

Once the representative populations have been created, a prior for each scenario can be calculated. A scenario’s prior is determined by multiplying together the probability that the scenario exists within the photometric aperture, the geometric probability that the scenario leads to an eclipse, and the fraction of instances in which the eclipse is “appropriate”. Here, “appropriate” means that an instance passes all of the constraints provided as input: an instance’s eclipse takes place within the photometric aperture, the secondary eclipse (if it exists) is not deep enough to cross the detection threshold, the instance’s primary star has wavelength-dependent magnitudes within 0.1 magnitudes of those provided as input, and

the instance’s primary star has T_{eff} and $\log g$ that agree with the inputted values to within 3σ .

After the prior for each scenario has been determined, the likelihood for each scenario must be calculated using the folded light curve. Light curves are created for each instance in a scenario, and then a trapezoidal light curve model is fit to each instance’s light curve to develop a distribution of transit durations, depths, and ingress/egress slopes for a particular scenario. Then, the same trapezoidal model is fit to the folded light curve supplied as input using either `emcee` (an MCMC process; Foreman-Mackey et al. 2013) or `MultiNest` (a multimodal nested sampling algorithm; Feroz et al. 2009, Feroz et al. 2013), depending on the user’s preferences (in our case, `MultiNest` was used). The resulting 3-dimensional distribution is multiplied with the 3-dimensional distribution developed from the scenario’s instances. Integrating over duration, depth, and ingress/egress slope for the resulting distribution yields the overall likelihood.

Once priors and likelihoods have been determined for each scenario, the last step is simply to combine them for each scenario to determine an overall posterior likelihood for every scenario. If the posterior likelihood for the planet scenario is exceedingly larger than all of the other scenarios combined, then the candidate can be classified as a planet.

The output includes simulation information from the underlying light curve fitting process, as well as figures and text files conveying likelihood information of various false positive scenarios and the transiting planet scenario. The next section provides a concrete validation example with characteristic input and output.

6. Results

The results section is divided into two parts. In the first part, the process of validation is described in detail for a single planet candidate, in order to explain precisely how the photometry and follow-up observations are used. In the second part, our validation process is more widely applied to every selected candidate and the results for each candidate are reported.

6.1. Validating a single planet: EPIC 212521166.01

In order to understand the process that was applied to each of our candidates, it is instructive to look at validation for a single, concrete example. Here, we describe in detail the validation process for a typical planet candidate system, EPIC 212521166. We chose this system because 1) it was detected in our pipeline, and 2) Osborn et al. (2016) has already confirmed and characterized the planet, which allows us to compare some of the system parameters we calculated against their results.

Osborn et al. (2016) found EPIC 212521166 to be an old, metal-poor K3 dwarf star. Both our analysis and theirs detected a planet candidate with $P = 13.9\text{d}$ and $R_p/R_* = 0.033$. A comparison of planetary and system parameters can be seen in Table 1. Both analyses are in good agreement on system and planetary parameters).

Using the orbital and transit parameters determined with our transit model, the stellar parameters derived from SPC, a folded light curve of the planetary transit, and two contrast curves in r-band and z-band collected via high-contrast speckle imaging from WIYN and DSSI, VESPA was employed to determine the false-positive probability (FPP) for EPIC 212521166.01. The FPP was found to be 1.82×10^{-9} , which was well below the cutoff threshold, so the planet candidate was classified as validated. The key output figure

Table 1: System and planetary parameters of EPIC 212521166

Parameter	Unit	This Paper	Osborn et al. (2016)
<i>Orbital parameters</i>			
Period P	days	13.86392 ± 0.00022	$13.86373 \pm 2.7 \times 10^{-4}$
Time of first transit ²	BJD-2454833	$2386.87433^{+0.00067}_{-0.00065}$	$2442.32989 \pm 6.6 \times 10^4$
Orbital eccentricity e	-	0 (fixed)	$0.051^{+0.061}_{-0.040}$
Inclination	degrees	$89.35^{+0.45}_{-0.64}$	89.28 ± 0.26
<i>Transit parameters</i>			
System scale a/R_*	-	$32.3^{+2.1}_{-4.9}$	30.73 ± 0.99
Radius ratio R_p/R_*	-	$0.0335^{+0.0014}_{-0.0008}$	$0.03346 \pm 5.9 \times 10^{-4}$
<i>Stellar parameters</i>			
Effective temperature T_{eff}	K	4877 ± 50	5010 ± 48
Surface gravity $\log g$	g cm^{-2}	4.51 ± 0.10	4.598 ± 0.032
Metallicity $[m/H]$	dex	-0.298 ± 0.08	-0.343 ± 0.032
<i>Validation parameters</i>			
FPP	-	1.82×10^{-9}	-

of VESPA can be seen in Fig. 16.

6.2. Full Validation Results

The process of validation described for EPIC 21252116.01 in the previous section was similarly applied to the remaining candidates suitable for validation. We identified 357 targets from the K2 candidate detection pipeline which had spectra from TRES. Of those, 287 passed through our vetting process and were classified as planets. Of those, we were

² Our reported transit time and that reported by Osborn et al. (2016) differ by 4 orbital periods.

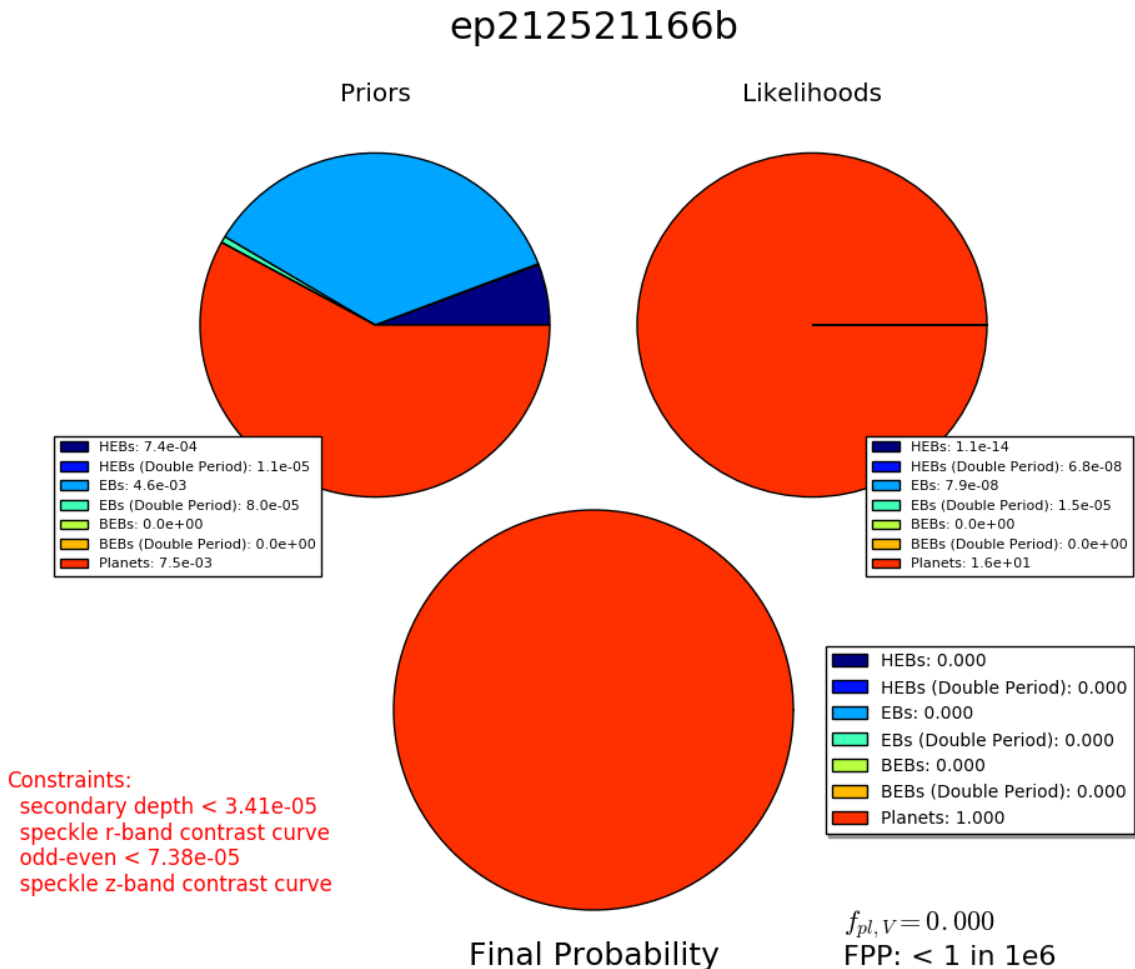


Fig. 16.—: False Positive Probability analysis of EPIC 212521166.01. Combining the prior likelihood of a false positive scenario (given sky position, contrast curve data, and wavelength-dependent magnitudes), as well as the likelihood of the transit photometry under various scenarios, the posterior distribution highly favors the planet scenario, with $FPP = 1.82 \times 10^{-9}$. (Note: the true FPP value is always reported in a supplementary file, but for $FPP < 1$ in $1e6$ the figure produced by VESPA simply reports $FPP < 1$ in $1e6$.)

able to determine transit parameters for 197 candidates. The FPP was calculated for each of these candidate (see Table 2), and candidates with $FPP < 0.001$ were promoted to validated planet status. (Also note that the stellar parameters for each system are reported in Table 3).

In addition to the parameters derived through the validation process described in previous sections, we also calculated the radii and masses of the stars in our sample using the equations from Section 8 of Torres et al. (2010). We also used these equations to propagate uncertainties into the stellar mass and radius estimates. These values are also reported in Table 2.

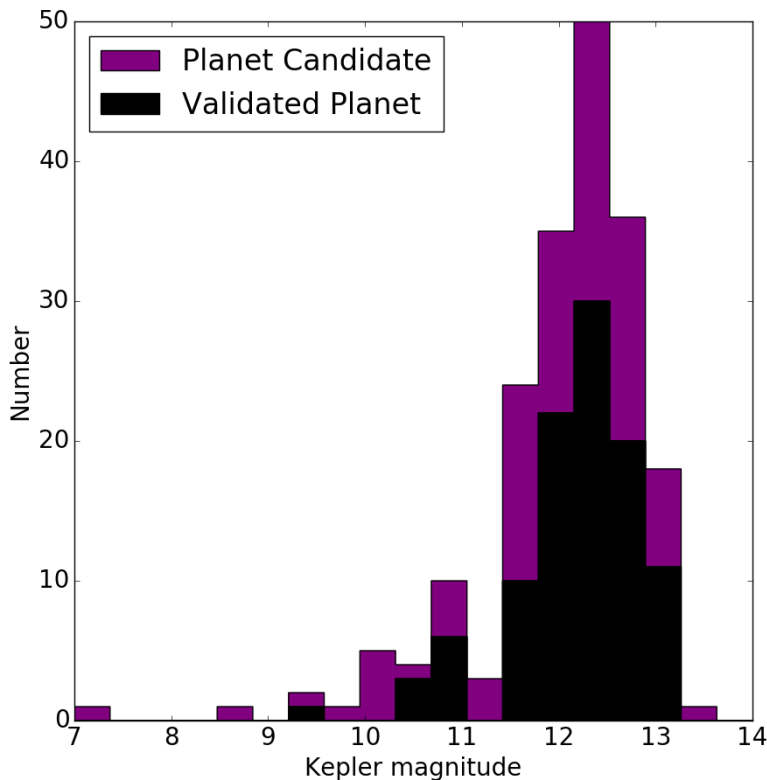


Fig. 17.—: Histogram of Kepler magnitude for the validated planets and candidates in C0-C10 of K2 that have been identified in this work. There is a clear cutoff in the distribution near magnitude 13, since validation was only conducted on stars for which we had a spectrum and almost all of the spectra we used were for targets brighter than 13th magnitude. Candidates with an "Unknown" disposition in Table 2 are not included in this histogram.

Systems with multiple planet candidates are more likely to be hosting multiple planets than multiple false positive signals. In fact, the likelihood of the planet scenario for

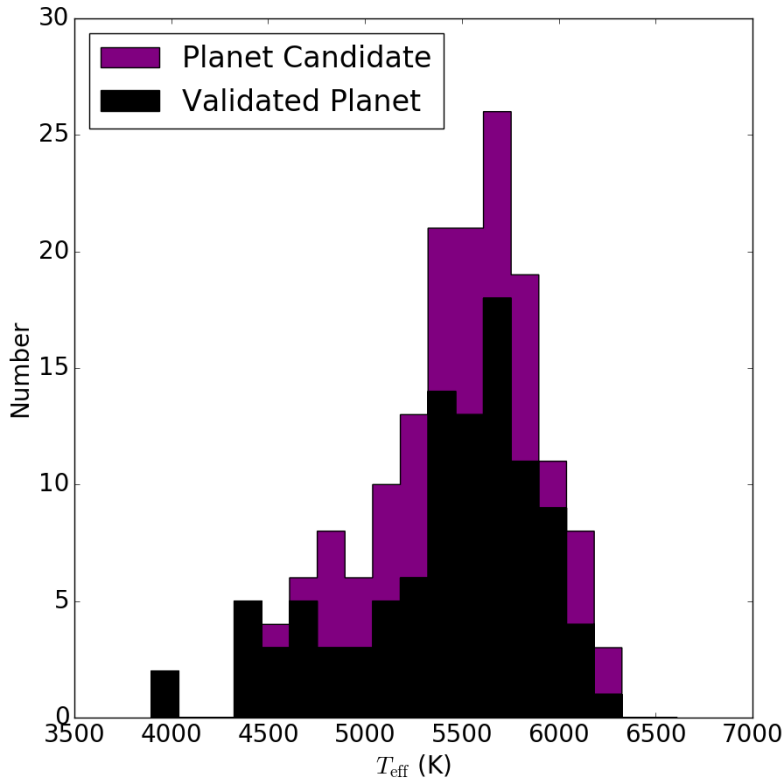


Fig. 18.—: Histogram of effective temperature for the validated planets and candidates in C0-C10 of K2 that have been identified in this work. Candidates with an “Unknown” disposition in Table 2 are not included in this histogram.

each individual candidate is consequently boosted relative to false positive scenarios in multiplanet candidate systems. To account for this effect, we apply a “multiplicity boost” to the planet scenario prior in such systems, deflating the FPP by the multiplicity boost factor to account for the nature of these systems. We choose a boost factor of 25 for double candidate systems and a boost factor of 50 for systems with 3+ candidates based on the values used by Lissauer et al. (2012), Vanderburg et al. (2016b), and Sinukoff et al. (2016). The FPP values reported in Table 2 already have the appropriate multiplicity boost factor applied.

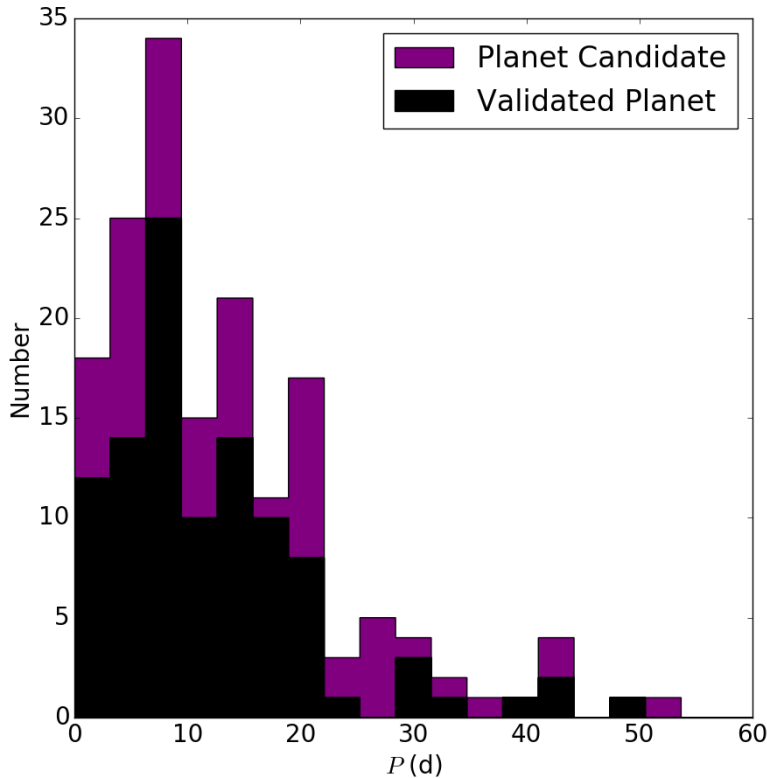


Fig. 19.—: Histogram of orbital period for the validated planets and candidates in C0-C10 of K2 that have been identified in this work. The steep drop off in validated planets and candidates around 20 days is due to the K2 strategy of observing each field for only ~ 75 days. Candidates with an “Unknown” disposition in Table 2 are not included in this histogram.

One limitation of our analysis was that it appeared in some cases that our transit solution gave an an unreasonably high value of R_p/R_* . In other words, our transit fitting process sometimes preferred a grazing transit from a brown dwarf or stellar-sized object over a low impact parameter transit from a planet-sized object. In fact, the latter scenario was preferred at a much higher rate than we expected. Further, VESPA only considers the size of a transiting object, without taking into consideration the fact that the largest planets ($\sim 2R_{Jup}$) are larger than the smallest stars ($\sim 0.8R_{Jup}$). For these reasons, we do not report FPP values on planets we estimate to be larger than $0.8R_{Jup}$ (a good size

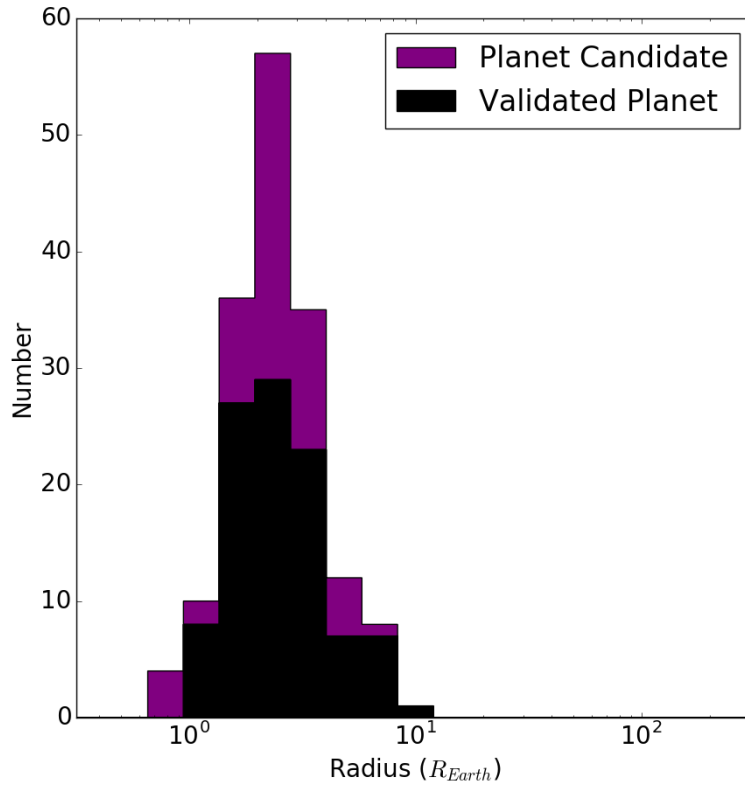


Fig. 20.—: Histogram of planetary radius for the validated planets and candidates in C0-C10 of K2 that have been identified in this work. Candidates with an "Unknown" disposition in Table 2 are not included in this histogram.

estimate for some of the smallest M dwarfs).

It is interesting to explore a few of the demographics of the newly validated exoplanet population. Figs. 17- 21 reveal various aspects of the validated exoplanet sample and the exoplanet candidate sample. However, it should be noted that those candidates with an "Unknown" disposition in Table 2 (either due to their large size or a VESPA error) are not included in any of these figures or their associated analysis (there are 34 such candidates).

Fig. 17 is a histogram of the distribution of brightnesses for host stars (stars hosting multiple planets are repeated in the histogram). Most of the candidates in our population

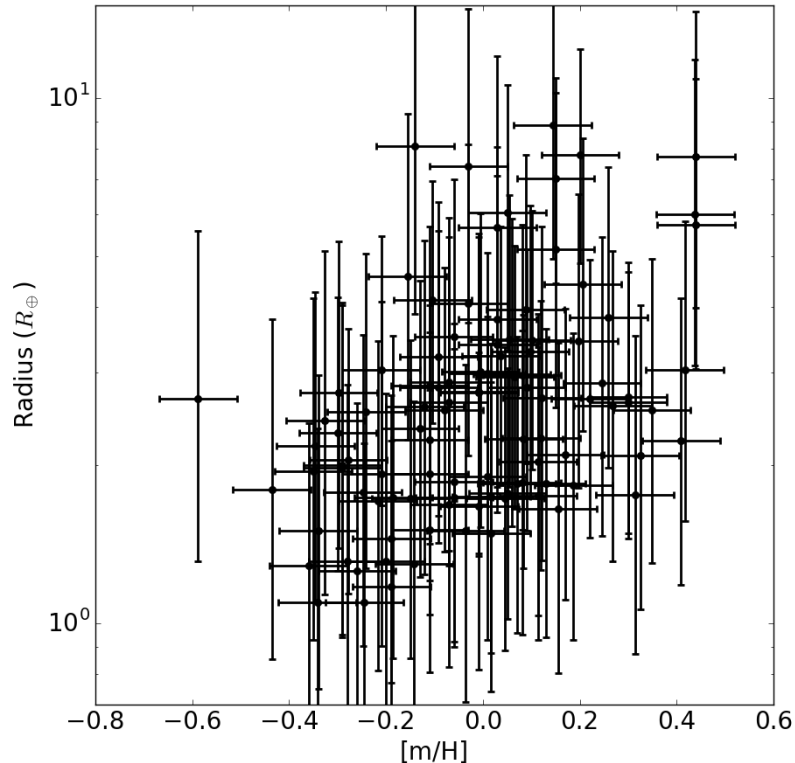


Fig. 21.—: Relationship between the planetary radius and the stellar metallicity for the validated planets from C0-C10 of K2 that have been identified in this work. Unlike the relationship seen in Buchhave et al. (2014), there appears to be a lower envelope in our sample leading to an absence of small planets orbiting metal-rich stars. This discrepancy may be a systematic effect stemming from differences between the K2 and Kepler observing strategies or targets. Candidates with an "Unknown" disposition in Table 2 are not included in this plot.

are clustered near stellar magnitudes of $K_p = 12$ to $K_p = 13$, and the cutoff we imposed at $K_p = 13$ is very evident.

Most of the candidates we identified (validated and otherwise) orbit host stars with effective temperatures in the 5000 – 6000 K range. However, there are a handful of hotter stars and a few cool M dwarfs in our sample as well (see Fig. 18).

We also explored the period distribution of our candidate population. As can be seen in Fig. 19, the typical planet candidate (validated or otherwise) has an orbital period of 20 days or less. This should come as no surprise, given the nature of the candidate identification pipeline we used (based on VJ14) and the ~ 75 day baseline of photometry per campaign field.

Fig. 20 demonstrates the planetary radius distribution of our sample. As mentioned above, we chose to exclude candidates classified with an "Unknown" disposition from our exploration of the candidate population. Thus, there's a clear cutoff in planet radius in Fig. 20 at $R_p = 0.8R_{\text{Jup}}$ (since we classified such planets as "Unknown"). Another feature of the planetary radius distribution for our sample is that the distribution peaks around $2 - 3R_{\oplus}$ (however, with linear rather than logarithmic bins, the validated planet distribution peaks nearer to $1R_{\oplus}$).

One of the more interesting relationships we encountered was between planetary radius and stellar metallicity. As has been seen in previous research, planetary radius appears to be positively correlated with stellar metallicity, so metal-rich stars tend to host large planets and metal-poor stars tend to host smaller planets. One major example of this is Buchhave et al. (2014), in which this effect is explored for the original Kepler field. However, as can be seen in Fig. 21, although we see a similar positive correlation, our sample also shows evidence of a lower envelope in the metal-rich, small-planet region (i.e. we don't see any small planets orbiting metal-rich stars). This lower envelope is not seen in Buchhave et al. (2014). We suspect that the difference between our distribution and theirs may stem from the disparate observing strategies of Kepler and K2, including the length of observations, the choice of targets, and the sensitivity to stars and planets at fainter magnitudes. However, we don't currently have a specific satisfying explanation, and further research is required.

We will refrain from drawing any conclusions about the underlying exoplanet population from any of these results given the great number of biases induced in the process of identifying candidates and subjecting them to validation (including the length of the K2 observation baseline, the process of candidate identification outlined by VJ14, the paucity of multiplanet systems due to time constraints in the transit fitting process, and the hard cut we imposed at $K_p = 13$). The planets validated in this work will be useful additions to the larger validated exoplanet population, but the underlying systematic biases leading to their validation are significant and should be carefully considered when attempting to support general claims about the exoplanet population.

7. Broader Impacts

The K2 mission has thus far conducted observations through C13 (ongoing), but it has more observations planned at least through C16 (and possibly C18 or further). Given that the validation infrastructure built for this research is directly applicable to future campaigns, we will be able to identify and validate exoplanet candidates from upcoming campaigns as quickly as the necessary follow-up observations can be collected.

This research will also be useful even after the end of the K2 mission. The upcoming Transiting Exoplanet Survey Satellite (TESS) mission (discussed in section 1.4.2 has three level one baseline science requirements, one of which is to measure the masses of 50 planets with $R < 4R_{\oplus}$. This necessitates an extensive follow-up program to the primary photometric observations conducted by the spacecraft. The work presented here will be extremely useful in that follow-up program, since only modest adjustments will allow for the validation of planet candidate systems identified by TESS rather than K2.

8. Summary and Conclusions

In this thesis, we identified 197 planet candidates from Campaigns 0-10 of the K2 mission and conduct a validation process on each of them. We removed instrumental systematics from the K2 photometry, searched the corrected light curves for candidates, and conducted a vetting process to identify promising candidates. We also analyzed follow-up observations of our candidate systems including spectroscopy and high-contrast imaging. We derived transit/orbital parameters from the K2 photometry, stellar parameters from spectra, and contrast curves from the high-contrast imaging. Then, using these results, we determined the false positive probability (FPP) of each planet candidate using a procedure called VESPA (Morton 2012), which estimates the posterior probability of planethood and various false positive scenarios through a target’s sky position, its likelihood of hosting a stellar companion, and the plausibility of various scenarios given the shape of the candidate transits. We reported the resulting FPPs for our planet candidates (in Table 2) and classified all candidates with $FPP < 0.001$) as validated planets.

102 of the 197 candidates had a $FPP < 0.001$, while 61 remained candidates ($0.001 < FPP$) and 34 are classified as "Unknown" (we either could not or chose not to report the FPP in these cases). Of the 102 newly validated exoplanets, 33 are brand new (i.e. have not even been classified as candidates before), while 37 have already been identified as candidates before and 32 have already been validated. Most of the newly validated exoplanets orbited host stars with $12 < K_p < 13$ and $5000 \text{ K} < T_{\text{eff}} < 6000 \text{ K}$. Additionally, the majority of validated planets had orbital periods $< 20 \text{ d}$ and planetary radii between $1 - 4R_{\oplus}$.

This work has clear broader implications. The ability to validate planet candidates is vital to conducting a successful follow-up and confirmation program. The wide applicability of the validation infrastructure developed in this research is clear from the large number

of candidates subjected to our validation process. By continuing to apply the validation process described here, future K2 campaigns and the upcoming TESS mission will benefit from a valuable source of validated planets and a useful validation pipeline able to process the large and constant supply of discovered planet candidates.

The author would like to thank Andrew Vanderburg and Dr. David Latham for their invaluable guidance throughout this project. The author would also like to thank the external readers Dr. Guillermo Torres and Dr. Dimitar Sasselov for their review and grading of this work. Further, the author is grateful for the collection of TRES spectra by Dr. Gil Esquerdo, Dr. Mike Calkins, and Dr. Perry Berlind, as well as the collection and analysis of speckle observations by Dr. Steve Howell, Dr. Elliott Horch, Dr. Mark Everett, and Dr. Dave Ciradi. Additionally, correspondences with Dr. Ian Crossfield, Dr. Tom Barclay, and Dr. Tim Morton were very helpful; Dr. Morton in particular provided extremely useful advice into the inner workings of VESPA. Finally, the author wishes to thank Prof. David Charbonneau and the classmates of Astronomy 99 for their regular support and feedback.

Table 2: Planet Candidate Parameters

EPIC	T_0 (BJD-2454833)	P (d)	i (deg)	R_p/R_*	a/R_*	R_p (R_\oplus)	R_* (R_\odot)	M_* (M_\odot)	FPP	Disposition
201384232.01	1994.4973 ± 0.0044	30.9444 ± 0.0031	$89.34^{+0.47}_{-0.85}$	$0.0247^{+0.0017}_{-0.0010}$	41^{+5}_{-11}	$2.6^{+2.8}_{-1.3}$	$1.0^{+1.0}_{-0.5}$	$0.75^{+0.48}_{-0.30}$	$1.04e - 04$	Planet
201441872.01	$1979.8714^{+0.0065}_{-0.0071}$	$4.44120^{+0.00092}_{-0.00096}$	$87.7^{+1.6}_{-3.5}$	$0.0121^{+0.0017}_{-0.0011}$	$12.1^{+2.8}_{-3.9}$	$1.2^{+1.1}_{-0.6}$	$0.92^{+0.85}_{-0.45}$	$0.85^{+0.51}_{-0.33}$	-	Unknown ³
201505350.01	1980.38333 ± 0.00026	7.919492 ± 0.000049	$89.36^{+0.45}_{-0.73}$	$0.0742^{+0.0018}_{-0.0010}$	$19.5^{+0.5}_{-1.3}$	$7.4^{+7.3}_{-3.7}$	$0.92^{+0.91}_{-0.45}$	$0.79^{+0.49}_{-0.31}$	$7.04e - 07$	Planet
201505350.02	$1984.27512^{+0.00082}_{-0.00081}$	11.90764 ± 0.00024	$89.01^{+0.71}_{-0.87}$	$0.0446^{+0.0017}_{-0.0008}$	$23.3^{+2.0}_{-3.7}$	$4.5^{+4.5}_{-2.3}$	$0.92^{+0.93}_{-0.46}$	$0.80^{+0.50}_{-0.31}$	$2.00e - 02$	Candidate
201505350.03	$1978.4311^{+0.0058}_{-0.0063}$	$2.50827^{+0.00030}_{-0.00029}$	$86.4^{+2.6}_{-5.1}$	$0.0128^{+0.0012}_{-0.0008}$	$7.6^{+1.3}_{-2.3}$	$1.3^{+1.3}_{-0.7}$	$0.92^{+0.93}_{-0.47}$	$0.80^{+0.49}_{-0.31}$	-	Unknown ³
201546283.01	$1979.84473^{+0.00039}_{-0.00040}$	$6.771386^{+0.000059}_{-0.000060}$	$88.8^{+0.8}_{-1.0}$	$0.0492^{+0.0016}_{-0.0009}$	$18.1^{+1.2}_{-2.5}$	$5.2^{+5.1}_{-2.6}$	$0.96^{+0.95}_{-0.48}$	$0.83^{+0.52}_{-0.32}$	$8.72e - 07$	Planet
201577035.01	1986.5776 ± 0.0011	$19.30702^{+0.00059}_{-0.00060}$	$89.47^{+0.37}_{-0.53}$	$0.0380^{+0.0011}_{-0.0008}$	$38.3^{+2.4}_{-5.6}$	$4.1^{+4.1}_{-2.0}$	$0.98^{+0.99}_{-0.48}$	$0.90^{+0.53}_{-0.35}$	$8.69e - 05$	Planet
201613023.01	$1982.3700^{+0.0027}_{-0.0026}$	$8.28247^{+0.00047}_{-0.00050}$	$87.9^{+1.6}_{-3.5}$	$0.0198^{+0.0017}_{-0.0008}$	$13.5^{+1.9}_{-4.9}$	$2.2^{+1.8}_{-1.0}$	$1.03^{+0.83}_{-0.47}$	$1.19^{+0.62}_{-0.41}$	$1.07e - 04$	Planet
201828749.01	$1980.1541^{+0.0033}_{-0.0032}$	$33.5140^{+0.0027}_{-0.0029}$	$89.33^{+0.48}_{-0.98}$	$0.0263^{+0.0030}_{-0.0014}$	47^{+8}_{-17}	$2.7^{+2.7}_{-1.3}$	$0.94^{+0.95}_{-0.46}$	$0.84^{+0.53}_{-0.32}$	$6.83e - 03$	Candidate
201855371.01	$1984.9435^{+0.0032}_{-0.0034}$	17.9692 ± 0.0014	$89.37^{+0.45}_{-0.86}$	$0.0299^{+0.0034}_{-0.0020}$	46^{+8}_{-15}	$2.0^{+2.2}_{-1.0}$	$0.60^{+0.67}_{-0.31}$	$0.57^{+0.38}_{-0.23}$	$1.15e - 06$	Planet
201920032.01	$2000.2016^{+0.0048}_{-0.0054}$	$28.2714^{+0.0038}_{-0.0035}$	$89.3^{+0.5}_{-1.1}$	$0.0268^{+0.0042}_{-0.0019}$	43^{+8}_{-16}	$3.0^{+2.7}_{-1.4}$	$1.03^{+0.91}_{-0.48}$	$1.04^{+0.57}_{-0.39}$	$1.03e - 02$	Candidate
202091388.01	$1940.3830^{+0.0026}_{-0.0025}$	$6.4798^{+0.0013}_{-0.0012}$	$88.2^{+1.3}_{-2.5}$	$0.0332^{+0.0027}_{-0.0019}$	$15.5^{+2.5}_{-4.8}$	$3.7^{+3.5}_{-1.8}$	$1.03^{+0.97}_{-0.50}$	$0.94^{+0.55}_{-0.36}$	$4.68e - 03$	Candidate
202675839.01	$2065.8483^{+0.0035}_{-0.0036}$	15.4667 ± 0.0015	$83.8^{+1.8}_{-1.5}$	$0.42^{+0.39}_{-0.31}$	$13.0^{+1.9}_{-1.3}$	57^{+69}_{-50}	$1.26^{+0.98}_{-0.56}$	$1.37^{+0.72}_{-0.47}$	-	Unknown ⁴
203771098.01	$2082.62488^{+0.00056}_{-0.00055}$	$42.36395^{+0.00074}_{-0.00076}$	$89.58^{+0.29}_{-0.25}$	$0.0610^{+0.0017}_{-0.0010}$	$50.0^{+3.1}_{-4.5}$	$7.7^{+6.9}_{-3.7}$	$1.2^{+1.0}_{-0.6}$	$1.12^{+0.63}_{-0.41}$	$1.04e - 06$	Planet
203771098.02	2072.79597 ± 0.00085	$20.88502^{+0.00041}_{-0.00040}$	$88.86^{+0.65}_{-0.64}$	$0.0451^{+0.0022}_{-0.0016}$	$26.4^{+3.5}_{-4.0}$	$5.7^{+5.2}_{-2.7}$	$1.2^{+1.0}_{-0.5}$	$1.10^{+0.61}_{-0.40}$	$2.68e - 05$	Planet
203826436.01	$2065.8560^{+0.0021}_{-0.0020}$	$6.42955^{+0.00031}_{-0.00030}$	$88.1^{+1.4}_{-2.6}$	$0.0293^{+0.0034}_{-0.0015}$	$15.2^{+2.1}_{-4.9}$	$2.9^{+3.0}_{-1.5}$	$0.90^{+0.95}_{-0.47}$	$0.73^{+0.46}_{-0.29}$	$1.39e - 15$	Planet
203826436.02	$2074.2361^{+0.0027}_{-0.0025}$	$14.0910^{+0.0010}_{-0.0011}$	$89.2^{+0.6}_{-1.0}$	$0.0270^{+0.0029}_{-0.0014}$	35^{+5}_{-10}	$2.6^{+2.8}_{-1.3}$	$0.89^{+0.95}_{-0.46}$	$0.73^{+0.48}_{-0.29}$	$1.66e - 09$	Planet
203826436.03	$2065.1129^{+0.0045}_{-0.0043}$	$4.44374^{+0.00045}_{-0.00047}$	$87.7^{+1.7}_{-3.4}$	$0.0171^{+0.0019}_{-0.0010}$	$11.0^{+1.4}_{-3.2}$	$1.7^{+1.8}_{-0.9}$	$0.90^{+0.98}_{-0.46}$	$0.73^{+0.49}_{-0.29}$	$1.17e - 10$	Planet
204750116.01	$2065.8360^{+0.0040}_{-0.0038}$	$23.4469^{+0.0019}_{-0.0020}$	$88.9^{+0.8}_{-1.3}$	$0.0271^{+0.0028}_{-0.0014}$	$27.0^{+4.4}_{-8.0}$	$3.2^{+3.0}_{-1.6}$	$1.1^{+1.0}_{-0.5}$	$0.93^{+0.55}_{-0.35}$	$2.20e - 03$	Candidate

³ The VESPA package (Morton 2012) failed to find a FPP

⁴ Our transit fitting process sometimes finds unreasonably large planet radii. Further, unless there is a deep secondary eclipse or ellipsoidal variations in the light curve, a planet-sized star cannot be distinguished from a planet without radial velocity measurements. Thus, FPP values are not reported for candidates with $R_p > 0.8R_{\text{Jup}}$.

Table 2: Continued

EPIC	T_0 (BJD-2454833)	P (d)	i (deg)	R_p/R_*	a/R_*	R_p (R_{\oplus})	R_* (R_{\odot})	M_* (M_{\odot})	FPP	Disposition
204890128.01	2063.3847 $^{+0.0024}_{-0.0023}$	12.20771 \pm 0.00060	88.8 $^{+0.9}_{-1.5}$	0.0291 $^{+0.0024}_{-0.0013}$	23.1 $^{+3.2}_{-6.5}$	2.8 $^{+2.9}_{-1.4}$	0.89 $^{+0.90}_{-0.44}$	0.84 $^{+0.49}_{-0.33}$	4.33e - 15	Planet
205029914.01	2061.7313 $^{+0.0014}_{-0.0015}$	4.98185 \pm 0.00017	86.8 $^{+2.2}_{-3.7}$	0.0223 $^{+0.0016}_{-0.0008}$	8.8 $^{+1.1}_{-2.3}$	2.5 $^{+2.2}_{-1.2}$	1.05 $^{+0.91}_{-0.48}$	1.11 $^{+0.62}_{-0.40}$	6.73e - 11	Planet
205071984.01	2067.92670 $^{+0.00063}_{-0.00064}$	8.99195 \pm 0.00016	89.10 $^{+0.64}_{-0.84}$	0.0566 $^{+0.0012}_{-0.0010}$	20.2 $^{+1.0}_{-2.3}$	5.7 $^{+6.3}_{-2.9}$	0.9 $^{+1.0}_{-0.5}$	0.70 $^{+0.47}_{-0.29}$	0.00e + 00	Planet
205071984.02	2070.7928 \pm 0.0025	31.7152 $^{+0.0025}_{-0.0022}$	89.28 $^{+0.52}_{-0.99}$	0.0375 $^{+0.0028}_{-0.0013}$	44 $^{+8}_{-15}$	3.8 $^{+4.3}_{-2.0}$	0.9 $^{+1.0}_{-0.5}$	0.70 $^{+0.47}_{-0.28}$	1.11e - 14	Planet
205071984.03	2066.4220 $^{+0.0037}_{-0.0040}$	20.6617 $^{+0.0018}_{-0.0017}$	89.31 $^{+0.49}_{-0.86}$	0.0340 $^{+0.0016}_{-0.0010}$	33.9 $^{+2.9}_{-7.6}$	3.4 $^{+3.7}_{-1.8}$	0.9 $^{+1.0}_{-0.5}$	0.69 $^{+0.46}_{-0.28}$	1.41e - 13	Planet
205950854.01	2157.8875 $^{+0.0026}_{-0.0025}$	15.8541 $^{+0.0014}_{-0.0013}$	89.0 $^{+0.7}_{-1.3}$	0.0224 $^{+0.0012}_{-0.0010}$	28.5 $^{+3.7}_{-8.5}$	2.3 $^{+2.1}_{-1.1}$	0.96 $^{+0.87}_{-0.46}$	0.94 $^{+0.54}_{-0.35}$	1.73e - 04	Planet
205957328.01	2148.5855 $^{+0.0033}_{-0.0031}$	14.3535 $^{+0.0014}_{-0.0015}$	89.0 $^{+0.7}_{-1.7}$	0.0240 $^{+0.0037}_{-0.0017}$	31 $^{+6}_{-12}$	2.4 $^{+2.4}_{-1.2}$	0.91 $^{+0.90}_{-0.47}$	0.80 $^{+0.49}_{-0.31}$	3.61e - 03	Candidate
206008091.01	2152.6673 $^{+0.0043}_{-0.0045}$	12.4000 $^{+0.0018}_{-0.0017}$	88.7 $^{+1.0}_{-2.0}$	0.0169 $^{+0.0011}_{-0.0008}$	21.0 $^{+2.9}_{-6.8}$	1.9 $^{+1.7}_{-0.9}$	1.05 $^{+0.90}_{-0.48}$	1.14 $^{+0.61}_{-0.40}$	4.96e - 06	Planet
206008091.02	2153.1849 $^{+0.0070}_{-0.0069}$	7.5766 \pm 0.0017	88.0 $^{+1.5}_{-2.7}$	0.01334 $^{+0.00091}_{-0.00082}$	14.3 $^{+2.3}_{-4.5}$	1.5 $^{+1.3}_{-0.7}$	1.03 $^{+0.87}_{-0.48}$	1.15 $^{+0.61}_{-0.41}$	5.56e - 05	Planet
206011496.01	2148.64575 $^{+0.00093}_{-0.00094}$	2.369008 $^{+0.000056}_{-0.000058}$	86.4 $^{+2.6}_{-4.2}$	0.0172 $^{+0.0010}_{-0.0006}$	7.2 $^{+0.8}_{-1.7}$	1.8 $^{+1.7}_{-0.9}$	0.99 $^{+0.89}_{-0.47}$	0.94 $^{+0.55}_{-0.35}$	2.38e - 09	Planet
206044803.01	2147.6403 \pm 0.0024	2.57340 $^{+0.00017}_{-0.00016}$	85.7 $^{+3.0}_{-5.2}$	0.0175 $^{+0.0018}_{-0.0009}$	6.5 $^{+0.9}_{-1.8}$	2.1 $^{+1.9}_{-1.0}$	1.10 $^{+0.98}_{-0.51}$	1.12 $^{+0.61}_{-0.40}$	1.48e - 04	Planet
206082454.01	2160.5399 $^{+0.0013}_{-0.0012}$	29.6267 $^{+0.0017}_{-0.0016}$	89.47 $^{+0.36}_{-0.55}$	0.0339 $^{+0.0014}_{-0.0009}$	43.9 $^{+3.7}_{-8.1}$	3.5 $^{+3.5}_{-1.8}$	0.95 $^{+0.94}_{-0.49}$	0.81 $^{+0.51}_{-0.31}$	1.13e - 06	Planet
206082454.02	2149.2946 \pm 0.0037	14.3171 \pm 0.0015	88.9 $^{+0.8}_{-1.5}$	0.0176 $^{+0.0013}_{-0.0008}$	24.9 $^{+3.4}_{-7.4}$	1.9 $^{+1.9}_{-0.9}$	0.97 $^{+0.96}_{-0.49}$	0.80 $^{+0.52}_{-0.31}$	5.00e - 05	Planet
206096602.01	2149.6856 \pm 0.0010	6.67177 \pm 0.00018	89.1 $^{+0.6}_{-1.2}$	0.0273 $^{+0.0017}_{-0.0011}$	29.9 $^{+3.7}_{-8.6}$	2.0 $^{+2.1}_{-1.1}$	0.67 $^{+0.70}_{-0.35}$	0.61 $^{+0.40}_{-0.25}$	7.98e - 08	Planet
206096602.02	2158.5450 $^{+0.0016}_{-0.0017}$	16.19708 $^{+0.00086}_{-0.00082}$	89.66 $^{+0.24}_{-0.49}$	0.0266 $^{+0.0018}_{-0.0012}$	80 $^{+11}_{-24}$	2.0 $^{+2.1}_{-1.0}$	0.68 $^{+0.71}_{-0.36}$	0.61 $^{+0.40}_{-0.24}$	4.84e - 05	Planet
206114630.01	2152.3896 \pm 0.0014	7.44503 $^{+0.00028}_{-0.00031}$	89.55 $^{+0.32}_{-0.68}$	0.0245 $^{+0.0031}_{-0.0021}$	63 $^{+14}_{-21}$	2.4 $^{+2.5}_{-1.3}$	0.91 $^{+0.93}_{-0.46}$	0.75 $^{+0.49}_{-0.30}$	6.24e - 01	Candidate
206119924.01	2146.9502 $^{+0.0041}_{-0.0043}$	4.65532 $^{+0.00051}_{-0.00052}$	88.0 $^{+1.5}_{-3.1}$	0.00956 $^{+0.00097}_{-0.00072}$	14.2 $^{+2.7}_{-4.9}$	0.72 $^{+0.75}_{-0.36}$	0.69 $^{+0.71}_{-0.35}$	0.65 $^{+0.42}_{-0.26}$	2.86e - 02	Candidate
206144956.01	2153.3277 \pm 0.0015	12.64782 $^{+0.00067}_{-0.00068}$	89.1 $^{+0.6}_{-1.1}$	0.0190 $^{+0.0027}_{-0.0011}$	28.7 $^{+3.1}_{-7.0}$	1.5 $^{+1.5}_{-0.8}$	0.73 $^{+0.70}_{-0.36}$	0.74 $^{+0.45}_{-0.28}$	4.75e - 05	Planet
206146957.01	2146.8701 \pm 0.0034	5.76134 \pm 0.00053	88.1 $^{+1.4}_{-3.2}$	0.0141 $^{+0.0016}_{-0.0009}$	16.3 $^{+3.1}_{-6.6}$	1.5 $^{+1.5}_{-0.8}$	0.99 $^{+0.96}_{-0.50}$	0.86 $^{+0.52}_{-0.33}$	3.04e - 03	Candidate
206159027.01	2149.3258 $^{+0.0019}_{-0.0018}$	8.05481 $^{+0.00042}_{-0.00041}$	88.6 $^{+1.0}_{-1.6}$	0.0240 $^{+0.0022}_{-0.0012}$	19.6 $^{+2.5}_{-5.2}$	1.9 $^{+2.2}_{-1.0}$	0.74 $^{+0.83}_{-0.39}$	0.62 $^{+0.41}_{-0.26}$	7.50e - 08	Planet
206181769.01	2151.4441 \pm 0.0011	13.97850 $^{+0.00059}_{-0.00055}$	89.2 $^{+0.6}_{-1.1}$	0.03161 $^{+0.00082}_{-0.00074}$	29.7 $^{+2.9}_{-7.4}$	3.0 $^{+2.9}_{-1.5}$	0.86 $^{+0.84}_{-0.42}$	0.83 $^{+0.49}_{-0.32}$	6.35e - 10	Planet
206192335.01	2146.9470 \pm 0.0020	3.59906 \pm 0.00019	88.0 $^{+1.5}_{-3.0}$	0.0176 $^{+0.0014}_{-0.0010}$	13.5 $^{+2.1}_{-4.2}$	1.7 $^{+1.7}_{-0.9}$	0.90 $^{+0.89}_{-0.45}$	0.80 $^{+0.49}_{-0.31}$	6.01e - 05	Planet
206245553.01	2147.1765 $^{+0.0014}_{-0.0013}$	7.49572 $^{+0.00028}_{-0.00029}$	88.4 $^{+1.1}_{-1.8}$	0.0229 $^{+0.0013}_{-0.0006}$	15.1 $^{+1.3}_{-3.2}$	2.8 $^{+2.3}_{-1.3}$	1.13 $^{+0.93}_{-0.52}$	1.17 $^{+0.65}_{-0.42}$	5.28e - 06	Planet
206268299.01	2164.9996 $^{+0.0024}_{-0.0028}$	19.5657 $^{+0.0020}_{-0.0018}$	88.9 $^{+0.8}_{-1.1}$	0.0250 $^{+0.0019}_{-0.0011}$	26.2 $^{+3.4}_{-6.5}$	3.0 $^{+2.4}_{-1.4}$	1.11 $^{+0.88}_{-0.49}$	1.32 $^{+0.69}_{-0.46}$	3.39e - 05	Planet

Table 2: Continued

EPIC	T_0 (BJD-2454833)	P (d)	i (deg)	R_p/R_*	a/R_*	R_p (R_\oplus)	R_* (R_\odot)	M_* (M_\odot)	FPP	Disposition
206348688.01	2150.4292 ± 0.0039	$7.81795^{+0.00076}_{-0.00079}$	$87.3^{+1.9}_{-4.3}$	$0.0189^{+0.0011}_{-0.0007}$	$10.4^{+1.4}_{-3.6}$	$2.6^{+2.0}_{-1.2}$	$1.28^{+0.99}_{-0.57}$	$1.36^{+0.68}_{-0.46}$	$4.68e - 07$	Planet
206348688.02	$2159.7477^{+0.0065}_{-0.0090}$	$18.2859^{+0.0054}_{-0.0044}$	$88.7^{+0.9}_{-2.1}$	$0.0195^{+0.0012}_{-0.0008}$	$21.1^{+2.7}_{-7.2}$	$2.7^{+2.2}_{-1.2}$	$1.3^{+1.0}_{-0.6}$	$1.36^{+0.70}_{-0.47}$	$1.11e - 08$	Planet
206535016.01	$2163.3687^{+0.0027}_{-0.0029}$	$20.3980^{+0.0019}_{-0.0018}$	$89.63^{+0.26}_{-0.54}$	$0.0301^{+0.0036}_{-0.0022}$	77^{+14}_{-25}	$2.8^{+2.7}_{-1.3}$	$0.84^{+0.81}_{-0.41}$	$0.83^{+0.50}_{-0.32}$	$2.84e - 01$	Candidate
210363145.01	$2237.8065^{+0.0015}_{-0.0014}$	$8.19980^{+0.00035}_{-0.00034}$	$88.8^{+0.9}_{-1.6}$	$0.0293^{+0.0013}_{-0.0010}$	$22.9^{+2.9}_{-6.9}$	$2.7^{+3.0}_{-1.4}$	$0.84^{+0.94}_{-0.43}$	$0.71^{+0.47}_{-0.29}$	$1.22e - 07$	Planet
210402237.01	2237.2463 ± 0.0020	$10.99401^{+0.00062}_{-0.00060}$	$88.7^{+0.9}_{-1.6}$	$0.0278^{+0.0014}_{-0.0008}$	$17.9^{+1.6}_{-3.9}$	$3.4^{+3.1}_{-1.6}$	$1.1^{+1.0}_{-0.5}$	$1.07^{+0.61}_{-0.39}$	$0.00e + 00$	Planet
210423938.01	$2239.0159^{+0.0042}_{-0.0037}$	$19.8605^{+0.0020}_{-0.0021}$	$88.9^{+0.8}_{-2.1}$	$0.0277^{+0.0063}_{-0.0028}$	33^{+10}_{-17}	$2.2^{+2.4}_{-1.2}$	$0.72^{+0.79}_{-0.38}$	$0.63^{+0.43}_{-0.26}$	$6.46e - 02$	Candidate
210512842.01	$2234.1412^{+0.0029}_{-0.0028}$	5.86871 ± 0.00042	$87.9^{+1.5}_{-2.6}$	$0.0175^{+0.0012}_{-0.0008}$	$13.0^{+1.8}_{-3.6}$	$1.8^{+1.8}_{-0.9}$	$0.93^{+0.92}_{-0.45}$	$0.88^{+0.52}_{-0.34}$	$7.35e - 04$	Planet
210558622.01	$2231.2160^{+0.0011}_{-0.0012}$	$19.56272^{+0.00075}_{-0.00069}$	$88.9^{+0.7}_{-1.0}$	$0.0358^{+0.0023}_{-0.0010}$	$23.5^{+2.3}_{-4.4}$	$2.5^{+2.5}_{-1.2}$	$0.65^{+0.65}_{-0.32}$	$0.64^{+0.40}_{-0.25}$	$1.89e - 15$	Planet
210609658.01	$2241.4056^{+0.0012}_{-0.0011}$	14.14522 ± 0.00045	$86.4^{+1.7}_{-0.9}$	$0.0634^{+0.0015}_{-0.0020}$	$8.03^{+0.79}_{-0.51}$	$7.8^{+4.6}_{-2.9}$	$1.13^{+0.66}_{-0.43}$	$2.16^{+0.87}_{-0.65}$	$3.73e - 10$	Planet
210629082.01	2253.0149 ± 0.0051	$27.3526^{+0.0076}_{-0.0070}$	$88.9^{+0.7}_{-1.2}$	$0.0194^{+0.0024}_{-0.0012}$	$25.7^{+3.2}_{-6.7}$	$2.8^{+2.2}_{-1.2}$	$1.3^{+1.0}_{-0.6}$	$1.61^{+0.76}_{-0.54}$	$2.30e - 03$	Candidate
210643811.01	2240.2773 ± 0.0045	9.5258 ± 0.0013	$87.3^{+1.9}_{-3.6}$	$0.0133^{+0.0016}_{-0.0007}$	$10.8^{+1.6}_{-3.5}$	$1.8^{+1.3}_{-0.7}$	$1.22^{+0.88}_{-0.51}$	$1.58^{+0.76}_{-0.51}$	$4.99e - 04$	Planet
210667381.01	$2233.7858^{+0.0038}_{-0.0036}$	$5.32945^{+0.00063}_{-0.00074}$	$87.8^{+1.6}_{-3.1}$	$0.0160^{+0.0013}_{-0.0009}$	$13.5^{+2.2}_{-4.5}$	$1.7^{+1.8}_{-0.8}$	$0.9^{+1.0}_{-0.5}$	$0.79^{+0.48}_{-0.31}$	$7.11e - 04$	Planet
210707130.01	$2231.6822^{+0.00075}_{-0.00074}$	0.684553 ± 0.000013	$85.1^{+3.5}_{-6.6}$	$0.0182^{+0.0016}_{-0.0010}$	$5.6^{+0.8}_{-1.6}$	$1.3^{+1.4}_{-0.7}$	$0.65^{+0.68}_{-0.34}$	$0.62^{+0.39}_{-0.25}$	$5.10e - 05$	Planet
210718708.01	$2237.0167^{+0.0036}_{-0.0035}$	$8.77589^{+0.00088}_{-0.00090}$	$88.5^{+1.1}_{-2.4}$	$0.0252^{+0.0032}_{-0.0016}$	$20.2^{+3.6}_{-7.6}$	$2.2^{+2.1}_{-1.1}$	$0.79^{+0.76}_{-0.39}$	$0.81^{+0.48}_{-0.31}$	$9.40e - 06$	Planet
210775710.01	2231.69729 ± 0.00013	59.84857 ± 0.00018	$89.841^{+0.086}_{-0.074}$	$0.1010^{+0.0016}_{-0.0012}$	$113.9^{+4.3}_{-5.7}$	12^{+10}_{-6}	$1.08^{+0.94}_{-0.50}$	$1.07^{+0.61}_{-0.39}$	$1.32e - 02$	Unknown ⁴
210843708.01	$2231.1418^{+0.0014}_{-0.0013}$	0.704031 ± 0.000025	$39.0^{+8.6}_{-6.0}$	$0.40^{+0.39}_{-0.28}$	$1.77^{+0.35}_{-0.20}$	72^{+75}_{-53}	$1.64^{+0.63}_{-0.46}$	$5.9^{+1.7}_{-1.4}$	-	Unknown ³⁴
210848071.01	2235.5290 ± 0.0028	$41.6882^{+0.0034}_{-0.0035}$	$89.54^{+0.32}_{-0.53}$	$0.0226^{+0.0017}_{-0.0009}$	55^{+6}_{-13}	$2.5^{+2.2}_{-1.2}$	$1.03^{+0.91}_{-0.48}$	$1.08^{+0.59}_{-0.40}$	$2.51e - 03$	Candidate
210857328.01	2237.0802 ± 0.0071	$14.1551^{+0.0032}_{-0.0030}$	$87.1^{+2.1}_{-4.0}$	$0.0160^{+0.0019}_{-0.0009}$	$10.5^{+1.7}_{-3.6}$	$2.2^{+1.9}_{-1.0}$	$1.3^{+1.1}_{-0.6}$	$1.19^{+0.66}_{-0.42}$	$2.15e - 04$	Planet
210894022.01	$2234.9687^{+0.0047}_{-0.0045}$	$5.35143^{+0.00059}_{-0.00060}$	$87.5^{+1.8}_{-3.5}$	$0.01206^{+0.00096}_{-0.00067}$	$10.8^{+1.5}_{-3.2}$	$1.3^{+1.1}_{-0.6}$	$0.98^{+0.85}_{-0.45}$	$1.10^{+0.60}_{-0.40}$	$3.53e - 08$	Planet
210903662.01	2232.83880 ± 0.00020	2.410266 ± 0.000013	$72.8^{+4.3}_{-2.8}$	$0.51^{+0.34}_{-0.33}$	$4.96^{+0.36}_{-0.29}$	107^{+89}_{-79}	$1.92^{+0.96}_{-0.68}$	$4.1^{+2.2}_{-1.5}$	-	Unknown ⁴
210957318.01	2234.90561 ± 0.00024	4.098491 ± 0.000028	$86.55^{+0.42}_{-0.35}$	$0.1279^{+0.0025}_{-0.0035}$	$11.71^{+0.61}_{-0.49}$	14^{+13}_{-7}	$1.00^{+0.96}_{-0.49}$	$0.91^{+0.54}_{-0.35}$	-	Unknown ⁴
210965800.01	$2237.3364^{+0.0016}_{-0.0015}$	$8.74785^{+0.00036}_{-0.00037}$	$88.8^{+0.9}_{-1.5}$	$0.03665^{+0.00098}_{-0.00090}$	$18.8^{+1.6}_{-4.0}$	$3.9^{+3.8}_{-1.9}$	$0.99^{+0.96}_{-0.48}$	$0.88^{+0.52}_{-0.33}$	$4.03e - 04$	Planet
211002562.01	$2232.45273^{+0.00052}_{-0.00050}$	3.347948 ± 0.000045	$82.10^{+0.64}_{-0.50}$	$0.1159^{+0.0014}_{-0.0013}$	$5.64^{+0.24}_{-0.18}$	16^{+13}_{-7}	$1.24^{+0.99}_{-0.56}$	$1.31^{+0.70}_{-0.48}$	-	Unknown ⁴
211048999.01	$2233.5802^{+0.0015}_{-0.0014}$	5.17220 ± 0.00020	$88.6^{+1.0}_{-1.9}$	$0.0302^{+0.0023}_{-0.0014}$	$19.6^{+2.7}_{-5.9}$	$2.7^{+2.8}_{-1.4}$	$0.83^{+0.83}_{-0.43}$	$0.72^{+0.46}_{-0.28}$	$1.09e - 03$	Candidate

Table 2: Continued

EPIC	T_0 (BJD-2454833)	P (d)	i (deg)	R_p/R_*	a/R_*	R_p (R_\oplus)	R_* (R_\odot)	M_* (M_\odot)	FPP	Disposition
211087003.01	$2231.1667^{+0.0017}_{-0.0018}$	$28.2888^{+0.0018}_{-0.0017}$	$89.33^{+0.49}_{-0.83}$	$0.0347^{+0.0031}_{-0.0014}$	44^{+6}_{-13}	$4.1^{+3.7}_{-2.0}$	$1.09^{+0.97}_{-0.51}$	$1.05^{+0.59}_{-0.39}$	$2.47e - 02$	Candidate
211089792.01	2231.43151 ± 0.00010	$3.258825^{+0.000009}_{-0.000008}$	$86.92^{+0.61}_{-0.44}$	$0.1293^{+0.0038}_{-0.0035}$	$10.95^{+0.59}_{-0.40}$	13^{+13}_{-7}	$0.96^{+0.93}_{-0.49}$	$0.81^{+0.52}_{-0.32}$	-	Unknown ⁴
211106187.01	$2239.2743^{+0.0030}_{-0.0029}$	14.6431 ± 0.0014	$87.0^{+2.7}_{-1.5}$	$0.19^{+0.52}_{-0.15}$	24^{+40}_{-4}	50^{+140}_{-40}	$2.41^{+0.65}_{-0.53}$	$18.8^{+5.5}_{-4.5}$	-	Unknown ⁴
211147528.01	2232.4081 ± 0.0013	$2.349516^{+0.000077}_{-0.000075}$	$83.3^{+4.2}_{-2.5}$	$0.0923^{+0.0049}_{-0.0086}$	$6.1^{+1.7}_{-0.9}$	$23.7^{+9.0}_{-7.4}$	$2.35^{+0.89}_{-0.70}$	$6.6^{+2.4}_{-1.9}$	-	Unknown ⁴
211319617.01	2310.3954 ± 0.0016	8.86594 ± 0.00034	$88.6^{+1.0}_{-1.5}$	$0.0326^{+0.0023}_{-0.0012}$	$21.3^{+3.0}_{-5.7}$	$2.7^{+2.9}_{-1.4}$	$0.75^{+0.82}_{-0.38}$	$0.66^{+0.44}_{-0.27}$	$4.89e - 09$	Planet
211351816.01	$2309.0557^{+0.0052}_{-0.0047}$	8.4052 ± 0.0011	$86.6^{+2.5}_{-5.6}$	$0.0246^{+0.0033}_{-0.0013}$	$9.3^{+1.6}_{-3.7}$	$3.5^{+1.7}_{-1.2}$	$1.31^{+0.62}_{-0.44}$	$3.3^{+1.2}_{-0.9}$	$1.13e - 03$	Candidate
211355342.01	2310.7937 ± 0.0025	$6.89422^{+0.00043}_{-0.00042}$	$88.3^{+1.2}_{-2.4}$	$0.0252^{+0.0028}_{-0.0015}$	$17.7^{+2.8}_{-5.9}$	$3.0^{+2.8}_{-1.5}$	$1.1^{+1.0}_{-0.5}$	$1.02^{+0.58}_{-0.37}$	$9.48e - 04$	Planet
211359660.01	$2308.20585^{+0.00065}_{-0.00063}$	4.736881 ± 0.000071	$88.3^{+1.2}_{-1.8}$	$0.0321^{+0.0016}_{-0.0008}$	$13.5^{+1.1}_{-2.4}$	$3.0^{+3.0}_{-1.5}$	$0.86^{+0.86}_{-0.43}$	$0.78^{+0.47}_{-0.31}$	$1.59e - 04$	Planet
211391664.01	$2312.9800^{+0.0016}_{-0.0015}$	10.13679 ± 0.00041	$88.5^{+1.0}_{-1.7}$	$0.0305^{+0.0012}_{-0.0008}$	$14.5^{+1.1}_{-2.6}$	$4.1^{+2.8}_{-1.7}$	$1.24^{+0.85}_{-0.52}$	$1.66^{+0.78}_{-0.55}$	$1.69e - 04$	Planet
211401787.01	$2318.0684^{+0.0026}_{-0.0024}$	13.7739 ± 0.0011	$88.6^{+1.0}_{-2.4}$	$0.0180^{+0.0019}_{-0.0007}$	$19.9^{+2.7}_{-7.3}$	$2.5^{+1.7}_{-1.1}$	$1.30^{+0.88}_{-0.54}$	$1.85^{+0.80}_{-0.61}$	$4.67e - 03$	Candidate
211418290.01	$2308.80699^{+0.00083}_{-0.00084}$	5.03207 ± 0.00010	$88.5^{+1.0}_{-1.5}$	$0.09130^{+0.00068}_{-0.00065}$	$4.92^{+0.05}_{-0.10}$	$14.1^{+5.8}_{-4.2}$	$1.41^{+0.58}_{-0.42}$	$4.7^{+1.5}_{-1.2}$	-	Unknown ⁴
211424769.01	$2311.49835^{+0.00031}_{-0.00030}$	$5.176244^{+0.000039}_{-0.000041}$	$83.2^{+1.6}_{-1.2}$	$0.51^{+0.34}_{-0.31}$	$12.28^{+0.89}_{-0.75}$	65^{+70}_{-49}	$1.16^{+0.98}_{-0.53}$	$1.21^{+0.65}_{-0.42}$	-	Unknown ⁴
211432167.01	2308.92980 ± 0.00021	$5.817780^{+0.000030}_{-0.000029}$	$84.24^{+0.13}_{-0.14}$	$0.1092^{+0.0022}_{-0.0014}$	$8.39^{+0.13}_{-0.12}$	27^{+10}_{-8}	$2.26^{+0.83}_{-0.63}$	$6.9^{+2.0}_{-1.6}$	-	Unknown ⁴
211491383.01	$2308.5893^{+0.0067}_{-0.0090}$	$4.1453^{+0.0010}_{-0.0007}$	$86.7^{+2.4}_{-5.4}$	$0.0084^{+0.0012}_{-0.0007}$	$8.9^{+1.9}_{-3.3}$	$1.10^{+0.84}_{-0.49}$	$1.19^{+0.90}_{-0.52}$	$1.50^{+0.74}_{-0.50}$	-	Unknown ³
211525389.01	$2314.99168^{+0.00065}_{-0.00064}$	8.26681 ± 0.00013	$88.9^{+0.7}_{-1.2}$	$0.0343^{+0.0011}_{-0.0007}$	$18.1^{+1.0}_{-2.7}$	$3.8^{+3.6}_{-1.8}$	$1.02^{+0.95}_{-0.49}$	$0.93^{+0.55}_{-0.36}$	$1.60e - 07$	Planet
211594205.01	2315.5009 ± 0.0014	$16.99341^{+0.00087}_{-0.00083}$	$89.41^{+0.42}_{-0.72}$	$0.0185^{+0.0017}_{-0.0009}$	47^{+6}_{-13}	$1.7^{+1.7}_{-0.9}$	$0.85^{+0.86}_{-0.44}$	$0.74^{+0.49}_{-0.29}$	$3.43e - 04$	Planet
211606790.01	$2317.08963^{+0.00054}_{-0.00053}$	$37.24702^{+0.00073}_{-0.00078}$	$87.46^{+0.59}_{-0.52}$	$0.45^{+0.37}_{-0.27}$	$31.3^{+2.0}_{-1.6}$	55^{+59}_{-40}	$1.12^{+0.78}_{-0.46}$	$1.65^{+0.72}_{-0.53}$	-	Unknown ⁴
211682544.01	$2312.5676^{+0.0018}_{-0.0019}$	50.8192 ± 0.0025	$89.75^{+0.18}_{-0.28}$	$0.0236^{+0.0014}_{-0.0010}$	107^{+12}_{-26}	$2.4^{+2.5}_{-1.2}$	$0.92^{+0.97}_{-0.46}$	$0.81^{+0.50}_{-0.32}$	$8.75e - 03$	Candidate
211733267.01	2311.93174 ± 0.00015	$8.658168^{+0.000032}_{-0.000031}$	$86.53^{+0.76}_{-0.67}$	$0.50^{+0.35}_{-0.28}$	$23.3^{+1.4}_{-1.2}$	50^{+60}_{-37}	$0.91^{+0.89}_{-0.45}$	$0.84^{+0.51}_{-0.32}$	-	Unknown ⁴
211736671.01	2312.0974 ± 0.0013	4.73379 ± 0.00015	$86.2^{+2.7}_{-3.7}$	$0.0301^{+0.0026}_{-0.0014}$	$8.6^{+1.6}_{-2.4}$	$4.7^{+2.6}_{-1.7}$	$1.42^{+0.80}_{-0.51}$	$2.6^{+1.0}_{-0.8}$	$1.20e - 02$	Candidate
211743874.01	$2315.2086^{+0.0050}_{-0.0051}$	$12.2824^{+0.0017}_{-0.0018}$	$88.5^{+1.1}_{-2.0}$	$0.0164^{+0.0012}_{-0.0009}$	$19.1^{+2.8}_{-6.0}$	$2.2^{+1.6}_{-1.0}$	$1.25^{+0.90}_{-0.54}$	$1.56^{+0.74}_{-0.52}$	$6.01e - 04$	Planet
211763214.01	$2313.5932^{+0.0059}_{-0.0067}$	$21.1916^{+0.0034}_{-0.0030}$	$89.1^{+0.7}_{-1.3}$	$0.0154^{+0.0014}_{-0.0010}$	$30.0^{+4.7}_{-9.2}$	$1.5^{+1.4}_{-0.7}$	$0.86^{+0.80}_{-0.43}$	$0.84^{+0.50}_{-0.32}$	$4.59e - 03$	Candidate
211770696.01	$2312.9685^{+0.0048}_{-0.0047}$	$16.2730^{+0.0021}_{-0.0023}$	$88.1^{+1.4}_{-2.2}$	$0.0182^{+0.0016}_{-0.0008}$	$14.6^{+2.0}_{-3.9}$	$2.0^{+1.6}_{-0.9}$	$1.03^{+0.79}_{-0.45}$	$1.28^{+0.64}_{-0.44}$	$2.08e - 05$	Planet
211818569.01	$2310.560483^{+0.000095}_{-0.000093}$	5.185759 ± 0.000013	$88.77^{+0.54}_{-0.48}$	$0.1039^{+0.0036}_{-0.0031}$	$19.6^{+1.1}_{-1.3}$	$8.1^{+8.6}_{-4.2}$	$0.71^{+0.75}_{-0.37}$	$0.63^{+0.42}_{-0.25}$	$9.74e - 04$	Planet

Table 2: Continued

EPIC	T_0 (BJD-2454833)	P (d)	i (deg)	R_p/R_*	a/R_*	R_p (R_{\oplus})	R_* (R_{\odot})	M_* (M_{\odot})	FPP	Disposition
211886472.01	2319.37961 ± 0.00016	$19.640123^{+0.000084}_{-0.000081}$	$87.70^{+0.50}_{-0.38}$	0.53 ± 0.31	$36.3^{+2.2}_{-1.8}$	91^{+76}_{-62}	$1.57^{+0.92}_{-0.57}$	$2.6^{+1.1}_{-0.8}$	-	Unknown ⁴
211906650.01	$2321.8455^{+0.0018}_{-0.0019}$	$41.4742^{+0.0032}_{-0.0044}$	$89.50^{+0.35}_{-0.60}$	$0.02974^{+0.00087}_{-0.00081}$	49^{+5}_{-11}	$3.5^{+3.1}_{-1.6}$	$1.07^{+0.95}_{-0.51}$	$1.02^{+0.58}_{-0.38}$	$1.34e - 05$	Planet
211913977.01	$2319.6820^{+0.0022}_{-0.0023}$	$14.67723^{+0.00080}_{-0.00083}$	$88.9^{+0.8}_{-1.7}$	$0.0261^{+0.0032}_{-0.0013}$	29^{+5}_{-11}	$2.3^{+2.5}_{-1.2}$	$0.82^{+0.88}_{-0.42}$	$0.70^{+0.45}_{-0.28}$	$3.94e - 03$	Candidate
211939692.01	2321.219 ± 0.011	$19.7738^{+0.0053}_{-0.0054}$	$88.4^{+1.2}_{-2.4}$	$0.0149^{+0.0018}_{-0.0011}$	$17.6^{+2.7}_{-5.8}$	$2.0^{+1.6}_{-0.9}$	$1.24^{+0.97}_{-0.56}$	$1.41^{+0.70}_{-0.47}$	$2.73e - 03$	Candidate
211941472.01	$2310.6171^{+0.0076}_{-0.0078}$	5.7818 ± 0.0013	$87.3^{+1.9}_{-3.7}$	$0.0097^{+0.0012}_{-0.0008}$	$10.0^{+1.9}_{-2.9}$	$1.24^{+0.90}_{-0.53}$	$1.17^{+0.84}_{-0.49}$	$1.57^{+0.76}_{-0.52}$	$3.16e - 02$	Candidate
211945201.01	$2325.82593^{+0.00065}_{-0.00067}$	19.49179 ± 0.00051	$89.33^{+0.47}_{-0.67}$	$0.0380^{+0.0023}_{-0.0011}$	$38.9^{+4.2}_{-8.3}$	$5.2^{+3.7}_{-2.2}$	$1.25^{+0.88}_{-0.53}$	$1.57^{+0.76}_{-0.52}$	$2.22e - 01$	Candidate
211978988.01	$2319.7053^{+0.0032}_{-0.0026}$	$36.5560^{+0.0038}_{-0.0041}$	$89.36^{+0.45}_{-0.77}$	$0.0262^{+0.0018}_{-0.0011}$	40^{+4}_{-10}	$3.1^{+2.6}_{-1.4}$	$1.09^{+0.90}_{-0.50}$	$1.20^{+0.64}_{-0.43}$	$5.95e - 03$	Candidate
211993818.01	$2316.02846^{+0.00027}_{-0.00026}$	8.986646 ± 0.000066	$82.5^{+1.6}_{-1.3}$	$0.53^{+0.33}_{-0.27}$	$10.36^{+0.64}_{-0.36}$	97^{+73}_{-56}	$1.69^{+0.67}_{-0.49}$	$5.5^{+1.7}_{-1.4}$	-	Unknown ⁴
212006318.01	$2314.325^{+0.011}_{-0.009}$	$14.4608^{+0.0035}_{-0.0043}$	$87.8^{+1.6}_{-3.1}$	$0.0152^{+0.0017}_{-0.0010}$	$13.8^{+2.3}_{-4.7}$	$1.8^{+1.5}_{-0.8}$	$1.11^{+0.92}_{-0.50}$	$1.20^{+0.64}_{-0.43}$	$4.39e - 03$	Candidate
212006344.01	2308.8286 ± 0.0012	$2.219405^{+0.000065}_{-0.000064}$	$87.9^{+1.5}_{-2.7}$	$0.0202^{+0.0010}_{-0.0009}$	$12.8^{+1.8}_{-3.6}$	$1.1^{+1.2}_{-0.6}$	$0.50^{+0.57}_{-0.27}$	$0.50^{+0.34}_{-0.21}$	$1.84e - 05$	Planet
212008766.01	$2312.1114^{+0.0025}_{-0.0024}$	$14.13348^{+0.00097}_{-0.00098}$	$88.9^{+0.8}_{-1.5}$	$0.0286^{+0.0059}_{-0.0019}$	$26.5^{+3.7}_{-8.5}$	$2.5^{+2.8}_{-1.3}$	$0.80^{+0.88}_{-0.40}$	$0.67^{+0.44}_{-0.27}$	$2.34e - 03$	Candidate
212012119.01	2309.1346 ± 0.0022	3.28086 ± 0.00017	$87.7^{+1.7}_{-3.2}$	$0.0271^{+0.0018}_{-0.0014}$	$12.1^{+1.7}_{-3.6}$	$2.3^{+2.0}_{-1.1}$	$0.79^{+0.69}_{-0.38}$	$0.88^{+0.49}_{-0.33}$	$1.78e - 03$	Candidate
212110888.01	$2308.351091^{+0.000087}_{-0.000088}$	2.995646 ± 0.000006	$83.22^{+0.27}_{-0.25}$	$0.0881^{+0.0018}_{-0.0011}$	$6.87^{+0.16}_{-0.15}$	$11.8^{+8.4}_{-5.0}$	$1.22^{+0.88}_{-0.52}$	$1.61^{+0.74}_{-0.54}$	-	Unknown ⁴
212132195.01	$2331.3906^{+0.0015}_{-0.0016}$	$26.1972^{+0.0023}_{-0.0022}$	$89.50^{+0.36}_{-0.71}$	$0.0314^{+0.0018}_{-0.0014}$	55^{+7}_{-17}	$2.5^{+2.7}_{-1.3}$	$0.72^{+0.80}_{-0.38}$	$0.63^{+0.42}_{-0.26}$	$1.54e - 03$	Candidate
212138198.01	$2309.37283^{+0.00056}_{-0.00057}$	$3.209153^{+0.000043}_{-0.000042}$	$82.8^{+4.8}_{-2.2}$	$0.32^{+0.45}_{-0.27}$	$10.7^{+8.9}_{-1.2}$	33^{+56}_{-32}	$0.93^{+0.90}_{-0.46}$	$0.85^{+0.52}_{-0.33}$	-	Unknown ⁴
212303338.01	$2385.3924^{+0.0036}_{-0.0033}$	$0.595622^{+0.000044}_{-0.000046}$	$84.4^{+4.1}_{-9.7}$	$0.0063^{+0.0011}_{-0.0007}$	$5.0^{+2.0}_{-1.8}$	$0.66^{+0.64}_{-0.34}$	$0.96^{+0.91}_{-0.47}$	$0.90^{+0.53}_{-0.34}$	$2.16e - 02$	Candidate
212357477.01	2388.2300 ± 0.0013	6.32666 ± 0.00019	$88.6^{+1.0}_{-1.9}$	$0.0206^{+0.0018}_{-0.0009}$	$21.7^{+3.4}_{-7.2}$	$2.3^{+2.3}_{-1.1}$	$1.0^{+1.0}_{-0.5}$	$0.94^{+0.53}_{-0.36}$	$1.45e - 03$	Candidate
212394689.01	$2390.4181^{+0.0014}_{-0.0015}$	6.67934 ± 0.00024	$88.2^{+1.3}_{-2.9}$	$0.0265^{+0.0028}_{-0.0012}$	$17.1^{+2.9}_{-6.5}$	$2.8^{+2.8}_{-1.4}$	$0.96^{+0.95}_{-0.49}$	$0.79^{+0.50}_{-0.31}$	$4.20e - 06$	Planet
212394689.02	$2420.2044^{+0.0018}_{-0.0017}$	5.17631 ± 0.00041	$88.1^{+1.4}_{-2.7}$	$0.0161^{+0.0014}_{-0.0009}$	$15.0^{+2.2}_{-4.8}$	$1.7^{+1.6}_{-0.9}$	$0.95^{+0.91}_{-0.48}$	$0.81^{+0.50}_{-0.32}$	$6.48e - 11$	Planet
212460519.01	2390.7941 ± 0.0014	$7.38706^{+0.00026}_{-0.00027}$	$88.7^{+0.9}_{-1.5}$	$0.0280^{+0.0017}_{-0.0010}$	$20.2^{+2.5}_{-4.9}$	$1.8^{+2.0}_{-0.9}$	$0.59^{+0.65}_{-0.31}$	$0.55^{+0.37}_{-0.23}$	$6.48e - 11$	Planet
212480208.01	2391.7677 ± 0.0025	$10.09889^{+0.00061}_{-0.00063}$	$88.5^{+1.1}_{-2.2}$	$0.01365^{+0.00098}_{-0.00056}$	$17.6^{+2.1}_{-5.5}$	$1.5^{+1.3}_{-0.7}$	$0.97^{+0.85}_{-0.46}$	$1.06^{+0.58}_{-0.39}$	$1.70e - 11$	Planet
212480208.02	$2395.6930^{+0.0059}_{-0.0069}$	$21.5737^{+0.0056}_{-0.0041}$	$89.1^{+0.6}_{-1.2}$	$0.01099^{+0.00073}_{-0.00057}$	$29.1^{+4.1}_{-8.2}$	$1.2^{+1.1}_{-0.5}$	$0.98^{+0.87}_{-0.45}$	$1.05^{+0.58}_{-0.38}$	$9.60e - 09$	Planet
212496592.01	$2386.5568^{+0.0029}_{-0.0028}$	$2.85866^{+0.00016}_{-0.00017}$	$86.7^{+2.4}_{-4.9}$	$0.0175^{+0.0031}_{-0.0014}$	$8.5^{+1.4}_{-2.7}$	$1.8^{+1.8}_{-0.9}$	$0.92^{+0.91}_{-0.46}$	$0.83^{+0.51}_{-0.32}$	$5.17e - 08$	Planet
212521166.01	$2386.87433^{+0.00067}_{-0.00065}$	13.86392 ± 0.00022	$89.35^{+0.45}_{-0.64}$	$0.0335^{+0.0014}_{-0.0008}$	$32.3^{+2.1}_{-4.9}$	$2.7^{+2.6}_{-1.4}$	$0.75^{+0.71}_{-0.37}$	$0.79^{+0.46}_{-0.30}$	$1.82e - 09$	Planet

Table 2: Continued

EPIC	T_0 (BJD-2454833)	P (d)	i (deg)	R_p/R_*	a/R_*	R_p (R_{\oplus})	R_* (R_{\odot})	M_* (M_{\odot})	FPP	Disposition
212534729.01	2390.5242 $^{+0.0043}_{-0.0052}$	13.4849 $^{+0.0014}_{-0.0013}$	89.1 $^{+0.7}_{-1.2}$	0.0174 $^{+0.0020}_{-0.0014}$	30.2 $^{+5.5}_{-8.7}$	1.7 $^{+1.6}_{-0.8}$	0.91 $^{+0.83}_{-0.43}$	0.93 $^{+0.54}_{-0.35}$	5.20e - 04	Planet
212555594.01	2387.4424 \pm 0.0021	4.16321 $^{+0.00021}_{-0.00020}$	88.4 $^{+1.1}_{-2.2}$	0.0175 $^{+0.0015}_{-0.0011}$	17.6 $^{+2.8}_{-5.4}$	1.7 $^{+1.6}_{-0.8}$	0.91 $^{+0.85}_{-0.44}$	0.89 $^{+0.50}_{-0.33}$	8.99e - 05	Planet
212562715.01	2387.4691 $^{+0.0028}_{-0.0030}$	13.5248 $^{+0.0011}_{-0.0009}$	89.26 $^{+0.53}_{-0.91}$	0.0236 $^{+0.0016}_{-0.0013}$	37 $^{+6}_{-10}$	2.5 $^{+2.6}_{-1.3}$	1.0 $^{+1.0}_{-0.5}$	0.83 $^{+0.51}_{-0.32}$	4.03e - 03	Candidate
212572439.01	2384.86557 \pm 0.00015	2.581475 \pm 0.000008	84.01 $^{+0.72}_{-0.59}$	0.0746 $^{+0.0022}_{-0.0024}$	7.70 $^{+0.57}_{-0.43}$	7.5 $^{+6.8}_{-3.6}$	0.92 $^{+0.84}_{-0.45}$	0.93 $^{+0.53}_{-0.34}$	3.06e - 02	Candidate
212577658.01	2388.3214 \pm 0.0021	14.06972 $^{+0.00069}_{-0.00068}$	89.0 $^{+0.7}_{-1.4}$	0.0193 $^{+0.0014}_{-0.0008}$	31 $^{+5}_{-11}$	2.1 $^{+2.0}_{-1.0}$	0.99 $^{+0.93}_{-0.48}$	0.92 $^{+0.54}_{-0.34}$	1.59e - 04	Planet
212580872.01	2391.2590 \pm 0.0011	14.78717 \pm 0.00044	89.10 $^{+0.61}_{-0.84}$	0.0386 $^{+0.0016}_{-0.0009}$	24.9 $^{+1.9}_{-4.0}$	4.4 $^{+4.0}_{-2.1}$	1.05 $^{+0.94}_{-0.50}$	1.00 $^{+0.57}_{-0.36}$	1.43e - 05	Planet
212586030.01	2387.8835 $^{+0.0034}_{-0.0040}$	7.78505 $^{+0.00082}_{-0.00064}$	89.1 $^{+0.7}_{-1.5}$	0.0232 $^{+0.0033}_{-0.0024}$	28.4 $^{+7.1}_{-9.3}$	2.9 $^{+1.9}_{-1.2}$	1.13 $^{+0.75}_{-0.45}$	1.83 $^{+0.79}_{-0.58}$	9.99e - 01	Candidate
212587672.01	2404.0437 \pm 0.0036	23.2260 $^{+0.0030}_{-0.0031}$	89.2 $^{+0.5}_{-1.3}$	0.0221 $^{+0.0043}_{-0.0019}$	43 $^{+9}_{-18}$	2.5 $^{+2.3}_{-1.2}$	1.02 $^{+0.95}_{-0.50}$	0.98 $^{+0.56}_{-0.37}$	3.57e - 02	Candidate
212639319.01	2389.4365 $^{+0.0027}_{-0.0028}$	13.84377 \pm 0.00089	85.6 $^{+3.6}_{-1.5}$	0.30 $^{+0.47}_{-0.27}$	18 $^{+29}_{-3}$	40 $^{+68}_{-39}$	1.21 $^{+0.80}_{-0.49}$	1.85 $^{+0.82}_{-0.59}$	-	Unknown ⁴
212672300.01	2410.0073 $^{+0.0041}_{-0.0046}$	39.7213 $^{+0.0055}_{-0.0056}$	89.0 $^{+0.7}_{-1.4}$	0.0262 $^{+0.0026}_{-0.0011}$	31 $^{+5}_{-11}$	3.5 $^{+2.6}_{-1.5}$	1.21 $^{+0.91}_{-0.52}$	1.42 $^{+0.72}_{-0.49}$	5.23e - 05	Planet
212679181.01	2385.60472 $^{+0.00055}_{-0.00056}$	1.054595 $^{+0.000013}_{-0.000014}$	87.7 $^{+1.6}_{-3.7}$	0.0242 $^{+0.0033}_{-0.0018}$	13.1 $^{+2.9}_{-4.8}$	1.3 $^{+1.5}_{-0.7}$	0.50 $^{+0.58}_{-0.27}$	0.47 $^{+0.32}_{-0.20}$	5.25e - 05	Planet
212686205.01	2388.4483 $^{+0.0034}_{-0.0033}$	5.67582 $^{+0.00042}_{-0.00044}$	88.5 $^{+1.1}_{-2.2}$	0.0171 $^{+0.0015}_{-0.0010}$	19.9 $^{+3.4}_{-7.0}$	1.3 $^{+1.4}_{-0.7}$	0.68 $^{+0.73}_{-0.35}$	0.61 $^{+0.40}_{-0.25}$	2.75e - 04	Planet
212689874.01	2392.0459 $^{+0.0017}_{-0.0018}$	15.85355 $^{+0.00077}_{-0.00074}$	89.0 $^{+0.7}_{-1.4}$	0.0298 $^{+0.0010}_{-0.0007}$	23.8 $^{+2.2}_{-6.3}$	3.2 $^{+3.1}_{-1.6}$	0.99 $^{+0.96}_{-0.50}$	0.88 $^{+0.53}_{-0.34}$	3.68e - 12	Planet
212689874.02	2410.0090 $^{+0.0065}_{-0.0057}$	28.4827 $^{+0.0067}_{-0.0083}$	88.8 $^{+0.9}_{-2.1}$	0.0258 $^{+0.0020}_{-0.0010}$	31 $^{+8}_{-15}$	2.8 $^{+2.8}_{-1.4}$	1.00 $^{+0.98}_{-0.49}$	0.87 $^{+0.55}_{-0.33}$	8.36e - 06	Planet
212691422.01	2394.8911 $^{+0.0052}_{-0.0054}$	48.3243 $^{+0.0078}_{-0.0085}$	87.8 \pm 1.8	0.0216 $^{+0.0017}_{-0.0013}$	21 $^{+11}_{-7}$	3.0 $^{+2.1}_{-1.2}$	1.27 $^{+0.88}_{-0.52}$	1.70 $^{+0.81}_{-0.56}$	3.27e - 09	Planet
212697709.01	2385.28702 $^{+0.00011}_{-0.00010}$	3.951625 \pm 0.000009	85.13 $^{+0.26}_{-0.25}$	0.0950 $^{+0.0033}_{-0.0024}$	10.33 $^{+0.36}_{-0.33}$	12 $^{+10}_{-6}$	1.1 $^{+1.0}_{-0.5}$	1.07 $^{+0.60}_{-0.39}$	-	Unknown ⁴
212703473.01	2389.7255 \pm 0.0024	6.78907 $^{+0.00036}_{-0.00037}$	88.4 $^{+1.2}_{-2.0}$	0.01505 $^{+0.00065}_{-0.00051}$	16.5 $^{+2.0}_{-4.4}$	1.7 $^{+1.6}_{-0.8}$	1.07 $^{+0.98}_{-0.50}$	1.01 $^{+0.57}_{-0.37}$	1.20e - 06	Planet
212703473.02	2388.1643 \pm 0.0024	18.51729 $^{+0.00088}_{-0.00089}$	89.40 $^{+0.42}_{-0.73}$	0.01733 $^{+0.00076}_{-0.00063}$	46 $^{+6}_{-12}$	2.0 $^{+1.9}_{-1.0}$	1.07 $^{+0.98}_{-0.53}$	1.00 $^{+0.57}_{-0.38}$	1.82e - 04	Planet
212735333.01	2385.1829 \pm 0.0017	8.35796 \pm 0.00029	88.5 $^{+1.0}_{-1.7}$	0.0252 $^{+0.0013}_{-0.0008}$	17.0 $^{+1.7}_{-3.9}$	2.7 $^{+2.7}_{-1.4}$	1.00 $^{+0.98}_{-0.51}$	0.84 $^{+0.53}_{-0.33}$	5.22e - 05	Planet
212768333.01	2388.61179 $^{+0.00073}_{-0.00071}$	17.04316 $^{+0.00033}_{-0.00032}$	89.37 $^{+0.46}_{-0.63}$	0.0486 $^{+0.0025}_{-0.0015}$	41.7 $^{+4.5}_{-8.9}$	4.6 $^{+4.8}_{-2.3}$	0.86 $^{+0.90}_{-0.44}$	0.74 $^{+0.48}_{-0.30}$	8.56e - 04	Planet
212803289.01	2400.8259 \pm 0.0011	18.24876 $^{+0.00064}_{-0.00062}$	87.6 $^{+1.6}_{-1.4}$	0.0425 $^{+0.0012}_{-0.0008}$	11.4 $^{+1.3}_{-1.5}$	7.0 $^{+3.9}_{-2.6}$	1.52 $^{+0.84}_{-0.56}$	2.6 $^{+1.0}_{-0.8}$	1.31e - 05	Planet
212828909.01	2385.5608 $^{+0.0030}_{-0.0029}$	2.84989 \pm 0.00019	87.7 $^{+1.7}_{-3.7}$	0.0160 $^{+0.0019}_{-0.0012}$	12.9 $^{+2.5}_{-4.8}$	1.5 $^{+1.6}_{-0.8}$	0.86 $^{+0.91}_{-0.45}$	0.68 $^{+0.45}_{-0.27}$	8.81e - 05	Planet
213546283.01	2469.3568 $^{+0.0014}_{-0.0015}$	9.77018 $^{+0.00033}_{-0.00032}$	88.9 $^{+0.8}_{-1.3}$	0.0295 $^{+0.0017}_{-0.0010}$	22.8 $^{+2.5}_{-5.5}$	3.3 $^{+2.6}_{-1.5}$	1.02 $^{+0.82}_{-0.46}$	1.19 $^{+0.65}_{-0.42}$	3.51e - 03	Candidate
213817056.01	2478.9449 $^{+0.0051}_{-0.0053}$	13.6136 \pm 0.0017	82.9 $^{+5.5}_{-2.4}$	0.30 $^{+0.46}_{-0.26}$	11 $^{+15}_{-2}$	28 $^{+49}_{-28}$	0.86 $^{+0.77}_{-0.39}$	0.98 $^{+0.53}_{-0.36}$	-	Unknown ⁴

Table 2: Continued

EPIC	T_0 (BJD-2454833)	P (d)	i (deg)	R_p/R_*	a/R_*	R_p (R_\oplus)	R_* (R_\odot)	M_* (M_\odot)	FPP	Disposition
214082960.01	2481.6660 $^{+0.0031}_{-0.0013}$	19.5982 $^{+0.0006}_{-0.0014}$	89.86 $^{+0.11}_{-0.22}$	0.032 $^{+0.010}_{-0.003}$	186 $^{+70}_{-58}$	3.5 $^{+3.5}_{-1.7}$	0.99 $^{+0.96}_{-0.49}$	0.83 $^{+0.55}_{-0.34}$	5.59e - 01	Candidate
214173069.01	2470.9071 \pm 0.0036	8.77644 $^{+0.00070}_{-0.00069}$	88.8 $^{+0.8}_{-1.6}$	0.0295 $^{+0.0021}_{-0.0016}$	24.2 $^{+3.7}_{-7.5}$	2.7 $^{+2.2}_{-1.2}$	0.83 $^{+0.69}_{-0.38}$	1.05 $^{+0.57}_{-0.37}$	4.10e - 06	Planet
214234110.01	2470.8795 \pm 0.0014	4.63790 $^{+0.00015}_{-0.00014}$	89.1 $^{+0.6}_{-1.2}$	0.0173 $^{+0.0016}_{-0.0013}$	30.2 $^{+5.2}_{-8.9}$	2.1 $^{+1.8}_{-1.0}$	1.11 $^{+0.95}_{-0.55}$	1.00 $^{+0.60}_{-0.37}$	5.37e - 01	Candidate
214254518.01	2471.2168 $^{+0.0045}_{-0.0044}$	5.05903 $^{+0.00051}_{-0.00049}$	87.9 $^{+1.5}_{-3.3}$	0.0154 $^{+0.0020}_{-0.0012}$	14.1 $^{+2.6}_{-5.2}$	1.1 $^{+1.1}_{-0.6}$	0.63 $^{+0.67}_{-0.33}$	0.60 $^{+0.40}_{-0.24}$	-	Unknown ³
215171927.01	2468.8704 \pm 0.0035	4.13574 $^{+0.00031}_{-0.00034}$	87.7 $^{+1.7}_{-3.4}$	0.0193 $^{+0.0017}_{-0.0012}$	13.1 $^{+2.4}_{-4.7}$	1.7 $^{+1.7}_{-0.9}$	0.83 $^{+0.78}_{-0.41}$	0.82 $^{+0.49}_{-0.31}$	1.16e - 08	Planet
215171927.02	2473.8954 $^{+0.0066}_{-0.0069}$	6.6312 $^{+0.0011}_{-0.0010}$	88.4 $^{+1.2}_{-2.7}$	0.0165 $^{+0.0017}_{-0.0013}$	17.9 $^{+3.8}_{-6.6}$	1.5 $^{+1.4}_{-0.7}$	0.82 $^{+0.77}_{-0.40}$	0.82 $^{+0.49}_{-0.31}$	1.27e - 07	Planet
215502661.01	2473.221 \pm 0.010	21.5228 $^{+0.0052}_{-0.0057}$	89.0 $^{+0.7}_{-1.9}$	0.0164 $^{+0.0039}_{-0.0016}$	31 $^{+7}_{-13}$	2.0 $^{+1.6}_{-0.9}$	1.10 $^{+0.83}_{-0.48}$	1.33 $^{+0.66}_{-0.45}$	5.52e - 01	Candidate
215854715.01	2477.0807 $^{+0.0051}_{-0.0054}$	11.1237 $^{+0.0015}_{-0.0013}$	88.5 $^{+1.1}_{-2.2}$	0.0194 $^{+0.0020}_{-0.0012}$	20.4 $^{+3.5}_{-7.2}$	1.9 $^{+1.9}_{-1.0}$	0.90 $^{+0.91}_{-0.46}$	0.77 $^{+0.50}_{-0.30}$	1.97e - 08	Planet
216050437.01	2475.24061 $^{+0.00075}_{-0.00072}$	14.94899 $^{+0.00029}_{-0.00030}$	84.8 $^{+1.2}_{-1.0}$	0.49 $^{+0.36}_{-0.31}$	16.1 $^{+1.5}_{-1.2}$	79 $^{+83}_{-61}$	1.5 $^{+1.1}_{-0.6}$	1.61 $^{+0.88}_{-0.60}$	-	Unknown ⁴
216114172.01	2470.2130 $^{+0.0076}_{-0.0075}$	13.1252 \pm 0.0021	88.8 $^{+0.8}_{-1.5}$	0.0157 $^{+0.0017}_{-0.0012}$	22.6 $^{+3.3}_{-6.3}$	1.8 $^{+1.7}_{-0.9}$	1.1 $^{+1.0}_{-0.5}$	0.97 $^{+0.56}_{-0.37}$	2.10e - 04	Planet
216166748.01	2470.3618 \pm 0.0025	19.6795 \pm 0.0011	88.8 $^{+0.9}_{-1.9}$	0.0212 $^{+0.0038}_{-0.0013}$	29 $^{+6}_{-12}$	2.5 $^{+2.4}_{-1.2}$	1.1 $^{+1.0}_{-0.5}$	0.97 $^{+0.58}_{-0.37}$	1.63e - 04	Planet ¹
216387101.01	2470.0123 $^{+0.0082}_{-0.0079}$	9.7615 $^{+0.0016}_{-0.0015}$	88.1 $^{+1.3}_{-2.7}$	0.0167 $^{+0.0025}_{-0.0014}$	15.3 $^{+2.8}_{-5.0}$	2.1 $^{+1.3}_{-0.8}$	1.15 $^{+0.71}_{-0.44}$	1.97 $^{+0.83}_{-0.60}$	1.77e - 02	Candidate
216405287.01	2471.2515 \pm 0.0016	3.40517 \pm 0.00012	87.8 $^{+1.6}_{-2.8}$	0.0232 $^{+0.0011}_{-0.0009}$	12.2 $^{+1.5}_{-3.3}$	2.6 $^{+2.5}_{-1.3}$	1.02 $^{+0.99}_{-0.50}$	0.89 $^{+0.52}_{-0.35}$	1.04e - 08	Planet
216468514.01	2471.52446 \pm 0.00014	3.313921 \pm 0.000010	82.37 $^{+0.33}_{-0.27}$	0.0828 $^{+0.0017}_{-0.0012}$	5.93 $^{+0.14}_{-0.11}$	12.2 $^{+9.6}_{-5.4}$	1.4 $^{+1.1}_{-0.6}$	1.45 $^{+0.72}_{-0.51}$	-	Unknown ⁴
216494238.01	2474.5838 $^{+0.0057}_{-0.0055}$	19.8945 \pm 0.0027	88.6 $^{+1.0}_{-1.6}$	0.0478 $^{+0.0023}_{-0.0019}$	17.5 $^{+1.7}_{-3.8}$	6.0 $^{+5.8}_{-2.9}$	1.1 $^{+1.1}_{-0.6}$	1.03 $^{+0.61}_{-0.39}$	2.47e - 06	Planet
216892056.01	2470.04807 $^{+0.00037}_{-0.00038}$	2.785913 \pm 0.000024	84.9 $^{+3.2}_{-1.6}$	0.34 $^{+0.44}_{-0.29}$	15 $^{+10}_{-2}$	20 $^{+34}_{-20}$	0.54 $^{+0.61}_{-0.29}$	0.51 $^{+0.34}_{-0.22}$	-	Unknown ⁴
217221649.01	2471.461 \pm 0.012	3.6428 $^{+0.0010}_{-0.0011}$	84.5 $^{+3.9}_{-7.7}$	0.0082 $^{+0.0012}_{-0.0007}$	4.7 $^{+1.0}_{-1.3}$	3.5 $^{+1.3}_{-1.0}$	3.9 $^{+1.3}_{-1.1}$	15.9 $^{+7.3}_{-5.3}$	1.54e - 03	Candidate
217855533.01	2487.3845 $^{+0.0063}_{-0.0059}$	21.5876 $^{+0.0045}_{-0.0051}$	88.9 $^{+0.8}_{-1.7}$	0.0113 $^{+0.0015}_{-0.0008}$	30 $^{+6}_{-12}$	1.6 $^{+1.1}_{-0.7}$	1.30 $^{+0.92}_{-0.54}$	1.66 $^{+0.79}_{-0.55}$	3.12e - 03	Candidate
217941732.01	2470.2003 $^{+0.0023}_{-0.0022}$	2.49416 \pm 0.00012	87.2 $^{+2.0}_{-3.7}$	0.0154 $^{+0.0019}_{-0.0012}$	9.9 $^{+1.7}_{-2.9}$	1.1 $^{+1.1}_{-0.5}$	0.65 $^{+0.65}_{-0.32}$	0.66 $^{+0.40}_{-0.26}$	1.19e - 06	Planet
218131080.01	2468.80842 $^{+0.00025}_{-0.00026}$	3.142846 \pm 0.000017	83.2 $^{+1.5}_{-1.0}$	0.0626 $^{+0.0008}_{-0.0011}$	4.80 $^{+0.31}_{-0.22}$	8.9 $^{+6.9}_{-4.0}$	1.3 $^{+1.0}_{-0.6}$	1.46 $^{+0.76}_{-0.52}$	0.00e + 00	Planet
218170789.01	2470.4021 $^{+0.0047}_{-0.0050}$	3.04163 $^{+0.00032}_{-0.00031}$	49.8 $^{+8.1}_{-6.9}$	0.37 $^{+0.41}_{-0.27}$	2.15 $^{+0.35}_{-0.24}$	38 $^{+53}_{-33}$	0.95 $^{+0.79}_{-0.43}$	1.12 $^{+0.61}_{-0.39}$	-	Unknown ⁴
218304292.01	2473.8161 $^{+0.0022}_{-0.0023}$	8.42163 \pm 0.00038	87.8 $^{+1.9}_{-1.6}$	0.24 $^{+0.50}_{-0.21}$	34 $^{+63}_{-12}$	28 $^{+62}_{-28}$	1.08 $^{+0.81}_{-0.46}$	1.48 $^{+0.72}_{-0.49}$	-	Unknown ⁴
218668602.01	2469.0914 $^{+0.0030}_{-0.0031}$	1.86598 \pm 0.00012	85.5 $^{+3.2}_{-6.0}$	0.0206 $^{+0.0020}_{-0.0014}$	6.4 $^{+1.1}_{-1.9}$	2.1 $^{+2.2}_{-1.1}$	0.91 $^{+0.99}_{-0.47}$	0.73 $^{+0.47}_{-0.29}$	1.39e - 03	Candidate
218916923.01	2492.81729 \pm 0.00037	28.38208 $^{+0.00030}_{-0.00029}$	89.56 $^{+0.29}_{-0.21}$	0.0974 $^{+0.0024}_{-0.0021}$	45.8 $^{+2.2}_{-2.7}$	10 $^{+11}_{-5}$	1.0 $^{+1.0}_{-0.5}$	0.77 $^{+0.48}_{-0.30}$	-	Unknown ⁴

Table 2: Continued

EPIC	T_0 (BJD-2454833)	P (d)	i (deg)	R_p/R_*	a/R_*	R_p (R_{\oplus})	R_* (R_{\odot})	M_* (M_{\odot})	FPP	Disposition
219388192.01	2470.98880 ± 0.00027	$5.292606^{+0.000030}_{-0.000031}$	$89.21^{+0.55}_{-0.74}$	$0.0945^{+0.0010}_{-0.0007}$	$13.31^{+0.22}_{-0.54}$	11^{+10}_{-5}	$1.09^{+0.97}_{-0.52}$	$1.03^{+0.60}_{-0.38}$	-	Unknown ⁴
220170303.01	$2563.6387^{+0.0060}_{-0.0059}$	9.6951 ± 0.0013	$88.5^{+1.1}_{-2.2}$	$0.0165^{+0.0022}_{-0.0013}$	$19.3^{+3.5}_{-6.5}$	$1.5^{+1.4}_{-0.7}$	$0.83^{+0.76}_{-0.39}$	$0.93^{+0.50}_{-0.35}$	$3.30e - 02$	Candidate
220186645.01	2563.5088 ± 0.0037	7.05572 ± 0.00068	$87.7^{+1.7}_{-3.2}$	$0.02369^{+0.00095}_{-0.00087}$	$11.1^{+1.2}_{-3.1}$	$2.9^{+2.3}_{-1.3}$	$1.14^{+0.89}_{-0.50}$	$1.34^{+0.68}_{-0.46}$	$3.05e - 05$	Planet
220187552.01	$2566.31466^{+0.00011}_{-0.00010}$	$17.093398^{+0.000043}_{-0.000044}$	$88.40^{+0.24}_{-0.23}$	$0.57^{+0.27}_{-0.21}$	$47.7^{+3.0}_{-1.6}$	33^{+40}_{-21}	$0.53^{+0.58}_{-0.28}$	$0.50^{+0.34}_{-0.21}$	-	Unknown ⁴
220207765.01	$2563.4267^{+0.0038}_{-0.0042}$	$7.11979^{+0.00062}_{-0.00059}$	$89.0^{+0.8}_{-1.4}$	$0.0205^{+0.0023}_{-0.0017}$	$27.2^{+6.0}_{-8.5}$	$2.1^{+2.3}_{-1.1}$	$0.9^{+1.0}_{-0.5}$	$0.73^{+0.47}_{-0.29}$	$2.71e - 01$	Candidate
220211923.01	$2580.4193^{+0.0046}_{-0.0058}$	$26.6723^{+0.0042}_{-0.0037}$	$89.1^{+0.7}_{-1.2}$	$0.0170^{+0.0012}_{-0.0009}$	$30.8^{+4.6}_{-9.4}$	$2.0^{+1.6}_{-0.9}$	$1.06^{+0.84}_{-0.47}$	$1.29^{+0.65}_{-0.44}$	$3.06e - 02$	Candidate
220216730.01	$2563.5765^{+0.0040}_{-0.0042}$	$18.2946^{+0.0017}_{-0.0016}$	$88.9^{+0.8}_{-1.5}$	$0.0341^{+0.0028}_{-0.0016}$	$27.1^{+4.0}_{-8.7}$	$3.0^{+2.9}_{-1.4}$	$0.82^{+0.77}_{-0.38}$	$0.89^{+0.52}_{-0.33}$	$2.84e - 03$	Candidate
220218012.01	$2570.6444^{+0.0037}_{-0.0036}$	$12.4875^{+0.0012}_{-0.0011}$	$88.7^{+1.0}_{-1.8}$	$0.0257^{+0.0028}_{-0.0014}$	$21.4^{+3.1}_{-6.7}$	$2.8^{+2.5}_{-1.4}$	$1.01^{+0.88}_{-0.48}$	$1.02^{+0.58}_{-0.37}$	$2.29e - 03$	Candidate
220225178.01	2563.5115 ± 0.0024	$4.19097^{+0.00023}_{-0.00024}$	$88.0^{+1.5}_{-2.6}$	$0.0179^{+0.0018}_{-0.0011}$	$14.1^{+2.2}_{-4.2}$	$1.8^{+1.9}_{-0.9}$	$0.95^{+0.96}_{-0.48}$	$0.80^{+0.50}_{-0.31}$	$6.42e - 03$	Candidate
220241529.01	$2561.2331^{+0.0026}_{-0.0025}$	2.08062 ± 0.00014	$86.9^{+2.3}_{-5.4}$	$0.0111^{+0.0010}_{-0.0007}$	$9.0^{+1.5}_{-3.3}$	$0.92^{+0.88}_{-0.44}$	$0.76^{+0.72}_{-0.36}$	$0.83^{+0.48}_{-0.31}$	$1.11e - 02$	Candidate
220245303.01	$2563.4770^{+0.0040}_{-0.0038}$	$3.68035^{+0.00037}_{-0.00038}$	$88.1^{+1.4}_{-2.8}$	$0.0125^{+0.0019}_{-0.0011}$	$13.2^{+2.7}_{-3.8}$	$1.2^{+1.2}_{-0.6}$	$0.85^{+0.91}_{-0.44}$	$0.69^{+0.45}_{-0.28}$	$7.93e - 01$	Candidate
220250254.01	$2560.9578^{+0.0021}_{-0.0020}$	$0.570235^{+0.000027}_{-0.000028}$	$83.7^{+4.6}_{-9.5}$	$0.00893^{+0.00094}_{-0.00071}$	$4.3^{+0.9}_{-1.3}$	$0.92^{+0.88}_{-0.46}$	$0.94^{+0.90}_{-0.47}$	$0.86^{+0.52}_{-0.33}$	$1.84e - 01$	Candidate
220256496.01	2560.8136 ± 0.0022	$0.669558^{+0.000032}_{-0.000033}$	82^{+6}_{-11}	$0.0155^{+0.0014}_{-0.0011}$	$3.5^{+0.6}_{-1.0}$	$1.5^{+1.5}_{-0.8}$	$0.90^{+0.90}_{-0.46}$	$0.78^{+0.49}_{-0.30}$	$4.69e - 03$	Candidate
220292715.01	$2574.48545^{+0.00058}_{-0.00054}$	$41.55293^{+0.00077}_{-0.00087}$	$89.50^{+0.34}_{-0.27}$	$0.0534^{+0.0040}_{-0.0038}$	82^{+29}_{-19}	$4.6^{+4.4}_{-2.3}$	$0.79^{+0.76}_{-0.39}$	$0.79^{+0.48}_{-0.30}$	$2.63e - 01$	Candidate
220294712.01	$2580.7196^{+0.0030}_{-0.0028}$	$23.6078^{+0.0021}_{-0.0022}$	$88.9^{+0.8}_{-1.2}$	$0.0258^{+0.0027}_{-0.0012}$	$27.0^{+4.1}_{-7.6}$	$3.3^{+2.9}_{-1.6}$	$1.2^{+1.0}_{-0.6}$	$1.15^{+0.65}_{-0.41}$	$7.26e - 06$	Planet
220317172.01	2563.1518 ± 0.0029	$4.43574^{+0.00031}_{-0.00032}$	$89.2^{+0.6}_{-1.1}$	$0.0145^{+0.0016}_{-0.0013}$	$33.4^{+8.4}_{-9.8}$	$1.5^{+1.5}_{-0.8}$	$0.94^{+0.93}_{-0.47}$	$0.81^{+0.51}_{-0.33}$	$2.17e - 01$	Candidate
220321605.01	2566.6413 ± 0.0011	9.79540 ± 0.00029	$89.2^{+0.6}_{-1.1}$	$0.0367^{+0.0017}_{-0.0012}$	$28.4^{+2.5}_{-6.6}$	$2.4^{+2.7}_{-1.3}$	$0.61^{+0.67}_{-0.32}$	$0.56^{+0.37}_{-0.23}$	$6.29e - 07$	Planet
220341183.01	$2566.0026^{+0.0065}_{-0.0076}$	8.1309 ± 0.0018	$87.8^{+1.6}_{-3.6}$	$0.0116^{+0.0015}_{-0.0010}$	$13.3^{+2.6}_{-5.0}$	$1.5^{+1.2}_{-0.7}$	$1.17^{+0.92}_{-0.52}$	$1.34^{+0.69}_{-0.47}$	$9.04e - 03$	Candidate
220376054.01	$2563.5996^{+0.0023}_{-0.0026}$	$8.59652^{+0.00053}_{-0.00051}$	$88.2^{+1.3}_{-2.3}$	$0.0181^{+0.0014}_{-0.0008}$	$15.8^{+2.2}_{-4.7}$	$2.3^{+1.9}_{-1.0}$	$1.14^{+0.94}_{-0.50}$	$1.29^{+0.67}_{-0.45}$	$8.69e - 04$	Planet
220397060.01	2570.2329 ± 0.0011	12.09222 ± 0.00039	$87.9^{+1.4}_{-1.6}$	$0.0538^{+0.0022}_{-0.0012}$	$10.4^{+0.7}_{-1.2}$	$6.1^{+4.5}_{-2.8}$	$1.03^{+0.77}_{-0.47}$	$1.33^{+0.65}_{-0.46}$	$2.84e - 10$	Planet
220410754.01	$2570.2516^{+0.0068}_{-0.0069}$	$19.4968^{+0.0042}_{-0.0055}$	$88.9^{+0.8}_{-1.6}$	$0.0176^{+0.0019}_{-0.0013}$	$26.1^{+5.7}_{-8.5}$	$2.1^{+1.7}_{-1.0}$	$1.11^{+0.88}_{-0.49}$	$1.33^{+0.67}_{-0.45}$	$2.15e - 03$	Candidate
220471666.01	$2561.3321^{+0.0024}_{-0.0025}$	$8.26967^{+0.00047}_{-0.00046}$	$89.0^{+0.7}_{-1.3}$	$0.0199^{+0.0013}_{-0.0011}$	$28.5^{+4.1}_{-8.4}$	$2.3^{+2.1}_{-1.1}$	$1.07^{+0.95}_{-0.52}$	$1.06^{+0.57}_{-0.38}$	$1.73e - 02$	Candidate
220481411.01	2561.04162 ± 0.00077	2.174794 ± 0.000038	$86.7^{+2.3}_{-4.1}$	$0.0232^{+0.0013}_{-0.0008}$	$8.5^{+1.1}_{-2.4}$	$1.7^{+1.8}_{-0.9}$	$0.69^{+0.70}_{-0.35}$	$0.69^{+0.42}_{-0.27}$	$1.22e - 09$	Planet
220487418.01	$2562.0045^{+0.0029}_{-0.0027}$	$14.07453^{+0.00091}_{-0.00089}$	$88.2^{+1.3}_{-2.5}$	$0.0245^{+0.0026}_{-0.0011}$	$16.4^{+2.5}_{-5.5}$	$3.2^{+2.5}_{-1.4}$	$1.21^{+0.91}_{-0.52}$	$1.49^{+0.73}_{-0.51}$	$1.88e - 04$	Planet

Table 2: Continued

EPIC	T_0 (BJD-2454833)	P (d)	i (deg)	R_p/R_*	a/R_*	R_p (R_\oplus)	R_* (R_\odot)	M_* (M_\odot)	FPP	Disposition
220503236.01	$2563.4592^{+0.0020}_{-0.0019}$	$8.67987^{+0.00040}_{-0.00042}$	$88.3^{+1.2}_{-1.8}$	$0.0235^{+0.0018}_{-0.0009}$	$15.8^{+1.8}_{-3.8}$	$2.9^{+2.6}_{-1.4}$	$1.1^{+1.0}_{-0.5}$	$1.02^{+0.58}_{-0.38}$	$7.34e - 04$	Planet
220555384.01	$2564.7712^{+0.0013}_{-0.0014}$	4.28453 ± 0.00014	$88.9^{+0.8}_{-1.4}$	$0.0194^{+0.0018}_{-0.0012}$	$25.7^{+4.1}_{-7.6}$	$1.3^{+1.4}_{-0.7}$	$0.62^{+0.67}_{-0.33}$	$0.59^{+0.39}_{-0.24}$	$6.88e - 04$	Planet
220621788.01	2568.2706 ± 0.0022	$13.68253^{+0.00073}_{-0.00076}$	$89.1^{+0.6}_{-1.3}$	$0.0217^{+0.0011}_{-0.0008}$	$29.7^{+3.6}_{-9.2}$	$2.4^{+2.2}_{-1.1}$	$1.02^{+0.93}_{-0.48}$	$1.01^{+0.57}_{-0.38}$	$1.79e - 03$	Candidate
220643470.01	2560.8116 ± 0.0015	$2.653230^{+0.000091}_{-0.000093}$	$71.4^{+5.0}_{-2.0}$	0.0414 ± 0.0026	$2.88^{+0.72}_{-0.23}$	$11.5^{+2.8}_{-2.3}$	$2.55^{+0.61}_{-0.48}$	$21.0^{+4.2}_{-3.7}$	-	Unknown ³⁴
220648214.01	2583.6487 ± 0.0032	$29.4351^{+0.0049}_{-0.0046}$	$89.37^{+0.46}_{-0.86}$	$0.0223^{+0.0014}_{-0.0010}$	43^{+5}_{-13}	$2.8^{+2.1}_{-1.2}$	$1.14^{+0.88}_{-0.50}$	$1.38^{+0.68}_{-0.47}$	$3.95e - 03$	Candidate
220650439.01	2562.3559 ± 0.0023	2.39910 ± 0.00013	$85.7^{+3.1}_{-5.4}$	$0.0162^{+0.0012}_{-0.0008}$	$6.6^{+0.9}_{-1.9}$	$1.8^{+1.8}_{-0.9}$	$1.0^{+1.0}_{-0.5}$	$0.88^{+0.53}_{-0.34}$	$2.38e - 10$	Planet
220674823.01	$2561.0108^{+0.0012}_{-0.0011}$	0.571299 ± 0.000024	80^{+7}_{-13}	$0.0169^{+0.0014}_{-0.0007}$	$2.66^{+0.30}_{-0.66}$	$1.9^{+1.8}_{-0.9}$	$1.01^{+0.95}_{-0.49}$	$0.89^{+0.53}_{-0.34}$	$2.02e - 05$	Planet
220674823.02	$2572.7341^{+0.0030}_{-0.0026}$	13.3398 ± 0.0011	$88.8^{+0.8}_{-1.4}$	$0.0271^{+0.0022}_{-0.0012}$	$24.9^{+3.5}_{-7.4}$	$3.0^{+2.8}_{-1.5}$	$1.00^{+0.93}_{-0.49}$	$0.89^{+0.53}_{-0.34}$	$1.72e - 04$	Planet
220679255.01	$2567.9859^{+0.0052}_{-0.0047}$	$8.1332^{+0.0011}_{-0.0013}$	$89.0^{+0.7}_{-1.4}$	$0.0173^{+0.0018}_{-0.0015}$	$27.1^{+5.2}_{-8.0}$	$2.1^{+1.8}_{-1.0}$	$1.14^{+0.95}_{-0.53}$	$1.22^{+0.63}_{-0.44}$	$6.83e - 02$	Candidate
220709978.01	$2566.0598^{+0.0022}_{-0.0021}$	$15.38886^{+0.00095}_{-0.00093}$	$88.9^{+0.8}_{-1.4}$	$0.0195^{+0.0014}_{-0.0007}$	$23.7^{+2.8}_{-6.4}$	$2.3^{+1.9}_{-1.0}$	$1.08^{+0.87}_{-0.49}$	$1.23^{+0.63}_{-0.43}$	$4.01e - 05$	Planet

Table 3: Stellar Parameters

EPIC	K_p	T_{eff}	$[m/H]$	$\log g$
201384232	12.510	5617 ± 53	-0.12 ± 0.08	4.67 ± 0.10
201441872	12.088	5450 ± 50	-0.13 ± 0.08	4.54 ± 0.10
201505350	12.806	5391 ± 50	-0.03 ± 0.08	4.60 ± 0.10
201546283	12.428	5368 ± 50	0.15 ± 0.08	4.58 ± 0.10
201577035	12.296	5638 ± 50	-0.03 ± 0.08	4.53 ± 0.10
201606542	11.923	5333 ± 50	0.06 ± 0.08	4.54 ± 0.10
201613023	12.137	5663 ± 50	-0.11 ± 0.08	4.30 ± 0.10
201713348	11.531	4944 ± 50	-0.03 ± 0.08	4.70 ± 0.10
201828749	11.564	5628 ± 50	-0.18 ± 0.08	4.57 ± 0.10
201855371	12.997	4382 ± 50	-0.35 ± 0.08	4.71 ± 0.10
201920032	12.890	5548 ± 50	0.13 ± 0.08	4.42 ± 0.10
202091388	13.500	5586 ± 50	0.15 ± 0.08	4.50 ± 0.10
202675839	12.362	5807 ± 50	0.45 ± 0.08	4.25 ± 0.10
203771098	11.648	5744 ± 50	0.44 ± 0.08	4.41 ± 0.10
203826436	12.241	5382 ± 57	-0.07 ± 0.08	4.66 ± 0.10
204750116	11.526	5869 ± 53	0.02 ± 0.08	4.53 ± 0.10
205029914	12.183	5774 ± 50	-0.08 ± 0.08	4.37 ± 0.10
205071984	12.005	5415 ± 50	0.03 ± 0.08	4.73 ± 0.10
205944181	12.410	5257 ± 50	0.03 ± 0.08	4.49 ± 0.10
205950854	12.105	5554 ± 50	-0.13 ± 0.08	4.46 ± 0.10
205957328	12.464	5317 ± 50	0.04 ± 0.08	4.59 ± 0.10
206008091	12.506	5748 ± 50	-0.11 ± 0.08	4.34 ± 0.10
206011496	10.916	5509 ± 50	0.07 ± 0.08	4.49 ± 0.10
206026904	12.150	5134 ± 50	0.11 ± 0.08	4.54 ± 0.10

Table 3: Continued

EPIC	K_p	T_{eff}	$[m/\text{H}]$	$\log g$
206044803	12.975	5761 ± 50	0.17 ± 0.08	4.38 ± 0.10
206082454	12.308	5569 ± 50	-0.06 ± 0.08	4.61 ± 0.10
206096602	12.045	4636 ± 50	-0.29 ± 0.08	4.70 ± 0.10
206114630	11.032	5277 ± 50	0.12 ± 0.08	4.65 ± 0.10
206119924	10.310	4547 ± 50	0.01 ± 0.08	4.64 ± 0.10
206144956	10.396	4799 ± 50	-0.34 ± 0.08	4.55 ± 0.10
206146957	11.379	5744 ± 50	-0.14 ± 0.08	4.57 ± 0.10
206159027	12.597	4893 ± 50	-0.21 ± 0.08	4.74 ± 0.10
206181769	12.770	5131 ± 50	0.06 ± 0.08	4.53 ± 0.10
206192335	11.870	5459 ± 50	-0.15 ± 0.08	4.59 ± 0.10
206245553	11.745	5844 ± 50	0.09 ± 0.08	4.35 ± 0.10
206268299	12.430	5929 ± 60	-0.21 ± 0.08	4.24 ± 0.11
206348688	12.566	6022 ± 51	0.30 ± 0.08	4.26 ± 0.10
206535016	11.644	5199 ± 50	-0.17 ± 0.08	4.52 ± 0.10
201091593	11.855	5280 ± 120	-0.17 ± 0.11	3.04 ± 0.20
201110617	12.947	4463 ± 50	-0.24 ± 0.08	4.68 ± 0.10
201111557	11.363	4720 ± 50	-0.06 ± 0.08	4.50 ± 0.10
201127519	11.558	4997 ± 50	0.30 ± 0.08	4.71 ± 0.10
201130233	12.604	5456 ± 50	0.13 ± 0.08	4.55 ± 0.10
201132684	11.678	5489 ± 50	0.07 ± 0.08	4.46 ± 0.10
201166680	10.897	6213 ± 50	0.14 ± 0.08	4.32 ± 0.10
201211526	11.696	5728 ± 50	-0.20 ± 0.08	4.51 ± 0.10
201225286	11.729	5419 ± 50	-0.10 ± 0.08	4.57 ± 0.10
201227197	12.486	5649 ± 50	0.07 ± 0.08	4.61 ± 0.10

Table 3: Continued

EPIC	K_p	T_{eff}	$[m/H]$	$\log g$
201231064	12.358	4972 ± 50	-0.03 ± 0.08	3.63 ± 0.10
201289302	12.745	5151 ± 50	-0.16 ± 0.08	4.43 ± 0.10
201299088	11.751	5154 ± 50	-0.26 ± 0.08	3.91 ± 0.10
201352100	12.798	5216 ± 50	0.16 ± 0.08	4.70 ± 0.10
201390048	11.961	4885 ± 50	-0.09 ± 0.08	4.71 ± 0.10
201427874	12.819	4937 ± 50	0.14 ± 0.08	4.71 ± 0.10
201437844	9.234	6330 ± 50	-0.15 ± 0.08	4.22 ± 0.10
201528828	11.415	5185 ± 50	-0.05 ± 0.08	4.46 ± 0.10
201595106	11.678	5705 ± 50	-0.01 ± 0.08	4.48 ± 0.10
201615463	11.964	5922 ± 58	0.05 ± 0.08	4.24 ± 0.10
210363145	11.896	5070 ± 50	0.12 ± 0.08	4.67 ± 0.10
210365511	12.439	4672 ± 50	-0.10 ± 0.08	4.63 ± 0.10
210402237	11.801	5839 ± 51	0.20 ± 0.08	4.41 ± 0.10
210403955	12.388	5377 ± 50	0.07 ± 0.08	4.65 ± 0.10
210423938	12.655	4760 ± 50	-0.14 ± 0.08	4.69 ± 0.10
210512842	12.106	5580 ± 70	-0.25 ± 0.08	4.52 ± 0.12
210558622	12.034	4500 ± 50	-0.24 ± 0.08	4.62 ± 0.10
210609658	12.587	5016 ± 50	0.20 ± 0.08	3.81 ± 0.10
210629082	11.580	6148 ± 50	0.29 ± 0.08	4.15 ± 0.10
210643811	10.632	5909 ± 50	0.05 ± 0.08	4.11 ± 0.10
210667381	12.674	5428 ± 50	0.16 ± 0.08	4.63 ± 0.10
210707130	12.099	4441 ± 50	-0.14 ± 0.08	4.65 ± 0.10
210718708	12.801	5129 ± 50	-0.35 ± 0.08	4.52 ± 0.10
210775710	11.827	5738 ± 50	0.07 ± 0.08	4.40 ± 0.10

Table 3: Continued

EPIC	K_p	T_{eff}	$[m/\text{H}]$	$\log g$
210843708	12.783	4710 ± 50	0.30 ± 0.08	3.12 ± 0.10
210848071	11.040	5703 ± 50	-0.06 ± 0.08	4.38 ± 0.10
210857328	12.584	6063 ± 50	0.41 ± 0.08	4.38 ± 0.10
210894022	12.300	5741 ± 50	-0.36 ± 0.08	4.36 ± 0.10
210903662	12.050	5960 ± 150	0.49 ± 0.14	3.51 ± 0.24
210957318	13.171	5574 ± 50	0.13 ± 0.08	4.53 ± 0.10
210965800	12.134	5525 ± 50	0.09 ± 0.08	4.55 ± 0.10
211002562	12.485	6055 ± 73	0.20 ± 0.08	4.29 ± 0.12
211048999	12.659	5015 ± 50	0.03 ± 0.08	4.63 ± 0.10
211089792	12.914	5392 ± 50	0.13 ± 0.08	4.59 ± 0.10
211106187	13.124	4883 ± 99	-1.11 ± 0.09	2.27 ± 0.16
211147528	11.832	6254 ± 98	0.15 ± 0.09	3.19 ± 0.16
211319617	12.393	5263 ± 50	-0.59 ± 0.08	4.70 ± 0.10
211351816	12.409	4836 ± 50	0.27 ± 0.08	3.51 ± 0.10
211355342	12.637	5609 ± 50	0.42 ± 0.08	4.46 ± 0.10
211359660	11.742	5159 ± 50	-0.01 ± 0.08	4.59 ± 0.10
211391664	12.102	6095 ± 50	-0.10 ± 0.08	4.09 ± 0.10
211401787	9.709	6114 ± 50	-0.15 ± 0.08	4.01 ± 0.10
211418290	11.504	5070 ± 59	-0.43 ± 0.08	3.25 ± 0.10
211424769	9.438	6185 ± 50	-0.12 ± 0.08	4.34 ± 0.10
211432167	8.550	6611 ± 50	-0.44 ± 0.08	3.14 ± 0.10
211491383	11.785	6035 ± 50	-0.07 ± 0.08	4.16 ± 0.10
211525389	11.687	5475 ± 50	0.26 ± 0.08	4.51 ± 0.10
211562654	12.754	5482 ± 50	0.09 ± 0.08	4.60 ± 0.10

Table 3: Continued

EPIC	K_p	T_{eff}	$[m/H]$	$\log g$
211594205	10.680	5252 ± 50	-0.22 ± 0.08	4.63 ± 0.10
211606790	12.673	5445 ± 50	0.08 ± 0.08	4.05 ± 0.10
211611158	12.414	5722 ± 50	-0.05 ± 0.08	4.58 ± 0.10
211682544	11.407	5410 ± 50	-0.04 ± 0.08	4.59 ± 0.10
211733267	12.150	5319 ± 50	-0.05 ± 0.08	4.55 ± 0.10
211736671	12.160	5414 ± 54	0.49 ± 0.08	3.75 ± 0.10
211743874	12.486	5985 ± 50	0.08 ± 0.08	4.14 ± 0.10
211763214	12.529	5277 ± 50	-0.20 ± 0.08	4.54 ± 0.10
211770696	12.253	5656 ± 53	-0.28 ± 0.08	4.23 ± 0.10
211800191	12.443	5851 ± 70	-0.35 ± 0.08	4.43 ± 0.12
211818569	12.935	4695 ± 50	-0.14 ± 0.08	4.68 ± 0.10
211886472	11.126	6194 ± 74	0.22 ± 0.08	3.80 ± 0.13
211906650	12.193	5784 ± 50	0.06 ± 0.08	4.45 ± 0.10
211913977	12.619	4942 ± 50	0.14 ± 0.08	4.66 ± 0.10
211941472	11.788	5739 ± 50	0.02 ± 0.08	4.11 ± 0.10
211945201	10.115	6046 ± 50	0.05 ± 0.08	4.14 ± 0.10
211978988	12.588	5759 ± 50	-0.03 ± 0.08	4.31 ± 0.10
211993818	7.218	5265 ± 50	-0.05 ± 0.08	3.20 ± 0.10
212006318	12.909	5838 ± 50	0.03 ± 0.08	4.32 ± 0.10
212006344	12.466	3920 ± 50	-0.34 ± 0.08	4.73 ± 0.10
212008766	12.802	5098 ± 50	-0.15 ± 0.08	4.70 ± 0.10
212012119	11.753	4822 ± 50	-0.08 ± 0.08	4.44 ± 0.10
212110888	11.441	5990 ± 50	-0.01 ± 0.08	4.11 ± 0.10
212132195	11.670	4789 ± 50	-0.18 ± 0.08	4.71 ± 0.10

Table 3: Continued

EPIC	K_p	T_{eff}	$[m/H]$	$\log g$
212138198	12.902	5182 ± 50	0.29 ± 0.08	4.55 ± 0.10
212157262	12.864	5477 ± 50	0.26 ± 0.08	4.62 ± 0.10
212164470	12.704	5982 ± 50	0.16 ± 0.08	4.36 ± 0.10
212303338	9.957	5338 ± 50	0.19 ± 0.08	4.51 ± 0.10
212357477	10.215	5733 ± 50	0.05 ± 0.08	4.51 ± 0.10
212394689	12.206	5503 ± 50	-0.01 ± 0.08	4.61 ± 0.10
212435047	12.389	5752 ± 50	-0.07 ± 0.08	4.36 ± 0.10
212460519	12.445	4396 ± 50	-0.44 ± 0.08	4.73 ± 0.10
212480208	10.892	5631 ± 50	-0.19 ± 0.08	4.39 ± 0.10
212496592	12.966	5176 ± 50	0.31 ± 0.08	4.57 ± 0.10
212521166	11.590	4877 ± 50	-0.30 ± 0.08	4.51 ± 0.10
212534729	13.066	5378 ± 50	-0.06 ± 0.08	4.47 ± 0.10
212555594	12.482	5252 ± 50	0.05 ± 0.08	4.49 ± 0.10
212562715	13.046	5570 ± 50	0.05 ± 0.08	4.60 ± 0.10
212572439	12.835	5054 ± 57	0.34 ± 0.08	4.46 ± 0.10
212577658	11.541	5343 ± 50	0.33 ± 0.08	4.51 ± 0.10
212580872	13.047	5623 ± 50	0.21 ± 0.08	4.47 ± 0.10
212586030	11.689	5084 ± 50	0.36 ± 0.08	3.95 ± 0.10
212587672	12.188	5928 ± 50	-0.21 ± 0.08	4.49 ± 0.10
212639319	12.471	5465 ± 50	0.29 ± 0.08	3.98 ± 0.10
212645891	12.641	5759 ± 50	0.18 ± 0.08	4.47 ± 0.10
212672300	12.846	5979 ± 52	0.10 ± 0.08	4.21 ± 0.10
212679181	12.011	3896 ± 66	-0.28 ± 0.08	4.78 ± 0.11
212686205	12.256	4621 ± 50	-0.26 ± 0.08	4.70 ± 0.10

Table 3: Continued

EPIC	K_p	T_{eff}	$[m/\text{H}]$	$\log g$
212689874	12.330	5712 ± 50	-0.09 ± 0.08	4.55 ± 0.10
212691422	11.923	6045 ± 50	0.01 ± 0.08	4.08 ± 0.10
212697709	12.193	5773 ± 50	0.31 ± 0.08	4.43 ± 0.10
212703473	10.729	5758 ± 50	0.11 ± 0.08	4.46 ± 0.10
212705192	11.728	5888 ± 60	0.06 ± 0.08	4.36 ± 0.10
212735333	11.977	5675 ± 50	-0.01 ± 0.08	4.58 ± 0.10
212768333	11.022	5262 ± 50	-0.16 ± 0.08	4.63 ± 0.10
212772313	10.471	5675 ± 50	0.03 ± 0.08	4.25 ± 0.10
212779596	11.930	4681 ± 50	-0.23 ± 0.08	4.69 ± 0.10
212803289	11.014	6033 ± 50	0.15 ± 0.08	3.78 ± 0.10
212828909	12.244	5233 ± 50	-0.04 ± 0.08	4.71 ± 0.10
213546283	12.031	5631 ± 50	-0.15 ± 0.08	4.29 ± 0.10
213817056	12.964	4863 ± 50	0.27 ± 0.08	4.38 ± 0.10
213919434	11.893	6500 ± 140	0.44 ± 0.13	2.34 ± 0.22
214082960	10.615	5350 ± 110	0.29 ± 0.10	4.59 ± 0.18
214173069	12.928	4714 ± 50	0.22 ± 0.08	4.30 ± 0.10
214234110	11.624	5608 ± 50	0.37 ± 0.08	4.46 ± 0.10
214254518	11.874	4455 ± 50	-0.28 ± 0.08	4.68 ± 0.10
215171927	12.692	4972 ± 50	0.02 ± 0.08	4.52 ± 0.10
215502661	12.032	5694 ± 50	0.00 ± 0.08	4.22 ± 0.10
215854715	12.611	5310 ± 50	0.01 ± 0.08	4.63 ± 0.10
216008129	11.966	5507 ± 50	0.13 ± 0.08	4.68 ± 0.10
216050437	12.326	6390 ± 100	0.45 ± 0.10	4.18 ± 0.17
216114172	12.603	5742 ± 57	0.19 ± 0.08	4.50 ± 0.10

Table 3: Continued

EPIC	K_p	T_{eff}	$[m/\text{H}]$	$\log g$
216166748	11.884	5679 ± 50	0.35 ± 0.08	4.49 ± 0.10
216387101	12.897	5529 ± 50	-0.22 ± 0.08	3.91 ± 0.10
216405287	12.997	5491 ± 58	0.27 ± 0.08	4.55 ± 0.10
216468514	12.749	6178 ± 50	0.35 ± 0.08	4.24 ± 0.10
216494238	12.302	5767 ± 50	0.44 ± 0.08	4.47 ± 0.10
216892056	12.503	4009 ± 74	-0.17 ± 0.08	4.76 ± 0.13
217192839	12.601	4682 ± 50	-0.32 ± 0.08	4.66 ± 0.10
217221649	12.220	6300 ± 150	0.50 ± 0.14	2.63 ± 0.24
217855533	10.043	6244 ± 50	-0.06 ± 0.08	4.11 ± 0.10
217941732	12.283	4528 ± 50	-0.25 ± 0.08	4.62 ± 0.10
217977895	12.745	5510 ± 50	0.00 ± 0.08	4.61 ± 0.10
218131080	12.700	6235 ± 82	0.14 ± 0.08	4.22 ± 0.14
218170789	12.890	5250 ± 50	0.08 ± 0.08	4.31 ± 0.10
218304292	12.511	5779 ± 51	-0.30 ± 0.08	4.14 ± 0.10
218668602	12.411	5231 ± 50	0.21 ± 0.08	4.68 ± 0.10
218916923	11.470	5425 ± 50	0.23 ± 0.08	4.66 ± 0.10
219388192	12.336	5689 ± 50	0.16 ± 0.08	4.43 ± 0.10
220170303	12.114	5000 ± 50	-0.07 ± 0.08	4.43 ± 0.10
220180311	12.676	5200 ± 170	0.36 ± 0.16	3.74 ± 0.27
220186645	12.961	5755 ± 50	0.07 ± 0.08	4.23 ± 0.10
220187552	12.836	4168 ± 50	-0.56 ± 0.08	4.76 ± 0.10
220192485	11.758	5211 ± 50	0.00 ± 0.08	4.53 ± 0.10
220207765	12.170	5318 ± 50	0.26 ± 0.08	4.68 ± 0.10
220211923	12.250	5890 ± 50	-0.26 ± 0.08	4.25 ± 0.10

Table 3: Continued

EPIC	K_p	T_{eff}	$[m/\text{H}]$	$\log g$
220216730	12.826	5043 ± 50	-0.14 ± 0.08	4.46 ± 0.10
220218012	12.971	5522 ± 50	0.11 ± 0.08	4.41 ± 0.10
220225178	12.302	5582 ± 50	-0.11 ± 0.08	4.62 ± 0.10
220241529	10.717	4720 ± 50	-0.06 ± 0.08	4.46 ± 0.10
220245303	11.821	5121 ± 50	-0.03 ± 0.08	4.69 ± 0.10
220250254	11.507	5396 ± 50	0.05 ± 0.08	4.55 ± 0.10
220256496	12.872	5221 ± 50	0.11 ± 0.08	4.60 ± 0.10
220292715	12.213	4895 ± 50	-0.15 ± 0.08	4.52 ± 0.10
220294712	12.264	6057 ± 59	0.10 ± 0.08	4.38 ± 0.10
220317172	12.107	5374 ± 50	0.09 ± 0.08	4.60 ± 0.10
220321605	12.588	4349 ± 50	-0.33 ± 0.08	4.72 ± 0.10
220341183	12.043	5794 ± 50	0.25 ± 0.08	4.25 ± 0.10
220376054	11.597	5768 ± 50	0.12 ± 0.08	4.27 ± 0.10
220383386	8.945	5366 ± 50	-0.01 ± 0.08	4.54 ± 0.10
220397060	12.835	5333 ± 50	0.05 ± 0.08	4.20 ± 0.10
220410754	12.843	5758 ± 50	-0.05 ± 0.08	4.22 ± 0.10
220459949	11.227	5893 ± 90	0.16 ± 0.08	3.01 ± 0.15
220471666	12.798	5704 ± 50	0.11 ± 0.08	4.41 ± 0.10
220474074	12.596	5615 ± 50	0.20 ± 0.08	4.25 ± 0.10
220481411	12.100	4591 ± 50	-0.19 ± 0.08	4.59 ± 0.10
220487418	12.062	5967 ± 50	0.04 ± 0.08	4.17 ± 0.10
220503236	12.713	5757 ± 50	0.25 ± 0.08	4.45 ± 0.10
220555384	12.395	4360 ± 50	-0.20 ± 0.08	4.69 ± 0.10
220592745	11.923	5753 ± 50	0.13 ± 0.08	4.23 ± 0.10

Table 3: Continued

EPIC	K_p	T_{eff}	$[m/\text{H}]$	$\log g$
220621788	11.752	5599 ± 50	0.06 ± 0.08	4.43 ± 0.10
220643470	10.839	4621 ± 50	-0.78 ± 0.08	2.17 ± 0.10
220648214	12.390	5785 ± 50	0.01 ± 0.08	4.21 ± 0.10
220650439	12.232	5716 ± 50	0.13 ± 0.08	4.57 ± 0.10
220674823	11.958	5590 ± 50	0.08 ± 0.08	4.54 ± 0.10
220679255	11.975	5966 ± 50	0.01 ± 0.08	4.33 ± 0.10
220709978	9.443	5934 ± 50	-0.30 ± 0.08	4.29 ± 0.10
228721452	11.325	5859 ± 50	0.19 ± 0.08	4.54 ± 0.10
228725972	12.482	5614 ± 50	-0.22 ± 0.08	4.63 ± 0.10
228729473	11.524	4939 ± 50	-0.04 ± 0.08	3.54 ± 0.10
228732031	11.937	5113 ± 50	-0.15 ± 0.08	4.50 ± 0.10
228734889	12.590	5792 ± 50	0.00 ± 0.08	4.52 ± 0.10
228734900	11.535	5733 ± 50	0.47 ± 0.08	4.26 ± 0.10
228735255	12.483	5637 ± 50	0.29 ± 0.08	4.34 ± 0.10
228736155	12.042	5397 ± 50	-0.08 ± 0.08	4.62 ± 0.10
228737155	11.081	4373 ± 50	-0.73 ± 0.08	2.08 ± 0.10
228754001	11.651	5036 ± 50	0.05 ± 0.08	3.79 ± 0.10
228760097	11.512	5673 ± 50	-0.10 ± 0.08	4.58 ± 0.10
228798746	12.660	4764 ± 50	-0.13 ± 0.08	4.67 ± 0.10
228801451	10.955	5231 ± 50	-0.03 ± 0.08	4.60 ± 0.10
228804845	12.551	6002 ± 50	0.21 ± 0.08	4.29 ± 0.10
228809391	12.595	4240 ± 110	-0.19 ± 0.11	1.93 ± 0.18
228952747	12.224	4325 ± 50	-0.34 ± 0.08	4.73 ± 0.10
228974324	12.873	4033 ± 50	-0.45 ± 0.08	4.78 ± 0.10

Table 3: Continued

EPIC	K_p	T_{eff}	$[m/H]$	$\log g$
229004835	10.151	5870 ± 50	-0.15 ± 0.08	4.40 ± 0.10
229024057	12.927	5370 ± 140	0.33 ± 0.13	4.40 ± 0.22
229039390	12.735	5853 ± 56	-0.10 ± 0.08	4.46 ± 0.10
229131722	12.515	5928 ± 50	0.23 ± 0.08	4.42 ± 0.10
229133720	11.477	4933 ± 50	-0.12 ± 0.08	4.65 ± 0.10

REFERENCES

- Agol, E., Steffen, J., Sari, R., & Clarkson, W. 2005, *MNRAS*, 359, 567
- Akeson, R. L., Chen, X., Ciardi, D., et al. 2013, *PASP*, 125, 989
- Albrecht, S., Winn, J. N., Johnson, J. A., et al. 2012, *ApJ*, 757, 18
- Alonso, R., Brown, T. M., Torres, G., et al. 2004, *ApJ*, 613, L153
- Ballard, S., Fabrycky, D., Fressin, F., et al. 2011, *ApJ*, 743, 200
- Baraffe, I., Chabrier, G., Allard, F., & Hauschildt, P. H. 2002, *A&A*, 382, 563
- Batalha, N. M., Borucki, W. J., Koch, D. G., et al. 2010, *ApJ*, 713, L109
- Belu, A. R., Selsis, F., Morales, J.-C., et al. 2011, *A&A*, 525, A83
- Beuermann, K., Hessman, F. V., Dreizler, S., et al. 2010, *A&A*, 521, L60
- Bond, I. A., Udalski, A., Jaroszyński, M., et al. 2004, *ApJ*, 606, L155
- Borucki, W., Koch, D., Basri, G., et al. 2008, in *IAU Symposium, Vol. 249, Exoplanets: Detection, Formation and Dynamics*, ed. Y.-S. Sun, S. Ferraz-Mello, & J.-L. Zhou, 17–24
- Buchhave, L. A., Latham, D. W., Johansen, A., et al. 2012, *Nature*, 486, 375
- Buchhave, L. A., Bizzarro, M., Latham, D. W., et al. 2014, *Nature*, 509, 593
- Carter, J. A., Fabrycky, D. C., Ragozzine, D., et al. 2011, *Science*, 331, 562
- Charbonneau, D., Brown, T. M., Latham, D. W., & Mayor, M. 2000, *ApJ*, 529, L45
- Charbonneau, D., Brown, T. M., Noyes, R. W., & Gilliland, R. L. 2002, *ApJ*, 568, 377

- Claret, A. 2000, *A&A*, 363, 1081
- Claret, A., & Hauschildt, P. H. 2003, *A&A*, 412, 241
- Díaz, R. F., Almenara, J. M., Santerne, A., et al. 2014, *MNRAS*, 441, 983
- Diaz-Cordoves, J., & Gimenez, A. 1992, *A&A*, 259, 227
- Dotter, A., Chaboyer, B., Jevremović, D., et al. 2008, *ApJS*, 178, 89
- Doyle, L. R., Carter, J. A., Fabrycky, D. C., et al. 2011, *Science*, 333, 1602
- Dressing, C. D., & Charbonneau, D. 2013, *ApJ*, 767, 95
- . 2015, *ApJ*, 807, 45
- Faigler, S., Tal-Or, L., Mazeh, T., Latham, D. W., & Buchhave, L. A. 2013, *ApJ*, 771, 26
- Feroz, F., Hobson, M. P., & Bridges, M. 2009, *MNRAS*, 398, 1601
- Feroz, F., Hobson, M. P., Cameron, E., & Pettitt, A. N. 2013, *ArXiv e-prints*,
arXiv:1306.2144
- Foreman-Mackey, D., Hogg, D. W., Lang, D., & Goodman, J. 2013, *PASP*, 125, 306
- Gaia Collaboration, Prusti, T., de Bruijne, J. H. J., et al. 2016, *A&A*, 595, A1
- Gaudi, B. S., & Winn, J. N. 2007, *ApJ*, 655, 550
- Gelman, A., & Rubin, D. B. 1992, *Statistical Science*, 7, 16
- Gilliland, R. L., Brown, T. M., Christensen-Dalsgaard, J., et al. 2010, *PASP*, 122, 131
- Girardi, L., Bertelli, G., Bressan, A., et al. 2002, *A&A*, 391, 195
- Girardi, L., Groenewegen, M. A. T., Hatziminaoglou, E., & da Costa, L. 2005, *A&A*, 436,

- Goodman, J., & Weare, J. 2010, *Commun. Appl. Math. Comput. Sci.*, 5, 65
- Greene, T. P., Line, M. R., Montero, C., et al. 2016, *ApJ*, 817, 17
- Horch, E. P., Veillette, D. R., Baena Gallé, R., et al. 2009, *AJ*, 137, 5057
- Howell, S. B., Sobek, C., Haas, M., et al. 2014, *PASP*, 126, 398
- Huber, D., Bryson, S. T., Haas, M. R., et al. 2016, *ApJS*, 224, 2
- Johns, M., McCarthy, P., Raybould, K., et al. 2012, in *Proc. SPIE*, Vol. 8444, *Ground-based and Airborne Telescopes IV*, 84441H
- Kipping, D. M. 2013, *MNRAS*, 435, 2152
- Klinglesmith, D. A., & Sobieski, S. 1970, *AJ*, 75, 175
- Kopal, Z. 1950, *Harvard College Observatory Circular*, 454, 1
- Kostov, V. B., Orosz, J. A., Welsh, W. F., et al. 2016, *ApJ*, 827, 86
- Kovács, G., Zucker, S., & Mazeh, T. 2002, *A&A*, 391, 369
- Kreidberg, L. 2015, *PASP*, 127, 1161
- Kurucz, R. L. 1992, in *IAU Symposium*, Vol. 149, *The Stellar Populations of Galaxies*, ed. B. Barbuy & A. Renzini, 225
- Latham, D. W., Stefanik, R. P., Mazeh, T., Mayor, M., & Burki, G. 1989, *Nature*, 339, 38
- Lissauer, J. J., Marcy, G. W., Rowe, J. F., et al. 2012, *ApJ*, 750, 112
- Mandel, K., & Agol, E. 2002, *ApJ*, 580, L171
- Marcy, G. W., Isaacson, H., Howard, A. W., et al. 2014, *ApJS*, 210, 20

- Markwardt, C. B. 2009, in *Astronomical Society of the Pacific Conference Series*, Vol. 411, *Astronomical Data Analysis Software and Systems XVIII*, ed. D. A. Bohlender, D. Durand, & P. Dowler, 251
- Marois, C., Zuckerman, B., Konopacky, Q. M., Macintosh, B., & Barman, T. 2010, *Nature*, 468, 1080
- Mayor, M., & Queloz, D. 1995, *Nature*, 378, 355
- McArthur, B. E., Benedict, G. F., Barnes, R., et al. 2010, *ApJ*, 715, 1203
- Meng, J., Aitken, G. J. M., Hege, E. K., & Morgan, J. S. 1990, *Journal of the Optical Society of America A*, 7, 1243
- Morton, T. D. 2012, *ApJ*, 761, 6
- . 2015, VESPA: False positive probabilities calculator, *Astrophysics Source Code Library*, ascl:1503.011
- Murphy, S. J., Bedding, T. R., & Shibahashi, H. 2016, *ApJ*, 827, L17
- Nesvorný, D., Kipping, D., Terrell, D., et al. 2013, *ApJ*, 777, 3
- Osborn, H. P., Santerne, A., Barros, S. C. C., et al. 2016, *ArXiv e-prints*, arXiv:1605.04291
- Perryman, M., Hartman, J., Bakos, G. Á., & Lindegren, L. 2014, *ApJ*, 797, 14
- Petigura, E. A., Howard, A. W., & Marcy, G. W. 2013, *Proceedings of the National Academy of Science*, 110, 19273
- Qian, S.-B., Dai, Z.-B., Liao, W.-P., et al. 2009, *ApJ*, 706, L96
- Quintana, E. V., Barclay, T., Raymond, S. N., et al. 2014, *Science*, 344, 277

- Ricker, G. R., Winn, J. N., Vanderspek, R., et al. 2015, *Journal of Astronomical Telescopes, Instruments, and Systems*, 1, 014003
- Roddier, F. 1981, *Progress in optics*. Volume 19. Amsterdam, North-Holland Publishing Co., 1981, p. 281-376., 19, 281
- Rogers, L. A. 2015, *ApJ*, 801, 41
- Sanchis-Ojeda, R., Fabrycky, D. C., Winn, J. N., et al. 2012, *Nature*, 487, 449
- Sanders, G. H. 2013, *Journal of Astrophysics and Astronomy*, 34, 81
- Schwarzschild, K., & Villiger, W. 1906, *ApJ*, 23, 284
- Sing, D. K., Désert, J.-M., Lecavelier Des Etangs, A., et al. 2009, *A&A*, 505, 891
- Sing, D. K., Fortney, J. J., Nikolov, N., et al. 2016, *Nature*, 529, 59
- Sinukoff, E., Howard, A. W., Petigura, E. A., et al. 2016, *ApJ*, 827, 78
- Swain, M. R., Vasisht, G., & Tinetti, G. 2008, *Nature*, 452, 329
- Swain, M. R., Vasisht, G., Tinetti, G., et al. 2009a, *ApJ*, 690, L114
- Swain, M. R., Tinetti, G., Vasisht, G., et al. 2009b, *ApJ*, 704, 1616
- Torres, G., Andersen, J., & Giménez, A. 2010, *A&A Rev.*, 18, 67
- Torres, G., Fressin, F., Batalha, N. M., et al. 2011, *ApJ*, 727, 24
- Vanderburg, A., & Johnson, J. A. 2014, *PASP*, 126, 948
- Vanderburg, A., Latham, D. W., Buchhave, L. A., et al. 2016a, *ApJS*, 222, 14
- Vanderburg, A., Bieryla, A., Duev, D. A., et al. 2016b, *ApJ*, 829, L9

Winn, J. 2010, in *Exoplanets*, ed. S. Seager (University of Arizona Press), 55–77

Wolszczan, A. 1994, *Science*, 264, 538

Wolszczan, A., & Frail, D. A. 1992, *Nature*, 355, 145

Yee, J. C., Johnson, J. A., Skowron, J., et al. 2016, *ApJ*, 821, 121

Zhou, G., Rodriguez, J. E., Collins, K. A., et al. 2016, *AJ*, 152, 136